Mon. Not. R. Astron. Soc. **000**, 1–36 (2007) Printed 24 August 2008 (MN LaTeX style file v2.2)

Black holes and core expansion in massive star clusters

A. D. Mackey[1], M. I. Wilkinson[2], M. B. Davies[3], and G. F. Gilmore[4]
[1] *Institute for Astronomy, University of Edinburgh, Royal Observatory, Blackford Hill, Edinburgh, EH9 3HJ, UK*
[2] *Department of Physics & Astronomy, University of Leicester, University Road, Leicester, LE1 7RH, UK*
[3] *Lund Observatory, Box 43, SE-221 00 Lund, Sweden*
[4] *Institute of Astronomy, University of Cambridge, Madingley Road, Cambridge, CB3 0HA, UK*

arXiv:0802.0513v1 [astro-ph] 5 Feb 2008

Draft version 24 August 2008

ABSTRACT
In this study we present the results from realistic N-body modelling of massive star clusters in the Magellanic Clouds. We have computed eight simulations with $N \sim 10^5$ particles; six of these were evolved for at least a Hubble time. The aim of this modelling is to examine in detail the possibility of large-scale core expansion in massive star clusters, and search for a viable dynamical origin for the radius-age trend observed for such objects in the Magellanic Clouds. We identify two physical processes which can lead to significant and prolonged cluster core expansion – mass-loss due to rapid stellar evolution in a primordially mass segregated cluster, and heating due to a retained population of stellar-mass black holes, formed in the supernova explosions of the most massive cluster stars. These two processes operate over different time-scales and during different periods of a cluster's life. The former occurs only at early times and cannot drive core expansion for longer than a few hundred Myr, while the latter typically does not begin until several hundred Myr have passed, but can result in core expansion lasting for many Gyr. We investigate the behaviour of each of these expansion mechanisms under different circumstances – in clusters with varying degrees of primordial mass segregation, and in clusters with varying black hole retention fractions. In combination, the two processes can lead to a wide variety of evolutionary paths on the radius-age plane, which fully cover the observed cluster distribution and hence define a dynamical origin for the radius-age trend in the Magellanic Clouds. We discuss in some detail the implications of core expansion for various aspects of globular cluster research, as well as the possibility of observationally inferring the presence of a significant population of stellar-mass black holes in a cluster.

Key words: stellar dynamics – globular clusters: general – methods: N-body simulations – Magellanic Clouds.

1 INTRODUCTION

As relatively simple objects which are integral to the study of many fundamental astronomical processes, massive star clusters are central to a wide variety of astrophysics over all scales – from star formation and stellar and binary evolution, through stellar exotica and variable stars, and the dynamics of self-gravitating systems, to galaxy formation and evolution, with implications for cosmology. In the context of this wider astrophysics however, it is clearly essential that we understand the clusters themselves: how internal physical processes in clusters shape their overall characteristics (and vice versa), and how individual clusters interact with and are influenced by their local environments. Only when armed with this knowledge is it possible to disentangle cluster evolutionary processes from the specific astrophysics under investigation.

From an observational perspective, we are provided with only a limited set of massive stellar clusters which are close enough to us that they may be fully resolved using presently available facilities (and hence thoroughly studied on a star-by-star basis). The Galactic globular clusters, while constituting the closest ensemble, are not ideal for studying massive star cluster evolution, primarily because they are almost exclusively ancient objects with ages $\sim 10 - 13$ Gyr (see e.g., Rosenberg et al. 1999; Salaris & Weiss 2002; Krauss & Chaboyer 2003; De Angeli et al. 2005). Therefore, while we are able to precisely measure the end-points of massive star cluster evolution, the long-term development which brought them to these observed states must be almost completely inferred. Fortunately, it is relatively straightforward to turn our attention to the Large and Small Magellanic Clouds (LMC/SMC), which both possess extensive systems of star clusters with masses comparable to the Galactic glob-

ulars, but crucially *of all ages:* $10^6 \lesssim \tau \lesssim 10^{10}$ yr. These two nearby galaxies are hence of fundamental importance to studies of star cluster evolution, because they are the only systems in which we can directly observe snapshots of cluster development over the last Hubble time using a sample of fully resolved objects.

Some of the earliest studies to take advantage of this situation and investigate the structural evolution of massive stellar clusters were those of Elson and collaborators. In particular, Elson, Fall & Freeman (1987) constructed radial brightness and density profiles for 10 young clusters in the LMC, while Elson, Freeman & Lauer (1989) and Elson (1991, 1992) extended this study to a larger sample of LMC clusters including much older objects. They discovered a striking relationship between cluster core size and age – specifically, that the observed spread in core radius is a strongly increasing function of age. The youngest clusters in their sample possessed compact cores with $r_c \sim 1-2$ pc, while the oldest clusters exhibited a range $0 \lesssim r_c \lesssim 6$ pc (cf. Fig. 1). Here, cluster core size is parametrised by the observational core radius, r_c, defined as the projected radius at which the surface density/brightness has decreased to half its central value.

The advent of the Hubble Space Telescope (HST) has allowed this discovery to be re-addressed observationally in significantly more detail than was possible with ground-based facilities. HST imaging can resolve Magellanic Cloud star clusters even in their inner cores, so that star counts may be conducted to very small projected radii and accurate surface density/brightness profiles constructed. Mackey & Gilmore (2003a) obtained structural measurements from a homogeneous compilation of archival Wide Field Planetary Camera 2 (WFPC2) imaging of 53 massive LMC clusters spanning the full age range. We found essentially the same relationship as Elson et al. (1989) – the youngest massive LMC clusters possess compact cores of typical radius $\sim 1-2$ pc, but with increasing age the spread in core radius increases such that the oldest clusters span the range $0 \lesssim r_c \lesssim 8$ pc. Mackey & Gilmore (2003b) subsequently extended these HST measurements to 10 SMC clusters, demonstrating for the first time that a radius-age trend indistinguishable from that observed in the LMC exists for this star cluster system.

Following these two studies, we were granted HST time to conduct a snapshot survey of additional massive LMC and SMC star clusters using the Advanced Camera for Surveys (ACS; HST program #9891), with the aim of improving the sampling of the radius-age parameter space. In all, 31 extra LMC and 13 extra SMC clusters were successfully imaged, significantly enlarging the sample. Final structural measurements for these objects are yet to be published (Mackey et al. 2008, in prep.); however preliminary results for the core sizes are plotted in Figure 1, along with the WFPC2 measurements of Mackey & Gilmore (2003a,b). In obtaining these new parameters, photometric measurements were made using the pipeline described by Mackey & Gilmore (2004) and Mackey, Payne & Gilmore (2006), while radial brightness profiles were constructed following procedures essentially identical to those described by Mackey & Gilmore (2003a) but adapted for ACS Wide Field Channel (WFC) imaging. Figure 1 also includes the recent HST/ACS measurements of the SMC cluster BS90 by Rochau et al. (2007).

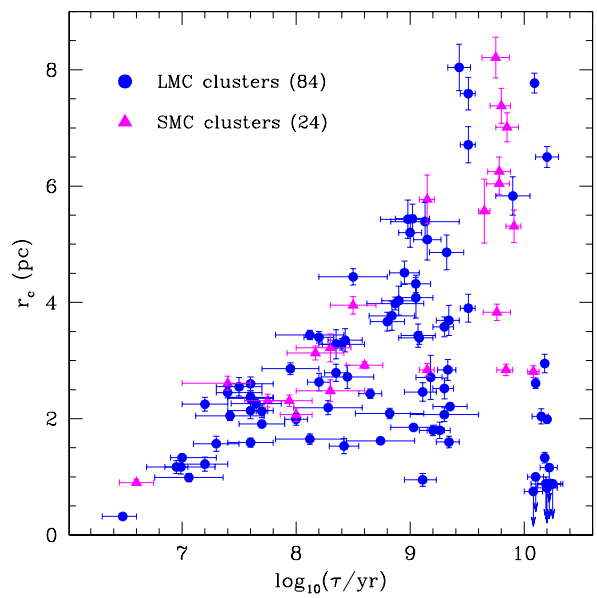

Figure 1. Core radius versus age for massive stellar clusters in the Large and Small Magellanic Clouds. This Figure includes all clusters from the HST/WFPC2 measurements of Mackey & Gilmore (2003a,b) as well as the new preliminary HST/ACS measurements of Mackey et al. (2008, in prep.) from Program #9891, and the recent measurements of BS90 by Rochau et al. (2007). Core radii for several of the oldest compact clusters are upper limits, as indicated (see Mackey & Gilmore 2003a).

Note that the core radii for several of the oldest, most compact clusters in Fig. 1 are upper limits, as indicated. This is due to severe crowding in the HST imaging, and the possibility that several of these clusters are core-collapsed objects (see Mackey & Gilmore 2003a). All affected clusters have measured $r_c < 1$ pc.

Figure 1 represents the most complete and up-to-date information presently available regarding the radius-age trend in the LMC and SMC star cluster systems. The upper envelope is very well defined for all ages up to a few Gyr. At older times than this, the full range of core radii observed in massive star clusters is allowed. In fact the situation is even more dramatic than was appreciated by earlier studies. Several of the oldest clusters in the new ACS sample fall off the top of the diagram: the Reticulum cluster in the LMC, with age $\tau \sim 12-13$ Gyr and $r_c \sim 14.8$ pc; and Lindsay 1 and 113 in the SMC, with $\tau \sim 9$ Gyr and $r_c \sim 16.4$ pc, and $\tau \sim 5$ Gyr and $r_c \sim 11$ pc, respectively. Hence the size range observed for the oldest clusters is $0 \lesssim r_c \lesssim 17$ pc.

These recent measurements of very extended objects are consistent with those for several old globular clusters in the Fornax and Sagittarius dwarf galaxies – Fornax cluster 1, and Terzan 8 and Arp 2 (Mackey & Gilmore 2003c) – which also have very large core radii. A number of Galactic globular clusters are also known to possess extended cores, as seen in Fig. 2 (upper panel), which shows the core radius distribution of the oldest LMC and SMC clusters from Fig. 1 compared with that for the Galactic globular cluster system. The observed ranges in r_c match well, as do the general shapes of the distributions. The main difference is that the distribution for Galactic globulars is more sharply peaked

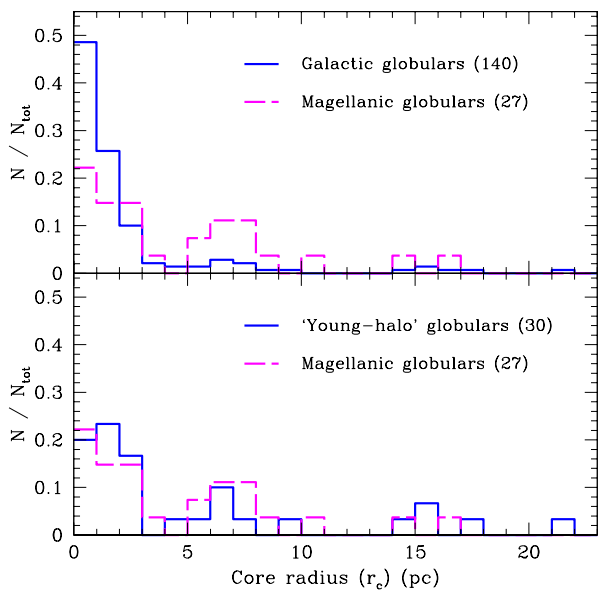

Figure 2. Core radius distributions for the oldest ($\tau \gtrsim 7$ Gyr) Magellanic Cloud clusters from Fig. 1 (dashed lines) and for Galactic globular clusters (solid lines). **Upper panel:** The full sample of Galactic globular clusters with suitable measurements of r_c is plotted; objects which are members or ex-members of the Sagittarius dwarf galaxy are excluded. Data are from Harris (1996) (2003 online update) with new measurements as described in Mackey & Gilmore (2004) and Hilker (2006). The distributions are very similar in range and overall shape; however the Galactic globulars have a sharp peak at small core radii. Note that all Magellanic Cloud clusters with core radius measurements which are upper limits already fall in the smallest r_c bin. **Lower panel:** If only the Galactic "young-halo" subsystem is considered (objects which preferentially lie at Galactocentric radii beyond ~ 15 kpc) a very much closer match is observed.

at small r_c. This is not surprising given that a large fraction of the Galactic globulars reside in the inner Galaxy, where tidal forces are expected to rapidly destroy loosely bound clusters. Indeed, following Mackey & Gilmore (2004) (see also Zinn 1993; Mackey & van den Bergh 2005), if only members of the Galactic globular cluster "young-halo" subsystem are considered (most of which are located at Galactocentric radii larger than ~ 15 kpc), the core radius distribution is an excellent match to that observed for the oldest LMC and SMC objects (Fig. 2, lower panel). The end-points of structural evolution observed for the Galactic globulars appear quite consistent with the end-points of the radius-age trend observed in the Magellanic Clouds.

The simplest interpretation of the radius-age trend is that it represents the progression of cluster structural properties with time[1]. In this scenario, Figures 1 and 2 provide striking evidence that our understanding of massive star cluster evolution is incomplete, since standard models do not predict an order-of-magnitude expansion of the core radius over a Hubble time (e.g., Meylan & Heggie 1997). Identifying the origin of the radius-age trend is therefore of considerable importance for star cluster astrophysics, and all related fields in which star clusters play a prominent role.

Elson et al. (1989) discussed the possibility that the increasing spread in radius with age could reflect inter-cluster variations in the slope of the stellar initial mass function (IMF). Clusters with flat IMFs possess comparatively more massive stars than those with steep IMFs. Consequently, they suffer more severe mass loss due to stellar evolution at early times, resulting in increased relative expansion. However, Elson et al. (1989) found that to induce expansion along the upper envelope of the observed trend would require a very flat IMF slope, and the resulting early mass loss would be severe enough to disrupt the cluster within only a few tens of Myr. An additional problem with the IMF hypothesis concerns the time-scale – the severe mass loss phase lasts for roughly only the first ~ 100 Myr of a cluster's evolution. Therefore, it cannot drive significant expansion over the full range of ages observed for Magellanic Cloud clusters. There is also an increasing body of observational evidence that the IMF in young star clusters is more-or-less invariant (see e.g., Kroupa 2001; de Grijs et al. 2002c).

Wilkinson et al. (2003) used N-body simulations of small star clusters to investigate whether the radius-age trend could reflect core expansion induced by populations of binary stars, or by time-varying tidal fields such as those which clusters on highly elliptical orbits might experience. They observed similar core radius evolution for model clusters on both circular and elliptical orbits, and therefore concluded that the tidal fields of the Magellanic Clouds have not yet significantly influenced the evolution of the intermediate-age clusters in these systems. Furthermore, while they found that the presence of large numbers of hard primordial binaries in their small clusters did lead to a degree of core radius expansion, the magnitude of the effect was insufficient to explain the observed radius-age trend.

Hunter et al. (2003) suggested that rather than representing the results of dynamical evolution, the radius-age trend might instead have its origins in a size-of-sample effect. They measured a very large sample of Magellanic Cloud clusters with masses $10 \lesssim M_{\rm cl} \lesssim 10^6\,{\rm M}_\odot$ and found the signature of such an effect in their data. On a log-abscissa plot such as Fig. 1, older ages correspond to larger time intervals and hence to more clusters forming in each log-time interval. Since the star cluster mass function decreases steeply with increasing cluster mass, this results in the maximum observed cluster mass in each log-time interval increasing with age. The clusters in the sample of Hunter et al. (2003) also showed a weak dependence of size on total mass in that more massive clusters have larger characteristic radii. Combined with the size-of-sample effect, this leads to a size-age distribution with an upper envelope not dissimilar to that evident in Fig. 1. However, it is not clear how applicable this argument is to the cluster sample considered in Fig. 1, because all these clusters have masses $M \gtrsim 10^4\,{\rm M}_\odot$, and show no coherent link between total mass and core radius (e.g., Mackey & Gilmore 2003a). Indeed, restricting the sample of Hunter et al. (2003) to clusters with $M \gtrsim 10^4\,{\rm M}_\odot$, their relationship between size and mass is no longer evident. Hence, a size-of-sample effect apparently does not explain the radius-age trend visible in Fig. 1.

[1] An additional possibility is that cluster formation conditions have changed significantly over the past ~ 10 Gyr. However, presently available constraints on this proposition are limited, and we do not discuss it further here.

Finally, Merritt et al. (2004) examined the formation of cores in primordially cusped clusters (i.e., objects which initially have $r_c \approx 0$) due to the presence of populations of massive stellar remnants. They used analytic calculations in combination with simplified N-body models (composed of equal-mass non-evolving particles) to show that the orbits of the remnants decay due to dynamical friction so that they sink to the cluster centres, heating the stellar background in the process and turning the cusp into a core. The authors also note that further heating of the core may continue over a longer time-scale, due to subsequent evolution of the subsystem of massive remnants. The rates of core growth determined by Merritt et al. (2004) are moderately successful in reproducing the observed radius-age trend; however their models seem to require a range of initial densities which is significantly larger than that found for young clusters in the Magellanic Clouds. It is also not clear how their results would respond to the introduction of a mass spectrum and stellar evolution into the simulations, or the introduction of more realistic initial conditions including the possibility of primordial mass segregation.

As demonstrated above, the radius-age trend is indistinguishable in the LMC and SMC, and the end-points of the trend are consistent with the core radius distributions of the Galactic globular clusters as well as of globular clusters belonging to the Fornax and Sagittarius dwarf galaxies (Mackey & Gilmore 2003c). These galaxies cover a very wide range of masses and morphological types, and hence possess very different tidal fields and possible external torques. This strongly suggests that the radius-age trend is primarily driven by internal cluster processes, rather than external influences (cf. Wilkinson et al. 2003). To this end, we have conducted a series of large-scale, realistic N-body simulations of Magellanic Cloud clusters with the aim of investigating an internal dynamical origin for the radius-age trend. More specifically, we have examined the influence of stellar-mass black holes (BHs), formed in the supernova explosions of the most massive cluster stars, on the long-term evolution of massive stellar clusters. We have also investigated the role played by primordial mass segregation in shaping the early evolution of massive stellar clusters. The basic results from several of our key simulations have been outlined in a recent *Letter* (Mackey et al. 2007); in the present paper, we describe in detail the complete results of our modelling.

2 NUMERICAL SETUP

2.1 N-body code and initial conditions

We use direct, realistic N-body modelling in order to investigate the structural and dynamical evolution of massive star clusters in the Magellanic Clouds. Simulations of this type are a powerful tool for such work because they incorporate all the relevant physical processes with a minimum of simplifying assumptions. Recent technological developments mean that it is now feasible to run models with N sufficiently large so as to be directly comparable to observed clusters. This has a number of advantages, discussed below.

For the present study, we have used the NBODY4 code (Aarseth 1999, 2003) in combination with a 32-chip GRAPE-6 special purpose computer (Makino et al. 2003) at the Institute of Astronomy, Cambridge. This code uses the fourth-order Hermite scheme (Makino 1991) and fast evaluation of the force and its first time derivative by the GRAPE-6 to integrate the equations of motion. Close encounters between stars, including stable binary systems and hierarchies, are integrated via state-of-the-art two-body and chain regularization schemes (Mikkola & Aarseth 1993, 1998). Also included in NBODY4 are routines for modelling the stellar evolution of both single and binary stars. For single stars these take the form of the analytical formulae derived by Hurley, Pols & Tout (2000) from detailed stellar evolution models, following stars from the zero-age main sequence through to remnant phases (such as white-dwarfs, neutron stars and black holes). Binary star evolution is calculated in a similar manner, following the prescription of Hurley, Tout & Pols (2002) and allowing for such phases as the tidal circularization of orbits, mass transfer, and common-envelope evolution. The stellar and binary evolution is calculated in time with the dynamical integration so that interaction between the two is simulated in a consistent fashion (e.g., Hurley et al. 2001, 2005). The stellar evolution routines allow a spread in stellar masses covering the range $0.1 - 100\,\mathrm{M}_\odot$, so that one can construct any desired IMF for a model cluster. In addition, a uniform metallicity for the cluster may be selected in the range $Z = 0.0001 - 0.03$. A mass-loss prescription is included such that evolving stars lose gas through winds and supernova explosions. This gas is instantaneously removed from the cluster. Such mass-loss can rapidly alter the gravitational potential of a star cluster, strongly affecting its early structural and dynamical evolution.

When constructing the initial conditions for our simulated clusters, we were careful to develop models as similar as possible to the youngest massive clusters observed in the LMC and SMC[2]. In general, young massive Magellanic Cloud clusters possess radial surface brightness profiles best described by three-parameter models of the form (Elson, Fall & Freeman 1987; EFF models hereafter):

$$\mu(r_p) = \mu_0 \left(1 + \frac{r_p^2}{a^2}\right)^{-\frac{\gamma}{2}} \quad , \tag{1}$$

where r_p is the projected radius, μ_0 is the central surface brightness, γ determines the power-law slope of the fall-off in surface brightness at large radii, and a is the scale length. These models are a subset of the more general family of models presented by Zhao (1996). The scale length, a, is related to the observational core-radius, r_c, defined here as the projected radius at which the surface brightness has dropped to half μ_0, by:

$$r_c = a(2^{\frac{2}{\gamma}} - 1)^{\frac{1}{2}} \ . \tag{2}$$

Some of the global properties observed for young massive Magellanic Cloud clusters are summarized in Fig. 3. In this plot, we have taken the structural parameters r_c and γ from Mackey & Gilmore (2003a,b), who constructed surface brightness profiles from HST photometry and fit EFF models as defined above. We have also taken the central density

[2] Although we again note the possibility that the initial conditions for massive clusters which formed at high redshift may be different to those for clusters forming today.

and total mass estimates of McLaughlin & van der Marel (2005), which were computed in a more robust manner than those provided by Mackey & Gilmore (2003a,b).

All young LMC and SMC clusters are observed to have cored (rather than cusped) profiles – even the ultra-compact cluster R136 exhibits a small core (see e.g., the discussion in Mackey & Gilmore 2003a, and references therein). Their profiles are well fit by EFF models with $\gamma \sim 2.5$: Elson et al. (1987) found a median value of $\gamma = 2.6$ and a range $2.2 \lesssim \gamma \lesssim 3.2$ for their ten young LMC clusters, while the larger sample plotted in Fig. 3 covers the range $2.05 \leqslant \gamma \leqslant 3.79$ and has a median value $\gamma = 2.67$. Excluding R136, the young LMC and SMC clusters typically have central densities in the range $1.6 \lesssim \log \rho_0 \lesssim 2.8$ (where ρ_0 is in units of $\mathrm{M}_\odot\,\mathrm{pc}^{-3}$), and total masses in the range $4 \lesssim \log M_{\rm tot} \lesssim 5$ (where $M_{\rm tot}$ is in units of $\mathrm{M}_\odot$). R136 is the youngest cluster in the sample, with $\tau \sim 3$ Myr, and also has the greatest central density: $\log \rho_0 \approx 4.8$.

Our model clusters are generated such that they initially have structural parameters in projection which are consistent with those observed for the youngest LMC and SMC clusters. This is achieved by selecting stellar positions randomly from the density distribution of an EFF model with $\gamma = 3$. Each star is assigned a velocity drawn from a Maxwellian distribution, where the velocity dispersion σ is calculated using the Jeans equations assuming an isotropic velocity distribution. In applying this generation algorithm it is important to know that for the EFF family of models, the deprojected density profile is given by:

$$\rho(r) = \rho_0 \left(1 + \frac{r^2}{a^2}\right)^{-\frac{\gamma+1}{2}} , \qquad (3)$$

where ρ_0 is the central volume density. From this, we can derive expressions for the isotropic velocity dispersion as a function of radius. The $\gamma = 3$ case is the closest value of γ to the median $\gamma = 2.67$ observed for young LMC clusters for which the expression for σ is analytic (see Appendix A).

We assign the stars in each cluster a range of masses according to the IMF of Kroupa (2001), which is a multiple-part power-law $\xi(m) \propto m^{-\alpha_i}$, where $\xi(m)dm$ is the number of single stars falling in the mass interval m to $m + dm$. Kroupa (2001) derived his IMF from a large compilation of measurements of young stellar clusters, including many in the LMC. This is in contrast with many other widely used IMFs – for example, the Kroupa, Tout & Gilmore (1993) IMF, which was derived from observations of Galactic field stars in the local neighbourhood and towards the Galactic poles. Therefore, we prefer the Kroupa (2001) IMF for direct modelling of Magellanic Cloud clusters.

We impose a stellar mass range of $0.1 - 100\,\mathrm{M}_\odot$ for our N-body clusters. The extremes of this range are set by the lowest and highest mass stars for which reliable stellar evolution routines are incorporated in NBODY4. Although stars more massive than $100\,\mathrm{M}_\odot$ do form in large star clusters (e.g., Weidner & Kroupa 2006), this upper limit is perfectly acceptable for our present models. For example, Massey & Hunter (1998) found only $\sim 10 - 20$ stars with $M > 80\,\mathrm{M}_\odot$ in the extreme LMC cluster R136 (depending on the adopted stellar evolution models), while the revised calculations in Massey et al. (2004, 2005), which incorporate improved spectroscopy and modelling, suggest

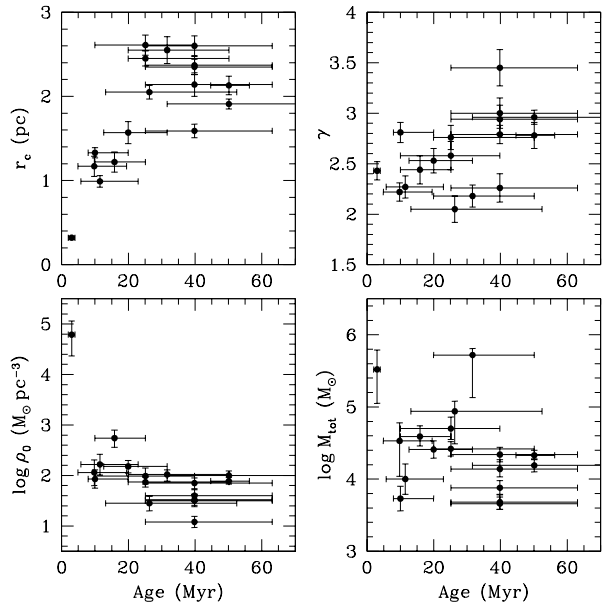

Figure 3. Properties of the young massive clusters observed in the LMC and SMC. Structural data are taken from Mackey & Gilmore (2003a,b), while the central density (ρ_0) and total mass ($M_{\rm tot}$) estimates are taken from McLaughlin & van der Marel (2005), as discussed in the text.

significant reductions in these estimated masses. In practice, we expect that increasing our upper mass limit to the inferred fundamental maximum stellar mass $\sim 150\,\mathrm{M}_\odot$ of Weidner & Kroupa (2004) would have essentially no discernible effect on the global evolution we observe for our models. We note that our lower mass limit means that in practice we only utilise the exponents $\alpha_1 - \alpha_3$ in the Kroupa (2001) IMF.

Our adopted IMF and stellar mass range, along with the requirement that our model clusters have masses commensurate with those observed for young Magellanic Cloud clusters (Fig. 3), allows the total number of stars in each given model to be assigned. Choosing $N \approx 10^5$ stars results in initial total cluster masses of $\log M_{\rm tot} \sim 4.75$.

It is only relatively recently, with the advent of special-purpose hardware, that it has been possible to follow models with such large N over more than a Hubble time of evolution. There are several advantages to running simulations of this size. First, the model star clusters are directly comparable in terms of total mass and central density (see below) to the massive clusters observed in the LMC and SMC. We are therefore now moving into the regime where many of the scaling-with-N issues which it has been necessary to account for in previous studies when applying the results of N-body simulations to the evolution of real clusters (see e.g., Aarseth & Heggie 1998) are circumvented. In addition, with such large N, fluctuations in the global evolution of the N-body model are reduced to the point where they are not significant. For small-N models, it has been standard practice to average the results of a number of simulations to reduce such fluctuations, the amplitudes of which increase with decreasing N (e.g., Giersz & Heggie 1994; Wilkinson et al. 2003; Heggie, Trenti & Hut 2006). For large-N models, this

process is not necessary (see e.g., Hurley et al. 2005)[3]. Finally, with $N \sim 10^5$ we are able to perform detailed simulated observations of our models. This allows us to derive quantities from the simulations which are directly comparable to the genuine observations of LMC and SMC star clusters. As we discuss more fully in Section 3, this step is a vital ingredient in the analysis of realistic N-body models.

Star clusters in the LMC are observed at galactocentric radii between $\sim 0 - 14$ kpc. We therefore evolve our model clusters in a weak external tidal field, rather than in isolation. This external field is incorporated by imposing the gravitational potential of a point-mass LMC with $M_{\rm g} = 9 \times 10^9\,{\rm M}_\odot$, and placing the clusters on circular orbits of galactocentric radius $R_{\rm g} = 6$ kpc. Wilkinson et al. (2003) give a more detailed description of the implementation of the external field within NBODY4, which is done by integrating the equations of motion in an accelerating but non-rotating reference frame, centred on the cluster's centre-of-mass. Adopting a point-mass LMC is a significant over-simplification; however, as noted by Wilkinson et al. (2003), the gradient of this potential is within a factor of two of that in the LMC mass model of van der Marel et al. (2002) at our orbital radius. More importantly however, our aim is not to examine the effect of tidal fields on the evolution of star cluster cores – Wilkinson et al. (2003) demonstrated that external fields comparable to those experienced by Magellanic Cloud clusters do not result in strong core evolution. Rather, we impose an external tidal field so that the gradual evaporation of stars from the cluster may be simulated in a self-consistent fashion, and the rates of evaporation between different models with the same external potential and escape criterion may be easily compared.

In an external potential, the tidal radius of a star cluster on a circular orbit may be estimated from the relationship (King 1962):

$$r_t = R_{\rm g} \left(\frac{M_{\rm cl}}{3M_{\rm g}} \right)^{\frac{1}{3}} , \qquad (4)$$

where $M_{\rm cl}$ is the cluster mass. In NBODY4 stars are deemed to have escaped the cluster when they reach a radius $2r_t$. This is a legitimate approximation – for example Heggie (2001) shows that although cluster stars may on occasion possess orbits which allow them to move far beyond r_t and yet return to the cluster, in practice the vast majority of stars which move beyond a few r_t are permanently lost. In our models r_t is a non-static quantity (since the cluster mass is monotonically decreasing with time); therefore, the instantaneous value is used when assessing the above escape criterion. We caution that other different recipes for the implementation of tidal fields exist, which can lead to significantly different escape rates and thus cluster lifetimes (e.g., Baumgardt 2001; Trenti, Heggie & Hut 2007).

Within the N-body code the equations of motion are integrated in scaled units such that $G = 1$ and the virial radius and total mass of the cluster are also set to unity (Heggie & Mathieu 1986). For a star cluster in virial equilibrium the initial energy in these units is $-1/4$ and the crossing time is $2\sqrt{2}$. Given the total mass of the cluster in solar masses and an appropriately chosen length-scale (which determines the conversion from N-body units to physical units) it is simple to obtain the conversion factors for time and velocity from N-body units to Myr and ${\rm km\,s^{-1}}$, respectively.

Since the chosen length-scale sets the conversion from N-body units to physical units, it controls the physical density of the cluster and hence the physical time-scale on which internal dynamical processes occur. We assume that a model cluster initially just fills its tidal radius. The value of this radius at time $\tau = 0$, determined via Eq. 4 with $M_{\rm cl} = M_{\rm tot}$, therefore sets the ratio between the length scale in N-body units and in physical units (pc). EFF profiles formally have no outer bound, so when randomly generating the initial stellar positions we only accept stars lying within the estimated tidal radius of the cluster under consideration.

The above process determined a length scale of 8.26 pc for our model clusters. This results in an initial central mass density of $\log \rho_0 = 2.31$ and a core radius $r_c = 1.90$ pc for these objects, values which match well those observed for many young Magellanic Cloud clusters (Fig. 3). We note that the clusters described here are not in any way mass segregated; however we also ran simulations of clusters incorporating various degrees of primordial mass segregation, the details of which are described below in Section 2.2. Those objects have the same length scale as the clusters described here, but smaller core radii and much higher central densities, more in line with those of the very young LMC cluster R136. Given this correspondence between our models and the properties of young Magellanic Cloud clusters, we are confident in our selection of an appropriate length scale.

In order to allow investigation of the effects of a population of stellar-mass BHs on cluster evolution, we modified NBODY4 to allow control of the production of BHs in supernova explosions. For the present modelling this is implemented in a relatively simplistic manner; however in principle the relevant code could be altered to cover more complex formation scenarios. We define three variable parameters – the minimum initial mass of BH progenitor stars, the masses of the BHs themselves, and the sizes of the natal velocity kicks which they receive. In each run, all stars initially more massive than $20\,{\rm M}_\odot$ produce BHs, with masses uniformly distributed in the range $8 < M_{\rm BH} < 12\,{\rm M}_\odot$ so that the mean BH mass is $10\,{\rm M}_\odot$. This range is consistent with dynamical masses obtained from observations of X-ray binaries (e.g., Casares 2006). We generate model clusters using the same random seed, so that they initially contain identical stellar populations. Our adopted IMF and total number of particles result in the formation of 198 BHs in all clusters.

The retention fraction of BHs in a given cluster, $f_{\rm BH}$, is strongly dependent on the natal kicks given to the BHs at formation. If a kick is too strong (i.e., $v_{\rm kick}$ larger, roughly, than the escape velocity of the cluster, $v_{\rm esc}$), a BH will quickly cross the limiting radius of the cluster and be removed from the simulation. Under our modifications to NBODY4, BH kicks can vary from zero ($f_{\rm BH} = 1$) to very large ($f_{\rm BH} = 0$) and can be set as a constant, or selected randomly from a uniform distribution with specified limits, or a Maxwellian distribution with a specified mean. By vary-

[3] We caution, however, that small-number statistics may still be subject to significant fluctuations between simulations – an example in the present work are the properties of ejected binaries, as discussed in Sections 4.1 and 4.2.

ing these aspects of natal BH kicks, it is straightforward to control the BH retention fraction in any given model.

Although NBODY4 allows the inclusion of primordial binary stars in cluster models, in the present paper we investigate only models with no primordial binaries. The inclusion of such objects would introduce a very large new area of parameter space for investigation, beyond the scope of the time available for our simulations. Even so, any complete modelling of Magellanic-type clusters should undoubtably incorporate binary star populations as these *are* observed – for example, Elson et al. (1998) observed the binary fraction in the young massive LMC cluster NGC 1818 to be 35 ± 5 per cent in the cluster core, decreasing to 20 ± 5 per cent in the outer regions. We anticipate that future simulations by us will investigate the effects of a binary star population on the results presented in this paper.

Finally, the youngest LMC and SMC clusters typically have metallicities not far from the solar value – for example, the literature compilation in Mackey & Gilmore (2003a) suggests a range $-0.4 \lesssim$ [Fe/H] $\lesssim 0.0$ in the LMC. Therefore, for consistency, in all simulations we set our clusters to have solar metallicity, $Z = 0.02$. However, we note that there is a strong age-metallicity relationship present in both Magellanic Clouds (see e.g., Pagel & Tautvaišienė 1998), in that older clusters are typically much more metal-poor than younger clusters. This may have important implications for our results. Hurley et al. (2004) have demonstrated that differences in metallicity can result in some weak variation in the global structural and dynamical evolution of open clusters, mainly due to differences in stellar winds and mass loss. Furthermore, variations in metal abundance may have a strong effect on the number and mass of BHs produced in supernova explosions (e.g., Zhang et al. 2007). We discuss these aspects further in Section 5.

2.2 Primordial mass segregation

Almost all young massive star clusters which have been observed with sufficient resolution are seen to exhibit some degree of mass segregation. This is true for clusters in the LMC (e.g., NGC 1805, NGC 1818, R136) and SMC (e.g., NGC 330), as well as in the Galaxy (e.g., Orion Nebula Cluster, Arches, Quintuplet) (e.g., de Grijs et al. 2002a,b; Sirianni et al. 2002; Malumuth & Heap 1994; Brandl et al. 1996; Hunter et al. 1996; Kim et al. 2006). Detailed simulations of star cluster formation (see e.g., Bonnell & Bate 2006, and references therein) are consistent with these observations, suggesting that mass segregation in young massive clusters may well be a product of the formation process, in that more massive stars are preferentially formed at the bottom of local potential wells where the gas density is greatest.

Irrespective of whether the observed properties of young massive clusters are truly "primordial", we would like to include the possibility of very early mass segregation in our models in order to investigate its effects on their subsequent evolution. To produce initially mass segregated clusters in a "self-consistent" fashion (i.e., close to virial equilibrium, with all members having appropriate velocities) we developed the following procedure. For a given model, we first generate a cluster as described in the previous Section. This object represents the case where there is no primordial mass segregation. We then implement a mass-function truncation, setting all stars in the cluster with masses greater than $8\,\mathrm{M}_\odot$ to have mass $8\,\mathrm{M}_\odot$. Next, the cluster is evolved dynamically using NBODY4, but with the stellar evolution routines turned off. Hence the cluster begins to dynamically relax and mass segregate. The degree of primordial mass segregation is then easily controlled using a single parameter – the length of time, $T_{\rm MS}$, for which the cluster is "pre-evolved". We selected the truncation limit of $8\,\mathrm{M}_\odot$ empirically so that the pre-evolution can extend for a reasonable duration (a few hundred Myr) without the most massive stars sinking to the cluster centre, interacting, and ejecting each other. Once the desired pre-evolution time is reached, we halt the simulation, replace the mass-truncated stars with their original masses, and take the positions and velocities in the pre-evolved cluster as the initial conditions for the full run including stellar evolution. It is straightforward to read in the pre-evolved cluster using NBODY4, without applying any re-scaling.

Because we replace the mass-truncated stars with their original masses after the pre-evolution is complete, these stars (which number a few hundred in any given model) have slightly incorrect velocities at the beginning of the simulation proper. However, since they almost all reside in the densest part of the cluster, once the full simulation begins these velocities change rapidly and, within the first few local dynamical times, become consistent with the mass distribution in the cluster. Hence this small inconsistency has a negligible effect on the long-term evolution. We also note that during the pre-evolution a small fraction of stars escape from the cluster. This is usually in the form of low-mass stars drifting slowly across the limiting radius, after which they are removed from the simulation. This process is very gradual however, and even the clusters with the longest pre-evolution times ($T_{\rm MS} = 450$ Myr) always retain more than 96 per cent of the mass of the initial non-segregated object. Occasionally, despite the mass-truncation of stars, a massive object will interact strongly with another massive object during the pre-evolution, and be ejected from the cluster. Since we are very interested in how the most massive stars in the cluster affect its evolution, and would like to maintain a high level of consistency between the BH populations of different model clusters, we always replace these objects at the end of the pre-evolution period using their positions and velocities from a few output times before the ejection. Since this is necessary for at most a handful of stars per cluster, the introduced inconsistencies are again negligibly small.

The initial central densities and core radii of our primordially mass segregated model clusters depend on the duration of the pre-evolution. We selected our longest pre-evolution times ($T_{\rm MS} = 450$ Myr) so that the resulting clusters possess properties very similar to those observed for R136, which is the most compact Magellanic Cloud cluster. These models have $r_c = 0.25$ pc and $\log \rho_0 = 4.58$ (cf. Fig. 3). In addition to these global properties, we examined in detail the radial variation in mass function slope for such models and compared the results with those observed for several young Magellanic Cloud clusters. This process is described in detail in Section 4.2; here, we simply note the excellent agreement between the models and the real clusters, as verification of the validity of our pre-evolution algorithm. We also ran simulations using clusters with more intermediate pre-evolution durations ($T_{\rm MS} = 115$ and 225 Myr) – as

might be expected, these objects possess intermediate core radii and central densities: $r_c = 0.83$ pc and $\log \rho_0 = 2.70$, and $r_c = 0.37$ pc and $\log \rho_0 = 3.61$, respectively.

3 "OBSERVING" THE SIMULATIONS

Since the radius-age trend is defined observationally (i.e., by Fig. 1), a vital ingredient in our analysis is to derive measurements from the simulations which are fully consistent with these observations. This requirement highlights a key advantage in running direct, realistic N-body models. Because the positions, velocities, masses and luminosities of all stars are explicitly followed, and because we do not have to worry about scaling our results with N, we are able to perform simulated observations of a model cluster at each output time which lead to measured quantities that are directly comparable to those obtained for the real Magellanic Cloud clusters. More specifically, we calculate the *observational* core radius of each model cluster rather than using the traditional N-body definition (see below), and further, we incorporate many of the subtleties of the actual HST measurements which have defined Fig. 1.

Consider Fig. 4, where we have plotted the detection limits in the HST WFPC2 and ACS imaging from which Fig. 1 was constructed, against cluster age. The brighter limits represent saturation on the images (very bright stars, while recorded on the images, are generally not measured by photometry software), while the lower limits represent the approximate 50 per cent detection completeness levels (faint stars are not always detected above background noise by photometry software). We have split the clusters into four age bins according to approximately constant detection limits – these are delineated on the plot with solid vertical lines. Within each bin, we mark the mean bright and faint detection limits with dashed lines, and the approximate maximum scatter about these means with dotted lines.

A number of things are evident from Fig. 4. First, for any given cluster, the observations sample only a portion of the range of stellar masses present in the cluster. Hence, the surface brightness profile, from which the structural parameters for that cluster are measured, is based only on the spatial distribution of stars within this range. Second, the sampled range varies systematically with cluster age. This is due to the fact that observations of star clusters in the LMC and SMC are commonly aimed at targeting stars near the main-sequence turn-off. Consequently, the required exposure time increases with cluster age, meaning that both the brighter and fainter detection limits become deeper with age. Looking at the two oldest bins, one can also see the increased capabilities of the ACS instrument compared with WFPC2. While the saturation limits are comparable for all clusters in these two bins, the ACS-imaged objects have faint detection limits ~ 2 mag fainter than those of the WFPC2-imaged objects – indicative of the increased sensitivity and dynamic range of ACS over WFPC2.

Given the above, when deriving structural measurements from our N-body simulations we must account for the fact that in the real observations for any given cluster, only a portion of the stellar mass function was sampled, and the fact that this range changes with the age of the target cluster. Since we know the details of the sampling from Fig. 4, this is simple to achieve.

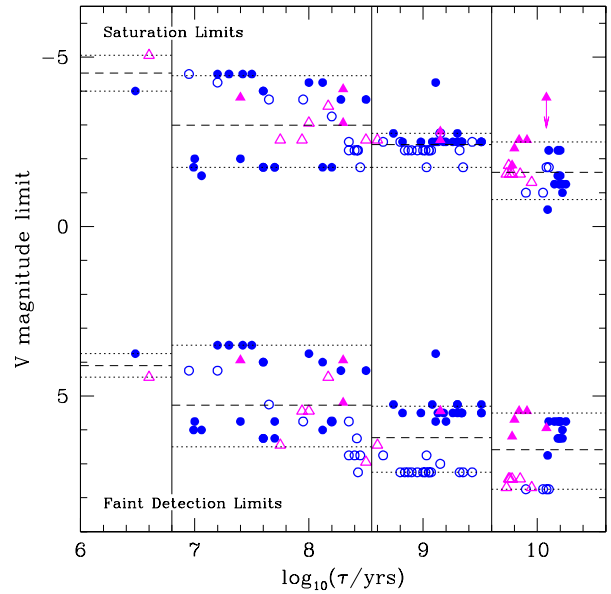

Figure 4. Bright and faint stellar detection limits on the HST/WFPC2 and ACS images of LMC and SMC clusters used for the measurements presented in Fig. 1. Circular symbols mark LMC clusters, while SMC objects are triangles. Filled symbols represent the WFPC2 imaging described in Mackey & Gilmore (2003a,b) while open symbols are the ACS imaging from Mackey et al. (2008, in prep.). Clusters are split into four age bins, delineated with solid vertical lines. Within each age bin, the mean bright and faint detection limits are marked by dashed lines, while the approximate maximum scatter about each mean is marked by a pair of dotted lines. For ease of reference, absolute magnitudes $M_V = (-5, 0, 5)$ correspond to zero-age main sequence stellar masses of $M_* \sim (45.0, 4.20, 1.06)\,\mathrm{M}_\odot$ at solar metallicity.

To "observe" a model cluster, we pass the N-body data through a measurement pipeline essentially identical to that we used to obtain structural quantities for the LMC and SMC samples (full details of the observational pipeline may be found in Mackey & Gilmore 2003a). For the data produced at a given output time, we first convert the luminosity and effective temperature of each star in the cluster to $UBVRI$ standard magnitudes, using the bolometric corrections of Kurucz (1992) supplemented with those of Bergeron, Wesemael & Beauchamp (1995) for white dwarfs. We also convert the position and velocity of each star to physical units using the appropriate length and velocity scale factors (see Section 2.1). With this complete, we next impose the bright and faint detection limits appropriate to the output time (these are the dashed mean limits in Fig. 4). This leaves an ensemble of stars with which to construct a surface brightness profile, which we do following Mackey & Gilmore (2003a,b). We project the three-dimensional position of each star onto a plane, construct annuli of a given width about the cluster centre, and calculate the surface brightness in each annulus. For consistency with the observational pipeline, we use a variety of annulus widths so that both the bright inner core and the fainter outer regions of the cluster are well measured. Next, we account for the fact that both the WFPC2

and ACS cameras have fields-of-view which are considerably smaller than the area on the sky filled by a Magellanic Cloud cluster, which might typically have $r_t \sim 40 - 50$ pc (i.e., $r_t \sim 160 - 200''$ at the LMC distance) (see e.g., Mateo 1987; Olsen et al. 1998). This results in surface brightness profiles generally being truncated beyond projected radii $r_p \sim 25$ pc (Mackey & Gilmore 2003a,b). After imposing this limit, we finally fit an EFF model of the form of Eq. 1 to the resulting surface brightness profile, and from this model derive the structural parameters – in particular the core radius, r_c, and the power-law slope at large radii, γ. To reduce noise we repeat this process for three orthogonal planar projections at each output time and average the results.

It is worth noting the difference between the quantity r_c and the 'core radius' usually defined in N-body simulations. This has been discussed in some detail by Wilkinson et al. (2003); however, in the interests of clarity we re-iterate a few of the most salient points. Traditionally, observers, theorists, and numericists have employed different interpretations of the 'core radius'. That for observers is as defined above (Eq. 2), as the projected radius at which the surface brightness (or density) has dropped to half the central value. Theoretically defined, the core radius is the natural scale-length of the model under consideration – for example, in EFF models a is the scale-length. Eq. 2 provides a general relation between a and r_c. It should be noted however, that as a cluster evolves, the EFF parameters are not static, and therefore the ratio between a and r_c is variable with time.

In N-body simulations the numerically calculated 'core radius' is more correctly termed the density radius, r_d. The implementation in NBODY4 is based on a quantity described by Casertano & Hut (1985), so that r_d is defined as the density-weighted average of the distance of each star from the density centre of the cluster (Aarseth 2001). The local density at each star is computed from the mass within the sphere containing the six nearest neighbours. As noted by Wilkinson et al. (2003), there is no general relationship between r_d and r_c, and in fact the behaviour of r_c and r_d may be quite different throughout a simulation.

As a final remark, we briefly consider the appropriateness of fitting a power-law profile (Eq. 1), which formally has no outer limit, to a simulated cluster evolving in a tidal field. There are two reasons why this is acceptable. First, because of the radial truncation imposed to mimic the field-of-view limitations of the WFPC2 and ACS cameras, our derived surface brightness profiles do not reach as far as the cluster tidal radius. Following Mackey & Gilmore (2003a,b), it is therefore legitimate to fit EFF models to these observed profiles, even when a cluster is dynamically old enough to exhibit a tidal truncation – in the interests of obtaining measurements of γ which are, like those for r_c, directly comparable to the real observations, we choose to employ the same methodology. Even without the truncation of our radial profiles, an EFF model would still have been the most appropriate choice. This is due to the treatment of stellar escapers in NBODY4, as discussed in Section 2.1. While the tidal radius r_t is estimated from Eq. 4, stars are not removed from the simulation until they reach $2r_t$. Hence they are free to populate the region $r_t < r < 2r_t$, and there is no truncation in the density profile at (or near) r_t, even for dynamically old clusters.

4 SIMULATIONS AND RESULTS

The properties of our N-body runs are listed in Table 1. Our main set of models are labelled Runs 1–4. These cover the extremes of the parameter space we are interested in investigating, spanned by BH retention fractions $f_{\rm BH} = 0$ and $f_{\rm BH} = 1$, and the pre-evolution durations $T_{\rm MS} = 0$ Myr (i.e., no primordial mass segregation) and $T_{\rm MS} = 450$ Myr (strong primordial mass segregation, matching that observed in young LMC and SMC objects). These runs are therefore expected to represent the extremes of cluster evolution induced by variation of the BH retention fraction and the degree of primordial mass segregation. The global properties of these four Runs have already been presented in a short *Letter* (Mackey et al. 2007); in the present paper we examine their evolution in considerably more detail.

In addition to our four primary runs, we performed several additional simulations in order to sample the parameter space more completely, and in particular verify that models with intermediate values of $f_{\rm BH}$ and $T_{\rm MS}$ exhibited evolution intermediate between that displayed by Runs 1–4. To this end, Runs 4a and 4b explore the effects of primordial mass segregation in more detail, while Run 5 highlights the effects of natal kicks on BH retention and the subsequent cluster evolution. Finally, Run 6 is used to address the question of whether we can reproduce the cluster evolution induced by a significant BH population by retaining neutron stars (NSs) instead of the BHs.

For each run, we measured the initial cluster mass, central density, and observed structural parameters r_c and γ – these are all listed in Table 1. It is important to re-emphasize how closely these correspond to the observed quantities for the youngest massive clusters in the Magellanic Clouds. This can be seen explicitly by comparing the values listed in Table 1 with the plots in Fig. 3. The model clusters with no primordial mass segregation have $r_c \sim 1.9$ pc, $\gamma \sim 3.0$, and $\log \rho_0 \sim 2.3$. These clusters therefore appear very similar to a number of Magellanic Cloud clusters with ages of ~ 20 Myr. In contrast, the heavily mass segregated model clusters have much smaller cores and higher central densities, with $r_c \sim 0.25$ pc and $\log \rho_0 \sim 4.6$. They also have flatter power-law fall-offs, with $\gamma \sim 2.3$. In this respect, they strongly resemble the very compact massive young LMC cluster R136, which has an age of ~ 3 Myr. The total masses of all models are very similar, in the range $4.728 \leqslant \log M_{\rm tot} \leqslant 4.746$. The variation is due to the pre-evolution procedure used to develop the mass segregated initial conditions, as described in Section 2.2. From comparison with Fig. 3, it is clear that our N-body clusters have masses typical of the youngest clusters in the observed sample. We also note that the "observed" integrated colours of our models at early times are consistent with measurements for young Magellanic Cloud clusters from the literature – for example, the integrated $(B - V)$ colours compiled by Bica et al. (1996).

Given the close correspondence between the properties of our model clusters and those observed for young LMC and SMC objects, we are confident that our N-body simulations are directly modelling the evolution of massive Magellanic Cloud clusters.

Output data was produced for each Run at intervals of $\Delta\tau = 1.5$ Myr for $\tau <= 100$ Myr, and at intervals of $\Delta\tau = 15$ Myr for $\tau > 100$ Myr. It is worth noting that no

Table 1. Details of N-body runs and initial conditions. Each cluster begins with N_0 stars with masses summing to $M_{\rm tot}$, and initial central density ρ_0. Initial cluster structure is "observed" to obtain r_c and γ. Each model is evolved until $\tau_{\rm max}$.

Name	N_0	$\log M_{\rm tot}$ ($\rm M_\odot$)	$\log \rho_0$ ($\rm M_\odot\,pc^{-3}$)	r_c (pc)	γ	Initial MSeg ($T_{\rm MS}$)	BH Retention ($f_{\rm BH}$)	$\tau_{\rm max}$ (Myr)[1]
Run 1	100 881	4.746	2.31	1.90 ± 0.09	2.96 ± 0.17	None	0.0	19 987
Run 2	100 881	4.746	2.31	1.90 ± 0.09	2.96 ± 0.17	None	1.0	10 668
Run 3	95 315	4.728	4.58	0.25 ± 0.04	2.33 ± 0.10	450 Myr	0.0	11 274
Run 4	95 315	4.728	4.58	0.25 ± 0.04	2.33 ± 0.10	450 Myr	1.0	10 000
Run 4a	98 605	4.738	2.70	0.83 ± 0.07	2.45 ± 0.14	115 Myr	1.0	4 274
Run 4b	97 209	4.733	3.61	0.37 ± 0.05	2.34 ± 0.10	225 Myr	1.0	4 457
Run 5	95 315	4.728	4.58	0.25 ± 0.04	2.33 ± 0.10	450 Myr	0.5	10 059
Run 6	100 881	4.746	2.31	1.90 ± 0.09	2.96 ± 0.17	None	0.0, NS[2]	19 987

[1] As described in Section 4, no special significance should be attached to the listed values of $\tau_{\rm max}$.
[2] Run 6 is identical to Run 1, except with natal neutron star kicks set to zero so that $f_{\rm NS} = 1.0$.

special significance should be attached to the listed values of $\tau_{\rm max}$ in Table 1. The main criterion for our primary Runs (Runs 1–6, excluding Runs 4a and 4b) was that $\tau_{\rm max}$ be larger than ~ 10 Gyr, to approximate the ages of the oldest Magellanic Cloud globular clusters. The listed $\tau_{\rm max}$ simply represent the most convenient termination points beyond this time. For interest's sake, Runs 1 and 6 were evolved for significantly longer periods ($\tau_{\rm max} = 20$ Gyr) than the other models, so that the clusters passed through the core-collapse phase. In contrast, Runs 4a and 4b were evolved only as long as necessary (i.e., just long enough for the effects of intermediate values of $T_{\rm MS}$ to become evident), to save on computation time.

4.1 Runs 1 and 2: No mass segregation

We first consider the pair of simulations labelled Run 1 and Run 2. Neither of these two model clusters have primordial mass segregation, and both start with identical initial conditions, to the extent that they share the same random seed. The sole difference between them is that in Run 1 the natal BH kicks are set to be $v_{\rm kick} \approx 200\ {\rm km\,s^{-1}}$, whereas in Run 2 they are set to be zero. Thus, every BH formed in a supernova explosion in Run 1 is provided with a sufficiently large random velocity that it very rapidly escapes from the cluster, so the retention fraction is $f_{\rm BH} = 0$. Conversely, in Run 2 all 198 BHs are retained in the cluster and the retention fraction is $f_{\rm BH} = 1$. The purpose of these runs is twofold. First, Run 1 lets us consider the long-term evolution of our simplest cluster set-up – no primordial mass segregation, and zero BH retention. This model therefore constitutes a control run against which the evolution of all our other models may be compared. Second, by making such a comparison, Run 2 lets us isolate the effects of a population of stellar-mass black holes on the structural and dynamical evolution of a massive star cluster.

The progress of Runs 1 and 2 across the radius-age plane is displayed in Fig. 5 (left panel). Also shown is the evolution of these two runs in the γ-age plane (right panel). First consider Run 1, which behaves exactly as expected for a classical massive stellar cluster. At very early times, extending to roughly $\tau \sim 100$ Myr, there is a period of severe mass loss due to the rapid evolution of the most massive stars in the cluster. By $\tau \sim 100$ Myr, approximately 25 per cent of the initial cluster mass has been lost. The 198 BHs are formed in supernova explosions between 3.5-10 Myr and, since they are born with $v_{\rm kick} \approx 200\ {\rm km\,s^{-1}}$, all are immediately ejected from the cluster. From Fig. 5, it is clear that the violent relaxation experienced by the cluster when $\tau \lesssim 100$ Myr is not reflected in its core-radius evolution, presumably because the mass loss is distributed evenly throughout the cluster. Similarly, there is no evidence of the violent relaxation phase in the evolution of γ.

As the cluster grows older, the rate of mass loss decreases and the cluster settles into a quasi-equilibrium state, where dynamical evolution is dominated by two-body relaxation processes. The median relaxation time for this $N = 10^5$ star cluster is given by $t_{rh} \approx 1.9{\times}10^5\ M_{\rm cl}^{1/2} m_*^{-1} r_h^{3/2}$ (Binney & Tremaine 1987) where m_* is the typical stellar mass and r_h is the 3-dimensional radius containing $0.5 M_{\rm cl}$. At $\tau = 100$ Myr, when the rapid early mass loss is mostly complete, $M_{\rm cl} \approx 43\,500\ {\rm M_\odot}$, $m_* \approx 0.45\ {\rm M_\odot}$ and $r_h \approx 8$ pc, so that $t_{rh} \sim 2$ Gyr. Mass segregation develops in the cluster on roughly this time-scale: this is evident in Fig. 5 as a gradual contraction in r_c as the most luminous stars in the magnitude range used to measure the structural parameters (cf. Fig. 4) sink towards the cluster centre. As two-body relaxation proceeds and mass segregation becomes more prominent, the core radius steadily shrinks with time. The power-law fall-off, γ, slowly becomes steeper during this phase; however as the core becomes increasingly more compact, so γ becomes increasingly flatter after $\tau \sim 10$ Gyr.

Eventually, after many Gyr of evolution, Run 1 enters the core-collapse phase. The point of greatest collapse (smallest r_c) occurs at $\tau \approx 17.4$ Gyr, when the central mass density reaches $\log \rho_0 \approx 4.5$ – a value commensurate with those inferred for NGC 2005 and 2019, the most likely core collapsed clusters in the LMC (e.g., Mackey & Gilmore 2003a; McLaughlin & van der Marel 2005). The point of greatest collapse coincides with a spate of binary star formation in the core – by $\tau = 17.5$ Gyr there are seven newly-formed binary stars. Subsequently, up until the end of the simulation at $\tau = 20$ Gyr, there is no significant change in the observed value of r_c. Defining the cluster age in terms

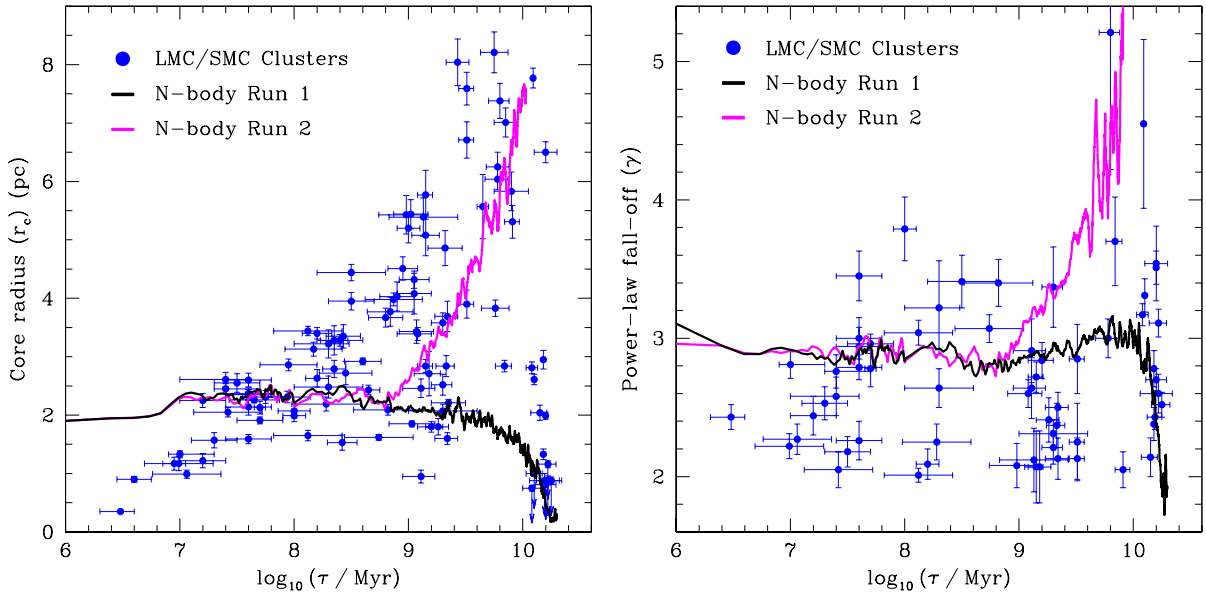

Figure 5. Structural evolution of N-body Runs 1 and 2. Neither has primordial mass segregation; the only difference between them is the BH retention fraction ($f_{\rm BH} = 0$ and 1, respectively). **Left panel:** Evolution of r_c, observed as described in Section 3. Run 1 evolves exactly as expected for a classical massive star cluster, with the main trend being a slow contraction in r_c as the system relaxes dynamically and moves towards core collapse. In stark contrast, Run 2 evolves very similarly to a point, after which strong expansion in the core radius is observed. The presence of 198 stellar-mass black holes in this cluster thus leads to strikingly different core radius evolution. **Right panel:** Evolution of the power-law fall-off, γ, again observed as described in Section 3. As with r_c, Run 2 evolves identically to Run 1 until the BH population becomes dynamically active, after which the evolution strongly diverges with Run 2 developing a steep fall-off in its outer regions. In this panel, only data points from the WFPC2 observations of Mackey & Gilmore (2003a,b) are plotted. Measurements of γ from the recent ACS observations of Mackey et al. (2008, in prep.) are not yet finalised.

of an integrated median relaxation time, which is necessary because t_{rh} is a constantly evolving quantity, we find that at $\tau = 17.4$ Gyr, $8.37\,t_{rh}$ has elapsed.

Fig. 6 illustrates the evolution of Run 1 in more detail. In the top panel a series of Lagrangian radii are plotted – here, we define $R_{x\%}$ to be the 3-dimensional radius containing x per cent of the *stellar* mass in the cluster – that is, *excluding* BHs. This exclusion is not important for Run 1, since all BHs are gone from the cluster by ~ 15 Myr; however it is crucial for examining the evolution of the stellar component of Runs in which $f_{\rm BH} > 0$. Unlike r_c, the innermost Lagrangian radii in Run 1 do show an increase in size in reaction to the early mass-loss phase; however, this increase is only very modest. In addition, the innermost Lagrangian radii do not show any sign of contraction until much later than does r_c – this is an indication of the luminosity (and hence mass) weighting inherent in the calculation of r_c. The half-mass radius of the cluster shows only a small amount of variation throughout its evolution. The outer radii also show only very gradual evolution. The main feature is an expansion in the 90% radius during the mass-loss phase. This is due to stars in the very outer regions of the cluster drifting beyond r_t as the cluster rapidly loses mass. Eventually these objects are removed from the simulation (once they get beyond $2r_t$) and the 90% radius slowly contracts. This contraction continues as the cluster slowly loses mass for the rest of its lifetime, and r_t gradually shrinks accordingly.

In the lower panel of Fig. 6, the mean stellar mass in shells encompassed by selected Lagrangian radii is plotted. This plot therefore shows the development of mass segregation in Run 1. This process is inhibited by the early violent relaxation phase, and there is only a very small degree of segregation present in the cluster's central regions by $\tau = 100$ Myr. Subsequently however, the stratification becomes very well established. As expected, this occurs more rapidly in the central regions of the cluster, where the relaxation time is shortest. By the time the core-collapse phase is reached, there is a large degree of mass segregation present in the model cluster. One notable feature, exhibited by both the outermost shell and the full cluster mean, is an increase in the mean stellar mass after $\tau \sim 10$ Gyr. This is due to the preferential removal of low-mass cluster stars by the external tidal field. These stars typically reside in the outer cluster regions at late times, and are hence far more susceptible to tidal effects than are the more massive objects which inhabit the cluster core. At late times, stellar evolution has all but slowed to a halt so that the tidal stripping of low-mass stars has a significant effect on the mean stellar mass.

Now consider Run 2, in which the BH kicks $v_{\rm kick} = 0\,{\rm km\,s^{-1}}$ so that $f_{\rm BH} = 1$. From inspection of Fig. 5, it is clear that the evolution of both r_c and γ is indistinguishable from that seen in Run 1 up to $\log\tau \sim 8.8$, after which strong expansion of r_c is observed for Run 2, in conjunction with a significant steepening in γ. A careful comparison between the two models reveals that this divergence begins at $\tau \approx 650$ Myr. The expansion of r_c in Run 2 continues for the remainder of the simulation, until $\tau_{\rm max} = 10.67$ Gyr. Since Runs 1 and 2 are identical apart from the kicks imparted to the BHs on their formation, the strongly different evolution

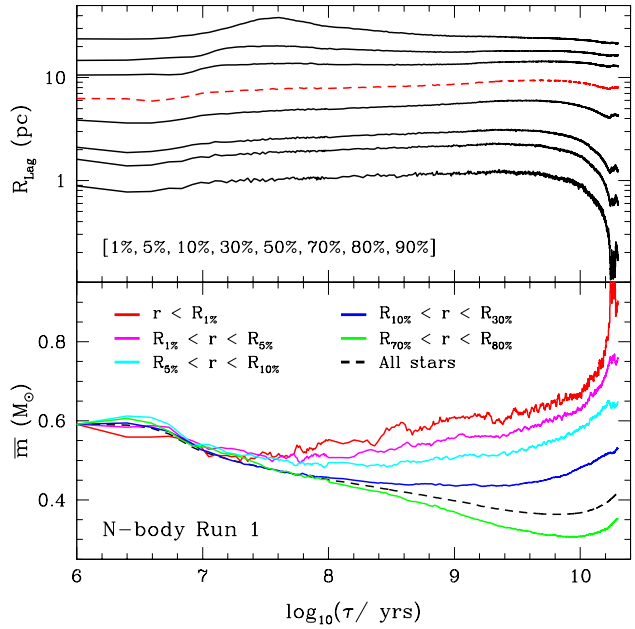

Figure 6. Evolution of various Lagrangian radii (top panel) and the mean stellar mass in the shells encompassed by selected Lagrangian radii (lower panel) for Run 1. The radii displayed in the top panel are, from inner to outer, the 1%, 5%, 10%, 30%, 50% $= r_h$ (dashed line), 70%, 80%, and 90% radii. In the lower panel the shells are defined by: $r \leqslant R_{1\%}$, $R_{1\%} < r \leqslant R_{5\%}$, $R_{5\%} < r \leqslant R_{10\%}$, $R_{10\%} < r \leqslant R_{30\%}$, and $R_{70\%} < r \leqslant R_{80\%}$ (these are listed in order from the upper to lower solid lines at the right hand side of the panel). The dashed line is the mean mass for all stars in the cluster.

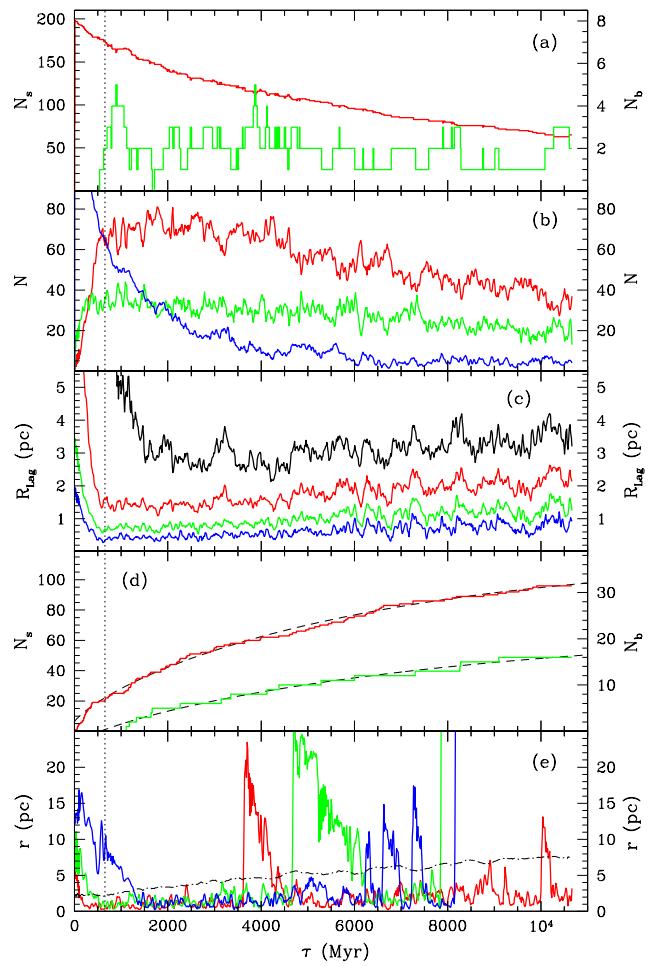

Figure 7. Properties of the BH population in Run 2 as a function of time: (a) the number of single BHs (upper line) and binary BHs (lower line) in the cluster; (b) the number of BHs within the shells encompassed by the *stellar* Lagrangian radii (cf. Fig. 6) $r \leqslant R_{1\%}$, $R_{1\%} < r \leqslant R_{5\%}$, and $r > R_{10\%}$ (the upper, middle and lower lines, respectively, at the right of the plot); (c) the *black hole* 10%, 25%, 50% and 75% Lagrangian radii (respectively, the innermost to outermost lines); (d) the cumulative numbers of escaped single BHs (upper) and binary BHs (lower), along with fits of the form $N_e = A_0 + A_1\tau - A_2\tau\log\tau$ (dashed lines); and (e) the radial positions of three typical BHs. The vertical dotted line indicates $\tau = 650$ Myr, the approximate time when core expansion begins. The evolution of r_c is plotted (dot-dashed line) in panel (e). Note the different axis scales on either side of panels (a) and (d).

observed for these two models must be due to the presence of the 198 BHs in Run 2.

The properties of this BH population as a function of time are illustrated in Fig. 7. As in Run 1, by $\tau \approx 100$ Myr, the most violent phase of stellar evolution is essentially complete. At this time, the BHs (of typical mass $m_{\rm BH} = 10\,{\rm M}_\odot$) are already significantly more massive than any other cluster members (of typical mass $m_* \approx 0.45\,{\rm M}_\odot$), and are hence beginning to sink to the cluster centre via dynamical friction, on a time-scale of $\sim (m_*/m_{\rm BH})\,t_{rh} \approx 90$ Myr.

This is evident from panels b and c in Fig. 7. Panel b shows the number of BHs within the shells encompassed by the *stellar* Lagrangian radii $r \leqslant R_{1\%}$, $R_{1\%} < r \leqslant R_{5\%}$, and $r > R_{10\%}$. The evolution of these Lagrangian radii themselves may be seen in Fig. 8, which is discussed in more detail below. Panel c shows the evolution of the *black hole* Lagrangian radii $B_{10\%}$, $B_{25\%}$, $B_{50\%}$, and $B_{75\%}$, where, by analogy with the stellar Lagrangian radii, $B_{x\%}$ is the 3-dimensional radius containing x per cent of the BH mass in the cluster.

By 200 Myr, the mass density of BHs at the centre of the cluster is already roughly equal to that of the stars, and by 400 Myr it is about three times larger. Shortly after, this central BH subsystem becomes unstable to further contraction (see Spitzer 1987, Eq. 3-55) and decouples from the stellar core in a runaway gravothermal collapse, leading to a very rapidly increasing central BH density – by 490 Myr, the central density of the BH subsystem is ~ 80 times that of the stars. This is sufficiently dense for the creation of stable BH binaries in three-body interactions to be initiated – the first such object is formed at ~ 510 Myr, and by ≈ 650 Myr there are several (see Fig. 7a). At this point, the collapse of the BH subsystem is halted: the BH Lagrangian radii cease their inward movement and become roughly constant, while the number of BHs within the inner stellar Lagrangian radii also level off. It is at this time that the evolution of the observational structural parameters r_c and γ in Run 2 begins to strongly deviate from that in Run 1.

As noted above, prior to this point the evolution of Run 2 is observationally identical to that of Run 1. Neither the

retention of the BH population at $\tau \approx 10$ Myr, nor the subsequent orbital decay of these objects and the resulting formation of a compact central BH subsystem leads to differential evolution of r_c. This appears at odds with the models presented by Merritt et al. (2004), who investigated the possibility that the radius-age trend results from the formation of cores in primordially cusped star clusters due to the sinking and central accumulation of massive stellar remnants. We attribute our differing results to the much higher degree of central mass concentration in the cusped models of Merritt et al. (2004), which thereby respond more strongly and more rapidly to the perturbations induced by sinking remnants than does our initially cored, relatively low density Run 2. Merritt et al. (2004) also mentioned the possibility of additional cluster expansion due to the subsequent evolution of the BH population, once the central subsystem had formed. As discussed below, *all* of the expansion observed in our models is the result of such processes.

The number of stable BH binaries in Run 2 peaks at 5 at $\tau \approx 890$ Myr. After this point, there are $0-5$ BH binaries at any given time (Fig. 7a). Once formed, a BH binary undergoes superelastic collisions with other, usually single, BHs in the central core (although BH binaries do also occasionally collide with each other). On average, as BH binaries participate in such interactions they become "harder" (more tightly gravitationally bound), with the released binding energy being carried off by the interacting BHs (e.g., Heggie 1975; Heggie & Hut 2003). In each such interaction, the binary BH also has a recoil velocity imparted to it, the magnitude of which is dependent on how energetic the interaction has been. Together, these processes result in the *scattering* of BHs outside r_c, often into the cluster halo. As a given binary becomes increasingly tightly bound, so too can the collisions in which it is involved become increasingly energetic, such that an interacting BH carries off sufficient kinetic energy that it escapes from the cluster altogether. Eventually the BH binary is sufficiently hard that the recoil velocity it receives during a collision is larger than the cluster escape velocity, and the binary escapes as well. Hence, interactions in the central compact BH subsystem also result in the *ejection* of BHs from the cluster. For clarity we will retain the italicised terminology (*scattering* and *ejection*) henceforth.

These processes are evident in Fig. 7e, which shows the movement of three typical BHs during Run 2. Each of the three is born well outside r_c, but all sink to the central core via dynamical friction, as described above. Two are already present there by the time the first BH binaries are formed. All three of the BHs are frequently scattered to r_c (dot-dashed line) during their evolution in the cluster, and at least once each into the cluster halo. One is ejected from the cluster at $\tau = 7900$ Myr due to a strong interaction in the core. Another becomes a member of a BH binary at $\tau = 6200$ Myr, and subsequently undergoes four strong interactions (including one in which its partner is exchanged), with increasing recoil velocity each time until this is sufficient for ejection at $\tau = 8200$ Myr.

Considering Fig. 7c, it is clear that at any given time there are always a handful of BHs outside the 10 per cent stellar Lagrangian radius. This is an indication of the ongoing scattering of BHs to outside $\sim r_c$, since any ejected BHs tend to escape the cluster quite rapidly. As is evident from Fig. 7e, a scattered BH gradually sinks back into the

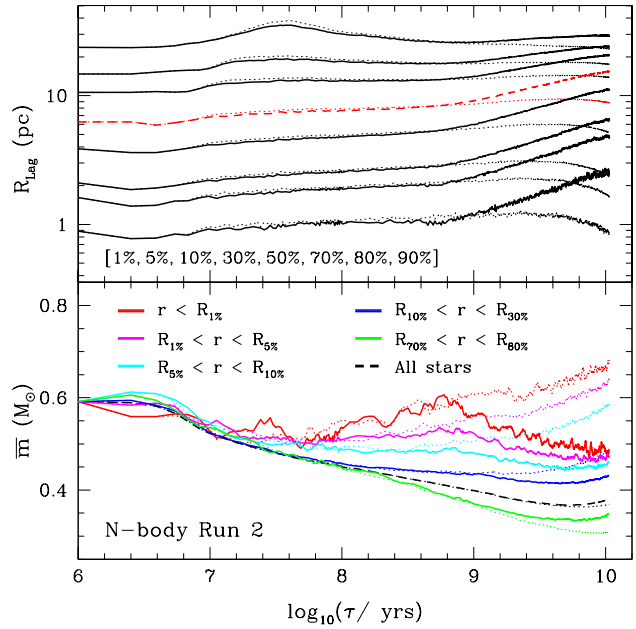

Figure 8. Evolution of various Lagrangian radii (top panel) and the mean stellar mass in the shells encompassed by selected Lagrangian radii (lower panel) for Run 2. The radii displayed in the top panel are, from inner to outer, the 1%, 5%, 10%, 30%, 50% $= r_h$ (dashed line), 70%, 80%, and 90% radii. In the lower panel the shells are defined by: $r \leqslant R_{1\%}$, $R_{1\%} < r \leqslant R_{5\%}$, $R_{5\%} < r \leqslant R_{10\%}$, $R_{10\%} < r \leqslant R_{30\%}$, and $R_{70\%} < r \leqslant R_{80\%}$ (these are listed in order from the upper to lower solid lines at the right hand side of the panel). The dashed line is the mean mass for all stars in the cluster. The evolution of Run 1 is marked by dotted lines, for comparison (note that the abscissa does not extend to such late times as are plotted in Fig. 6).

cluster centre via dynamical friction, thus transferring its newly-gained energy to the stellar component of the cluster. Most is deposited within r_c, where the stellar density is greatest. The ejection of BHs also transfers energy to the cluster, since a mass m escaping from a cluster potential well of depth $|\Phi|$ does work $m|\Phi|$ on the cluster. This mechanism is particularly effective in heating the stellar core, since BHs are ejected from the very centre of the cluster, and the energy contributed to each part of the cluster is proportional to the contribution which that part makes to the central potential (see e.g., Heggie & Hut 2003). In addition, here $m_{\rm BH}$ is significantly larger than m_*.

Together these two processes heat the stellar core of the cluster, resulting in significant core expansion. This becomes evident observationally at $\tau \approx 650$ Myr, and continues as long as the BH population is dynamically active – in the case of Run 2, the simulation was halted before the expansion ceased. From Fig. 5, the size of r_c is roughly proportional to $\log \tau$, consistent with the shape of the upper envelope of the observed cluster distribution. However, in this N-body model the expansion begins too late for the evolution to trace the upper envelope exactly; rather, it runs parallel.

The evolution of the stellar Lagrangian radii in Run 2 is illustrated in Fig. 8, along with the evolution of the mean stellar mass in the same Lagrangian shells examined earlier for Run 1. The progress of Run 1 is also marked on Fig. 8

for comparative purposes (dotted lines). As noted above, the initial infall and accumulation of BHs in the cluster centre does not cause any differential expansion of Run 2 over Run 1 at any radii. It is only after BH binaries are formed and the BH population becomes dynamically active that expansion occurs in Run 2. This expansion is evident at all radii, although the magnitude is greatest in the central regions of the cluster. None of the Lagrangian radii expand by as great a factor over the simulation as does r_c. The explanation for this can be seen in the lower panel of Fig. 8 – the development of mass segregation amongst the stellar component in Run 2 is severely inhibited by the activity of the BH population, compared to Run 1. This results in a larger apparent expansion in r_c than in the innermost stellar Lagrangian radii because of the luminosity weighting inherent in the measurement of r_c.

The process of mass segregation in Run 2 is only suppressed after the BH population becomes dynamically active. Up until this point, segregation has been proceeding just as in Run 1; however, after $\tau \approx 650$ Myr, no further stratification occurs. Stellar evolution subsequently reduces the mean mass in each Lagrangian shell with time. This interpretation is consistent with the cluster expansion processes due to BH scattering and ejection which were described above. In particular, the repeated BH scattering-sinking cycles constantly stir up the stellar component of the cluster and hence hinder the development of mass segregation, particularly in the inner cluster regions. The stratification which occurs before the BH population becomes dynamically active is not reversed however – there is still clearly a mean-mass gradient from the inner to the outer regions of the cluster at all times.

A useful quantity for examining the evolution of the cluster structures in Runs 1 and 2 is the ratio of the core radius to half-light (or half-mass) radius (e.g., Vesperini & Chernoff 1994; Trenti et al. 2007; Heggie et al. 2007; Hurley 2007). In regards to the latter of these radii, the relevant observational parameter is the projected radius containing half the cluster light ($r_{h,l}$). This is straightforward to calculate for the EFF family of models. The enclosed luminosity as a function of projected radius r_P may be obtained by integrating Eq. A2 within a cylinder of radius r_P along the line of sight (e.g., Eq. 11 in Mackey & Gilmore 2003a):

$$L(r_P) = \frac{2\pi\mu_0}{\gamma - 2}\left[a^2 - a^\gamma\left(r_P^2 + a^2\right)^{-(\gamma-2)/2}\right] \ . \quad (5)$$

When $r_P = r_{h,l}$ the enclosed luminosity is half of the total luminosity, i.e. $L(r_{h,l})/L_{\rm tot} = 1/2$. Substituting this into Eq. 5 and rearranging the result leads to an expression for $r_{h,l}$:

$$\log(r_{h,l}^2 + a^2) = \frac{2}{2-\gamma}\log\left(\frac{1}{a^\gamma}\left[\frac{L_{\rm tot}(2-\gamma)}{4\pi\mu_0} + a^2\right]\right) \ . \quad (6)$$

Projected half-light radii, along with the ratios $r_c/r_{h,l}$ may hence be calculated for the LMC and SMC cluster samples of Mackey & Gilmore (2003a,b) using their best-fitting EFF models and total luminosity estimates. Directly comparable quantities may also be calculated at each output time for our N-body Runs using the "observed" EFF models. In this procedure, for the purposes of direct comparison we do not use $L_{\rm tot}$ as calculated by the N-body code, but rather the total luminosity enclosed within some limiting observational radius, as specified in Mackey & Gilmore (2003a).

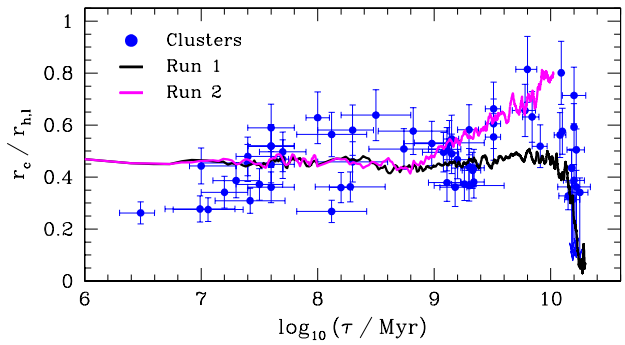

Figure 9. Evolution of the ratio of core radius to projected half-light radius $r_c/r_{h,l}$ for N-body Runs 1 and 2, compared with measurements for LMC and SMC clusters. Note that the measured ratios for the oldest, most compact LMC clusters are upper limits, reflecting the upper limits to the core radius measurements for these clusters (cf. Fig. 1).

The evolution of $r_c/r_{h,l}$ for Runs 1 and 2, compared with the measurements for LMC and SMC clusters, may be seen in Fig. 9. For much of Run 1, this ratio is a stable quantity at $r_c/r_{h,l} \approx 0.45$. As this model enters core collapse, however, the ratio shrinks to become very small. This is very similar behaviour to that observed by previous authors – in particular Hurley (2007), who measured the evolution of an identical (observationally defined) quantity in his large N-body models. Very different behaviour is observed for Run 2, however. As soon as the BH population in this model becomes active and core expansion begins, $r_c/r_{h,l}$ begins to steadily increase. This presumably reflects the increased heating efficiency of the BH population within the stellar core, as compared with the heating efficiency at larger radii in the cluster (cf. Fig. 8). By the end of Run 2 $r_c/r_{h,l} \sim 0.8$, matching the values observed for several of the most extended Magellanic Cloud clusters. These observations are consistent with the results of Hurley (2007), who found that even the presence of one BH-BH binary can prevent the expected decrease in $r_c/r_{h,l}$ – in our models the presence of many BHs results in a significant *increase* in this ratio. It has been suggested that a cluster with a large value of $r_c/r_{h,l}$ may harbour a central IMBH (see the extensive discussion presented by Hurley 2007); however, our Run 2 clearly demonstrates that the presence of a population of stellar-mass BHs can also lead to large values of this ratio.

Returning to Fig. 8, one significant point of note is that although the spatial distribution of stellar mass is quite different in Run 2 compared to Run 1, the overall mean stellar mass in Run 2 (dashed line) remains almost exactly the same as that in Run 1 throughout the simulation. Given that the initial stellar populations in the two models were identical, this indicates that the typical mass of a star escaping across the tidal radius in the two runs is very similar. Calculating the mean mass of all escaping stars in Run 1 between $\tau = 100$ Myr (when the early violent relaxation is essentially complete) and $\tau = 10667$ Myr (when Run 2 is terminated) reveals a value of $0.328\,{\rm M}_\odot$, while the same calculation for Run 2 results in $0.332\,{\rm M}_\odot$. These two values are indistinguishable, which is remarkable given the strong divergence in the structural evolution of the two clusters. Inspection

of the distribution of velocities with which stars escape between $\tau = 100 - 10667$ Myr in each simulation reveals these also to be indistinguishable. Together these results imply that both models lose stars solely due to relaxation processes. There is only a tiny group of ~ 20 relatively high velocity stellar escapers in Run 2 (i.e., which have an escape velocity greater than that of the fastest escaper in Run 1) out of a total of more than 55 000 stellar escapers, indicating that stars interact closely with BH binaries only very rarely. Heating of the stellar component via close interactions between stars and BH binaries is therefore negligible – the hardening of BH binaries is driven solely through interactions with other BHs in the central subsystem.

It is also enlightening to consider the properties of the escaping BHs in Run 2. The cumulative number of escaped single and binary BHs is plotted in Fig. 7d. The approximate time at which core expansion begins, $\tau = 650$ Myr, is marked with a vertical dotted line. Some single BHs escape before this point – these are BHs which are formed in the outer regions of the cluster and drift across the tidal boundary due to the early violent fluctuations in the cluster's gravitational potential. After $\tau = 650$ Myr, once BHs begin to be ejected solely due to interactions in the central subsystem, it is clear that the cumulative numbers $N_{\rm e}$ of escaping single and binary BHs increase more slowly at later times – that is, that the escape rates decrease with time. Hypothesising that the time derivatives of these rates vary as $-1/\tau$ (i.e., that $dN_{\rm e}/d\tau \propto -\log\tau$) suggests a fit of the form $N_{\rm e}(\tau) = A_0 + A_1\tau - A_2\tau\log\tau$ to the cumulative distributions, where the A_i are coefficients derived in the fitting process. Best-fit curves of this form are also plotted in Fig. 7d (dashed lines). Clearly these are excellent matches to the observed cumulative distributions, indicating that the rates of single and binary BH escape do indeed both have time derivatives which vary as $-1/\tau$.

The BH escape rates decrease with time because the density of the central BH subsystem is also decreasing with time – this is evident from Fig. 7c, which shows that the inner BH Lagrangian radii follow a generally increasing trend throughout the majority of the simulation. The typical number of BHs in the central subsystem falls with time because of BH ejections (Fig. 7b), and these ejections also heat the BH core. Simultaneously, the stellar component of the cluster is becoming more extended, meaning that the gravitational potential at the centre of the cluster due to this component is becoming increasingly shallow. Together these processes lead to the density of the central BH subsystem decreasing, on average, with time. The mean BH-BH encounter rate also therefore decreases with time, meaning that the BH binary hardening rate decreases, as does the BH ejection rate, as observed.

The decreasing BH binary hardening rate also means that the BH scattering rate decreases with time. Together with the slowing BH ejection rate, this means that the stellar core is also less efficiently heated with time. This is reflected in the roughly logarithmic dependence of r_c on τ. Because the BH scattering and ejection rates decrease throughout the lifetime of Run 2, by the end of the simulation at $\tau_{\rm max} = 10.67$ Gyr, there is still a sizeable population of 65 single BHs and 2 binary BHs remaining in the cluster. This contrasts strongly with the results from early, more analytic, studies of the evolution of BH subsystems in globular clusters, which predicted depletion of any BH populations on timescales much less than the cluster lifetimes (Kulkarni, Hut & McMillan 1993; Sigurdsson & Hernquist 1993). The fact that the BH encounter rate decreases due to the interplay between the stellar component of the cluster and the BH population, as seen in our detailed numerical modelling, prolongs the life of the BH subsystem in a massive star cluster for much longer than previously appreciated.

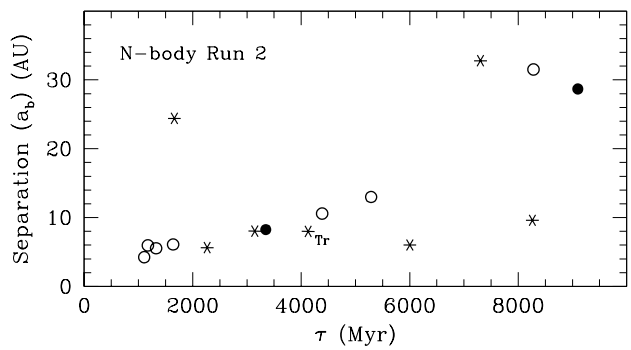

Figure 10. Separations and eccentricities of the ejected BH binaries in Run 2 as a function of cluster age. Eccentricity is represented by point style: BH binaries with $e \leqslant 0.8$ are asterisks, those with $0.8 < e \leqslant 0.95$ are open circles, while those with $e > 0.95$ are filled circles. The asterisk marked with 'Tr' is the innermost binary in the one ejected triple BH system (see text).

The properties of the ejected BH binaries in Run 2 complete the picture of BH evolution in this model. Over the course of the simulation, 15 BH binaries are ejected. Their separations (a_b) and eccentricities (e) are displayed in Fig. 10 as a function of cluster age. The hardest binaries are clearly ejected at the earliest times. This is when the cluster escape velocity ($v_{\rm esc}$) is largest – that is, when the binaries can be hardened to the greatest extent before the recoil velocity imparted during close interactions ejects them from the cluster. Typical separations are $a_b \approx 4 - 6$ AU for binaries ejected when $\tau < 2.5$ Gyr. As the cluster expands and loses mass, $v_{\rm esc}$ decreases and BH binaries are ejected before becoming this hard. For $\tau > 5$ Gyr, a_b is typically $10 - 30$ AU. There is no strong pattern in eccentricities of ejected BH binaries – there are six with $e \leqslant 0.8$, seven with $0.8 < e \leqslant 0.95$, and only two with $e > 0.95$. The maximum eccentricity of an ejected binary is $e = 0.972$. The BHs which are members of ejected binaries have a mean mass of $10.98\,{\rm M}_\odot$. This is more massive than the overall mean for BHs in Run 2, which have masses distributed uniformly in the range $8 \leqslant m_{\rm BH} \leqslant 12\,{\rm M}_\odot$.

In addition to the 15 BH binaries, one triple BH system is ejected from Run 2, at $\tau \approx 4100$ Myr. This consists of a tight low-eccentricity binary ($a_b = 8$ AU, $e = 0.376$) with a single BH bound in a wider low-eccentricity orbit ($a_b = 149$ AU, $e = 0.370$).

Previous studies have demonstrated that binary BHs ejected from massive star clusters can have orbital properties that would lead them to coalesce within a Hubble time due to the emission of gravitational radiation (see e.g., Portegies Zwart & McMillan 2000). Such objects may therefore be possible candidates for detection by gravitational wave experiments. An approximate formula

for the time-scale for a BH binary to coalesce due to the emission of gravitational radiation is given by (e.g., Portegies Zwart & McMillan 2000):

$$T_{\rm coal} \approx 3.2 \times 10^8 \left(\frac{\rm M_\odot}{m_{\rm BH}}\right)^3 \left(\frac{a_b}{\rm AU}\right)^4 \left(1-e^2\right)^{\frac{7}{2}} \ {\rm Gyr}. \qquad (7)$$

It is easy to show that none of the ejected BH binaries in Run 2 would merge within a meaningful time-scale (here we adopt $\sim$ 12 Gyr, which is the approximate age of the Universe minus the delay of $\sim$ 1.5 Gyr before the first BH binary ejections occur in Run 2). The most tightly bound ejected binary has $a_b = 4.2$ AU and $e = 0.839$, while the most eccentric ejected binary has $a_b = 8.2$ AU and $e = 0.972$. Even so, the orbital parameters of these objects are not vastly different from those which would lead to merging events on an interesting time-scale. For example, the binary with $e = 0.972$ would need $a_b = 1.06$ AU to merge in 12 Gyr, while that with $a_b = 4.2$ AU would need $e = 0.994$. We consider this topic further in Sections 4.2 and 5.

Recent large-scale N-body simulations have demonstrated comprehensively that when an intermediate-mass black hole (IMBH; mass $\sim$ a few $\times 10^3 {\rm M}_\odot$) is present in a massive star cluster, a central stellar density and velocity cusp develops about this object (e.g., Baumgardt, Makino & Ebisuzaki 2004a,b). It is natural to ask whether a similar cusp develops in Run 2, where a comparable BH mass is concentrated in the cluster centre, but in the form of many relatively small objects rather than one massive object.

Fig. 11 summarises the structural and dynamical state of the stellar component of Run 2 at two output times: $\tau = 5$ Gyr and $\tau = 10$ Gyr. These are late enough that any cusp should have had sufficient time to form (see e.g., the time-scales in Baumgardt et al. 2004a,b). The top panels in Fig. 11 show the 3-dimensional radial mass density profile of the cluster at the two output times (solid circles). All luminous matter in the cluster was counted in each profile (i.e., BHs were excluded). The radial bins contain 50 stars for radii closest to the cluster centre, graduating to 100 stars, then 500 and 1000 stars at increasingly large radii.

For comparative purposes, we have also plotted deprojected EFF models in these panels. These models are of the form of Eq. A2. In calculating them, we used the values of μ_0, a, and γ observed from the projected brightness profile at the appropriate time, as described in Section 3. The maximum radial extent of the projected brightness profiles is marked in Fig. 11 by vertical dotted lines. Agreement between the models and data is not necessarily expected beyond these radii; in addition, tidal effects become important at the largest radii. For convenience (see below), we took γ in the deprojected models to be the closest integer value to that observed – that is, $\gamma = 4$ at $\tau = 5$ Gyr, and $\gamma = 6$ at $\tau = 10$ Gyr. In each deprojected EFF model, the central surface luminosity density, μ_0, was converted to the volume luminosity density j_0 via Eq. A2. For example, at $\tau = 5$ Gyr, we measured $\mu_0 = 0.55\,{\rm mag\,pc^{-2}} = 51.05\,{\rm L_\odot\,pc^{-2}}$, which corresponds to $j_0 = 4.59\,{\rm L_\odot\,pc^{-3}}$. To obtain a mass density from this value requires multiplication by a global mass-to-light ratio appropriate for the age and metal abundance of the cluster. We determined this empirically by fitting the deprojected EFF model to the measured data. The resulting mass-to-light ratios ($M/L = 1.33$ at $\tau = 5$ Gyr, and $M/L = 2.01$ at $\tau = 10$ Gyr) are a good match for those calculated by directly summing the mass and luminosity of all stars in the cluster, excluding BHs ($M/L = 1.35$ at $\tau = 5$ Gyr, and $M/L = 2.10$ at $\tau = 10$ Gyr). We note that the assumption of a globally constant mass-to-light ratio is a reasonable approximation for Run 2 at these late times due to the relatively low degree of mass segregation amongst the stellar component of this cluster.

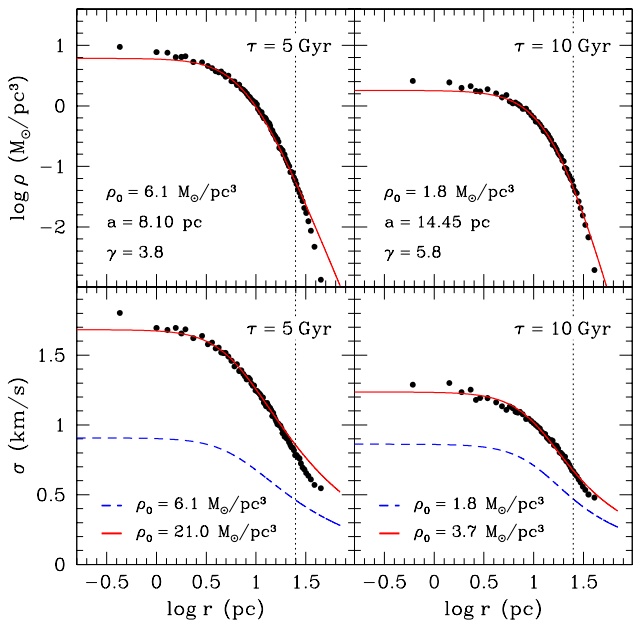

Figure 11. Radial mass density profiles and 1D velocity dispersion profiles for Run 2 (upper and lower panels, respectively) at cluster ages of 5 Gyr and 10 Gyr (left and right panels, respectively). In all panels, data from the simulation are marked with solid black circles. *Only stars were used to derive these measurements – BHs were excluded.* In the upper panels, the solid line indicates a deprojected EFF model fit using parameters set by those observed from the simulation at the appropriate output time. The vertical dotted lines indicate the maximum radius used in the construction of projected brightness profiles when obtaining these observations (see Section 3). In each lower panel, the dashed line represents the velocity dispersion profile predicted by the EFF model plotted in the matching upper panel, while the solid lines represent the same models with rescaled central densities to fit the data (see text).

It is clear from Fig. 11 that no significant cusps are present in the cluster's stellar density profile at either time. At the most, it is possible that very marginal cusps exist, since the density profiles rise slightly above the EFF models (which have constant density cores) at the innermost few data points; however the significance of this "density excess" is very low. Certainly, striking cusps of the form of those observed by Baumgardt et al. (2004a,b) to develop about central IMBHs in clusters are not present.

In the lower panels of Fig. 11, we plot the 1D stellar velocity dispersion as a function of radius at the two output times. The same radial bins as in the density profiles were used. Again, although the central regions of these profiles show some point-to-point scatter, there is no evidence at either time of a significant central velocity cusp analogous

to the type observed by Baumgardt et al. (2004a,b) when an IMBH is present.

It seems likely that the absence of a stellar density and velocity cusp about the central BH subsystem in Run 2 is due to the fact that scattered and ejected BHs are constantly moving through the region where a cusp would be expected to develop. This region is hence constantly being disturbed so that stars cannot settle into a stable distribution about the central concentrated mass as they can when only a single high-mass object is present. Such a process is similar to the destruction of cusps in galactic nuclei by supermassive black holes; except in that case a single very massive binary BH typically does the damage (e.g., Merritt & Cruz 2001).

Since there is no evidence from the 3D radial profiles for any large central density or velocity cusps, the projected profiles which it is possible to observe for real clusters will certainly show no evidence for any cusps. This is supported by the surface brightness profiles calculated at each output time in Run 2 to measure r_c and γ, which exhibit constant density cores as observed for the majority of LMC and SMC clusters (Mackey & Gilmore 2003a,b).

Is there therefore another means by which we might infer observationally the presence of the significant central BH population in Run 2? The lower panels in Fig. 11, together with Fig. 12 sketch the principles of one potentially viable method. In each of the lower panels in Fig. 11, we plot the stellar velocity dispersion profile predicted by taking the parameters (ρ_0, a, γ) from the nicely-fitting deprojected EFF density model marked in the respective top panel. Since we chose integer values of γ, the predicted velocity dispersion profiles are analytic, and easily computed. That for $\gamma = 6$ is given by Eq. A14, while the $\gamma = 4$ case is the well known Plummer sphere:

$$\sigma^2(r) = \frac{2\pi G \rho_0 a^2}{9\sqrt{1+\frac{r^2}{a^2}}} \,. \tag{8}$$

The resulting velocity dispersion profiles are plotted with dashed lines in the lower panels of Fig. 11. Clearly they are a very poor fit to the measured profiles. However, simply rescaling the central density ρ_0 so that the central velocity dispersion predicted by the deprojected EFF model is consistent with the innermost measured data points results in rather nice fits (solid lines), at least out to large radii where the external tidal field begins to affect the stellar dynamics. The required central densities at 5 and 10 Gyr are, respectively, ≈ 3.4 and ≈ 2.1 times those determined from the density profiles in the upper panels. This clearly implies that unseen matter (i.e., the BH population) is influencing the stellar dynamics in the cluster. By measuring the velocities of stars in an extended cluster, we might therefore be able to infer the presence of a retained BH population.

Such measurements are difficult. Apart from any technical intricacies, we are limited to working in projection and, with present technology, to using line-of-sight velocities only. The left panel of Fig. 12 shows the dispersion in the line-of-sight velocities in Run 2 at $\tau = 5$ Gyr as a function of projected radius. As previously, all luminous matter in the cluster was counted in the profile, but BHs were excluded. The radial bins contain 50 stars for radii closest to the cluster centre, graduating to 100 stars, then 500 and 1000 stars at increasingly large projected radii. Wilkinson et al. (2002)

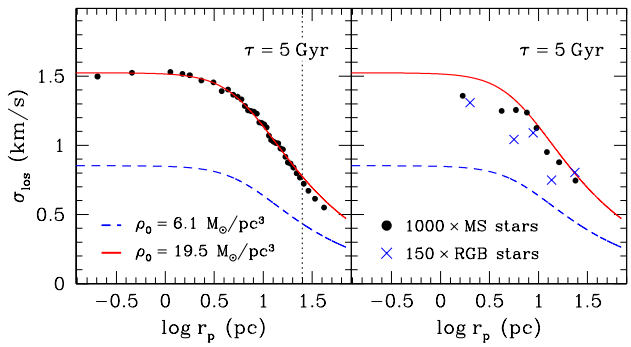

Figure 12. Dispersion in the line-of-sight velocities in Run 2 at $\tau = 5$ Gyr, as a function of projected radius. In the left panel, data from the simulation are marked with solid black circles. *Only stars were used to derive these measurements – BHs were excluded.* The dashed line represents the dispersion profile predicted by a Plummer sphere with central density taken from the profile in the upper left panel of Fig. 11. The solid line represents the same model with a rescaled central density (see text). In the right panel dispersion profiles from two stellar sub-samples are plotted: solid dots are for a sample of 1000 upper main sequence stars, and crosses are for a sample of 150 red giant branch stars. The two models from the left-hand panel are also marked.

provide an expression for $\sigma_{\rm los}(r_p)$ in a Plummer sphere (their Eq. 27 and 28). In the simplest case of an isotropic mass-follows-light model their expression reduces to:

$$\sigma^2_{\rm los}(r_p) = \frac{\pi^2 G \rho_0 a^2}{16\sqrt{1+\frac{r_p^2}{a^2}}} \,, \tag{9}$$

which has the same functional form as $\sigma^2(r)$, but a slightly smaller central value: $\sigma^2_{\rm los}(0) \approx 0.88\sigma^2(0)$. This suggests that the dynamical signature we observed from the lower panels of Fig. 11 should still be visible in projection, and indeed we find this to be the case. In the left panel of Fig. 12 we fit a model of the form Eq. 9 to the data (solid line), again leaving ρ_0 as a free parameter. In this case we find $\rho_0 = 19.5 {\rm M}_\odot$, which is very similar to the value required to fit the deprojected velocity data, but very different from the value implied from the radial density profile. We also computed a model using this latter value ($\rho_0 = 6.1 {\rm M}_\odot$); this is the dashed line in the left panel of Fig. 12.

The difference between the two models is sufficiently large that it may be detectable in clusters using presently available technology. In the right panel of Fig. 12 we plot $\sigma^2_{\rm los}(r_p)$ determined using two samples of stars randomly selected from Run 2. The first is a sample of 1000 upper main sequence stars grouped into six bins of 125 stars, while the second is a sample of 150 red giant branch stars grouped into five bins of 30 stars. Both samples clearly favour the model with the larger mass-to-light ratio. The red-giant sample is of a size which could feasibly be measured by a modern multi-object spectrograph such as VLT/FLAMES, although it must be borne in mind that the typical measurement errors in radial velocities observed with such a facility will be at least comparable in magnitude to the dispersion in a diffuse cluster ($\sim 1-2$ km s^{-1}) – a sophisticated analysis would be required to properly account for these.

While somewhat crude, our results demonstrate that

in a cluster such as that modelled in Run 2, where there is a relatively large BH population present, *the stellar dynamics should imply the presence of significantly more mass than is evident from observations of the luminous component of the cluster*. This arms us with a means of searching, albeit indirectly, for BH populations in massive LMC and SMC star clusters. Even so, we expect such observations to be extremely challenging due to the small velocity dispersions involved, the necessity of working in projection, and the general sparsity (in terms of numbers of bright stars) of the extended clusters observed in the Magellanic Clouds.

4.2 Runs 3 and 4: Strong mass segregation

We next consider the pair of simulations labelled Run 3 and Run 4. These are both strongly primordially mass segregated clusters, created as described in Section 2.2 using a pre-evolution duration of $T_{\rm MS} = 450$ Myr. This duration was selected so that Runs 3 and 4 possess initial properties very similar to those observed for the very young, compact cluster R136 in the 30 Doradus complex in the LMC (see below).

Like Runs 1 and 2, Runs 3 and 4 start with identical initial conditions, to the extent that they share the same random seed. Once again, the sole difference between them is that in Run 3 the natal BH kicks are set to be $v_{\rm kick} \approx 200$ km s^{-1}, whereas in Run 4 they are set to be zero – this results in $f_{\rm BH} = 0$ and $f_{\rm BH} = 1$, respectively.

The primary aim of Runs 3 and 4 is to try and follow the evolution of models which look more similar to the very youngest ($\tau \lesssim 20$ Myr) massive LMC and SMC clusters than do Runs 1 and 2. In particular, as discussed in Section 2.2, a number of very young Magellanic Cloud clusters have been observed to be mass segregated to some degree. However, significant mass segregation does not develop in Runs 1 and 2 until $\tau \sim 100$ Myr or so. In addition, the projected brightness profiles of Runs 1 and 2 (and particularly the structural parameters r_c and γ) do not resemble observed young LMC and SMC clusters until $\tau \approx 20$ Myr (e.g., Fig. 5). These differences mean that the observed early evolution of Runs 1 and 2 may not accurately reflect the processes occurring in the youngest massive Magellanic Cloud clusters.

Furthermore, in Run 2 we found that the BH population did not influence the structural evolution of the cluster until after the formation of the first BH binaries in the core at $\tau \approx 510$ Myr. Since Fig. 1 shows that there is clearly evolution in the observed radius-age trend on time-scales shorter than this, it is important to examine whether it is possible for the BH population to become dynamically active earlier than seen in Run 2. One might naively expect this to occur if BHs are formed preferentially at the centre of a cluster, such as they would be in a primordially mass segregated object.

It is important to first assess the suitability of the initial conditions we constructed for Runs 3 and 4 before moving on to an examination of the evolution of these Runs. One simple but useful indication is provided by the observed initial structural parameters r_c, γ, and ρ_0. The measured values for Runs 3 and 4 are listed in Table 1. As described previously, these quantities are an excellent match for those determined for R136; see also Fig. 3. We note however, that R136 is nearly an order of magnitude more massive than our N-body models. Scaling issues are discussed in Section 5.

One of the major differences between Runs 3 and 4 and Runs 1 and 2 is that the former have very much larger central densities than the latter. This is simply due to the strong central concentration of the most massive stars in Runs 3 and 4 as a result of the initial mass segregation. It is enlightening to examine the early evolution of the central densities in these differing models – this evolution is plotted for Runs 1 and 3 in Fig. 13. At the start of the simulation, the density of Run 3 is directly comparable to that of R136; however, as the early phase of severe mass loss due to stellar evolution begins, the central density drops rapidly so that by ~ 10 Myr it matches the densities observed for other young LMC and SMC clusters. This rapid drop in central density implies that the central regions of the cluster expand during this early period of evolution, and indeed this is what is observed (see below). In comparison, the initial central density of Run 1 is much lower than that of R136, and does not change much as the rapid early stellar evolution progresses. This is consistent with the fact that Run 1 shows little or no central expansion during this phase. Together, Runs 1 and 3 span the range of central densities observed for the youngest LMC and SMC clusters – we are therefore confident of the applicability of our models in this regard.

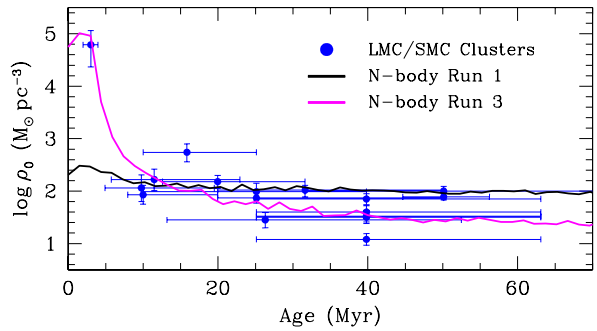

Figure 13. Early evolution of the central density ρ_0 for Run 1 and Run 3. Run 1 has no primordial mass segregation while Run 3 is strongly primordially segregated. Run 3 appears very similar to R136 at early times; however by a few tens of Myr its central density has decreased significantly and is a good match to LMC and SMC clusters of this age. Run 1 starts with a much lower central density, which it maintains throughout its early evolution. Together these two models span the observed density ranges for the youngest LMC and SMC objects.

It is also possible to assess how well the primordial mass segregation generated in Runs 3 and 4 matches that observed in genuine young Magellanic Cloud clusters. We do this by performing simulated observations of the radial variation of the stellar mass function (MF) in the models, and comparing the results to those determined from the detailed observational studies of Hunter et al. (1995, 1996) for R136 (~ 3 Myr old); that of de Grijs et al. (2002a) for NGC 1805 (~ 10 Myr old) and NGC 1818 (~ 20 Myr old); and that of Sirianni et al. (2002) for NGC 330 (~ 30 Myr old).

In performing the simulated observations, we follow the individual cluster studies as closely as possible. That is, we use the same projected radial bin widths and the same stellar detection limits within each such bin as were used in the original observational study. This ensures that our measurements are closely comparable to those obtained in each. Consider, for example, the work of Sirianni et al. (2002).

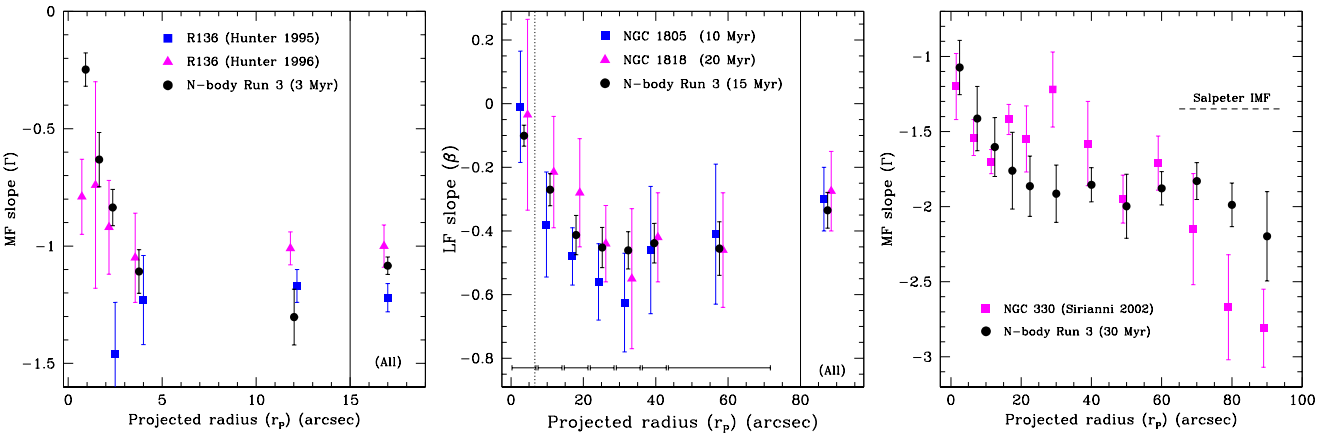

Figure 14. Mass and luminosity function slopes as a function of projected radius for various young massive LMC and SMC clusters, compared with results from simulated observations of N-body Run 3. The plots have been reproduced to match those presented for each cluster by the original authors. **Left:** Mass function slope Γ as a function of projected radius in R136 in the LMC from Hunter et al. (1995, 1996), compared with Run 3 at age 3 Myr. **Centre:** Luminosity function slopes β as a function of projected radius for NGC 1805 and NGC 1818 in the LMC from de Grijs et al. (2002a), compared with Run 3 at age 15 Myr. **Right:** Mass function slope Γ as a function of projected radius in NGC 330 in the SMC from Sirianni et al. (2002), compared with Run 3 at age 30 Myr.

These authors used five annuli of $5''$ width to span the range $0-25''$ in projected radius in their study of NGC 330, followed by ten annuli of $10''$ width to span the range $25-125''$ in projected radius. Ultimately, however, they decided to employ a maximum projected radius of $95''$ for their MF calculations, due to a significant contaminating population of field stars. Within their radial bins, the stellar mass limits used to calculate the MF were from the top of the main sequence in this cluster ($\sim 7\,\mathrm{M}_\odot$) to the 50 per cent completeness level – at $\sim 1.3\,\mathrm{M}_\odot$ in the cluster centre, decreasing to $\sim 0.8\,\mathrm{M}_\odot$ at a projected radius of $25''$ and beyond. When measuring our model cluster for a comparison with the results of Sirianni et al. (2002), we took the data from the output time nearest to 30 Myr, projected the positions of all stars onto a plane, converted the projected radial scale from parsecs to arcseconds by applying the SMC distance modulus of 18.85 assumed by Sirianni et al. (2002), and then applied exactly the same bin widths and mass limits per bin as Sirianni et al. (2002) to obtain the stellar samples for MF fitting. Sirianni et al. (2002) corrected their star counts for completeness variations, so we assumed 100 per cent completeness in each radial bin. At our chosen output time, the core radius and central density of our model are within ~ 15 per cent of the values measured for NGC 330 (see Figs. 13 and 15), so the bins are sampling equivalent regions in the cluster.

The results of our simulated observations may be seen in Fig. 14, along with the original measurements for R136, NGC 1805 and 1818, and NGC 330. For R136 and NGC 330, the mass functions are represented by $\zeta(m)$, which is the number of stars per *logarithmic* mass interval, as opposed to the mass function $\xi(m)$ defined in Section 2.1. If the mass function $\xi(m)$ has a power-law exponent $-\alpha_i$, then the mass function $\zeta(m)$ will have exponent $\Gamma_i = -\alpha_i + 1$. In the case of NGC 1805 and 1818, we calculate and fit luminosity functions (LFs) rather than MFs, so as to match the work of de Grijs et al. (2002a). The assumed form of the LFs, defined here as the number of stars per logarithmic luminosity bin, is a power law of slope β.

From Fig. 14 it is clear that the results obtained via our simulated observations of Run 3 are generally an excellent match for those measured for the real LMC and SMC clusters. The greatest differences occur for the innermost radial bin of R136, and the outermost radial bins of NGC 330. The former discrepancy suggests that the very centre of Run 3 (within ~ 0.1 pc) may initially be somewhat more mass segregated than R136, although we note that the rest of our measurements are highly consistent with the real observations of R136, and that the region taken by Hunter et al. (1996) to obtain their measurement at the innermost radius is *extremely* crowded with bright stars. The latter discrepancy may be related to the necessity for significant field star decontamination in the outermost regions of NGC 330 by Sirianni et al. (2002) – again, we note that the majority our measurements of Run 3 are in excellent agreement with those obtained by these authors for NGC 330.

Overall, these results are strongly suggestive that the initial conditions we constructed for Runs 3 and 4, and in particular of the algorithm we developed to generate the primordial mass segregation in these models, are valid. We note however, that we are not able to place any similar observational constraints on the initial velocity distributions in these models. As an aside, it is extremely interesting to observe the progression of the radial mass/luminosity function profile of Run 3 from age $\tau = 3$ Myr to 30 Myr, in comparison with the profiles observed for four genuine LMC and SMC clusters. While there has previously been nothing to link the measurements of these four objects, the early evolution of Run 3 clearly demonstrates that a cluster which initially possesses a core radius, central density and radial MF profile very similar to that of R136 can evolve to look very much like NGC 1805 and NGC 1818 after 15 Myr and then further to look like NGC 330 after another 15 Myr, simply via internal cluster dynamical processes under the influence of rapid mass loss due to stellar evolution.

In Fig. 15, we show the evolution of Runs 3 and 4 across the radius-age and γ-age planes. Unlike Runs 1 and 2, both Runs 3 and 4 exhibit dramatic core expansion right from the

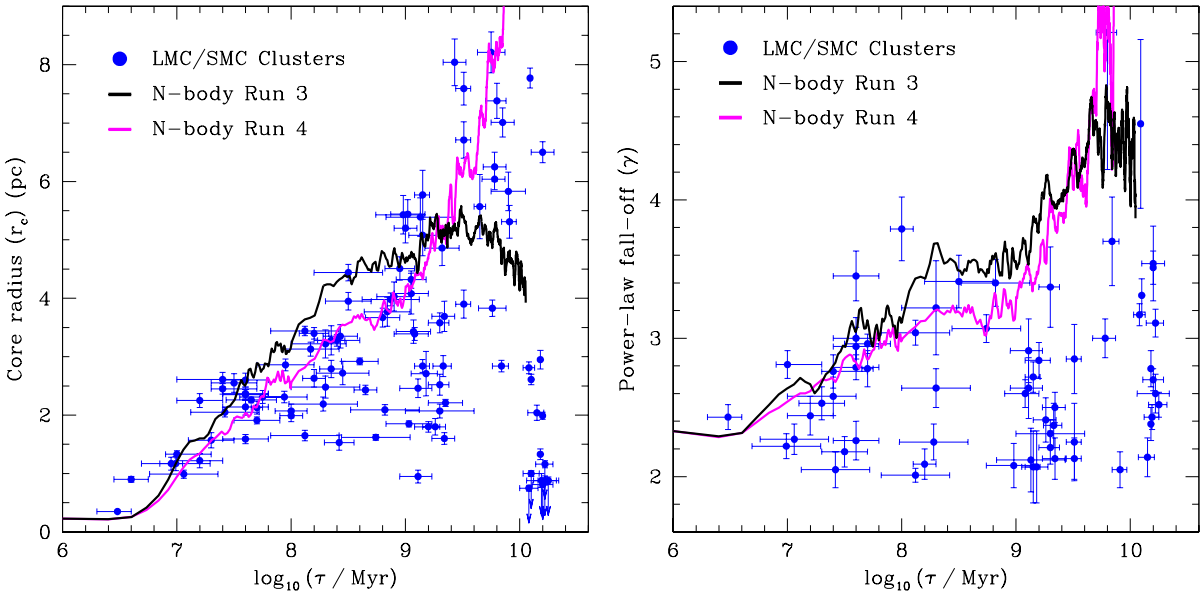

Figure 15. Structural evolution of N-body Runs 3 and 4. Both possess significant primordial mass segregation; the only difference between them is the BH retention fraction ($f_{\rm BH} = 0$ and 1, respectively). **Left panel:** Evolution of r_c, observed as described in Section 3. Both models experience significant expansion over the first ~ 200 Myr of evolution, due to the early phase of severe mass loss due to stellar evolution. This is in contrast to Runs 1 and 2, where the mass loss was spread throughout the cluster rather than being centrally concentrated. Subsequently, Run 3 begins to relax dynamically and slowly contracts, whereas the BH population retained in Run 4 becomes dynamically active, leading to further core expansion in this model. By $\tau_{\rm max} = 10$ Gyr, the core radius for Run 4 has moved off the top of the plot, to $r_c \approx 11$ pc. **Right panel:** Evolution of the power-law fall-off, γ, again observed as described in Section 3. Both models develop increasingly steep γ values as they evolve; however, that for Run 3 reaches a plateau once the core expansion in this model ceases. In contrast, Run 4 develops a very steep fall-off in its outer regions.

beginning of their evolution. This is in response to the early phase of severe mass-loss due to stellar evolution, which in Runs 3 and 4 is highly centrally concentrated because of the primordial mass segregation. Fig. 16 shows the radial distributions of all supernovae in Runs 1 and 3 – the more centralized location of these events in Run 3 compared with Run 1 is clearly evident. The central concentration of the mass-loss, together with the high central density in Runs 3 and 4, means that the amount of heating per unit mass lost is maximised in these models, hence leading to the observed dramatic core expansion. This core expansion is at least partly responsible for the rapid decrease in the central density of Run 3 which we noted in Fig. 13 (the demise of the most massive cluster stars also contributes to this decrease).

It is interesting that Runs 3 and 4 do not undergo an early core collapse despite their high central densities. Early core collapse in a massive cluster may lead to a runaway merger event, which is one possible formation channel for a central intermediate-mass black hole (IMBH) (e.g., Portegies Zwart & McMillan 2002; Portegies Zwart et al. 2004). Previous work has demonstrated that clusters with a very short initial median relaxation time are susceptible to early collapse – Portegies Zwart & McMillan (2002) suggest $t_{rh} < 25$ Myr. It is not clear whether a similar threshold is applicable to our primordially mass segregated models. These have very much longer initial median relaxation times ($t_{rh} \approx 1.2$ Gyr), but rather short central relaxation times ($t_{r0} \approx 9$ Myr). It is possible that expansion of the cluster core due to mass-loss from rapid stellar evolution acts against the tendency of the core to collapse more strongly in our models than in previous models, due to the initial preferentially central location of many massive stars.

By $\tau \approx 100$ Myr the rate of mass-loss from stellar evolution has significantly decreased, and by $\tau \approx 200$ Myr the core expansion in Runs 3 and 4 has largely stalled. Even though both models initially contain identical stellar populations, Run 3 loses more mass up to this point than does Run 4, because the 198 BHs in Run 3 escape from the cluster immediately after formation, whereas those in Run 4 are retained. This difference is reflected in the larger degree of early core expansion observed in Run 3 compared to Run 4. Up until an age of roughly a few hundred Myr, Run 3 closely traces the observed upper envelope of the radius-age trend.

In both models, the early mass-loss and core expansion is accompanied by a significant steepening in the outer power-law fall-off. This is again in contrast to the evolution observed for Runs 1 and 2 during the early mass-loss phase, where γ remains essentially constant. Similarly to the core-radius evolution in Runs 3 and 4, the steepening of γ stalls beyond $\tau \approx 100$ Myr in these models, once the rate of mass-loss has decreased. Furthermore, the evolution of γ up to this point is slightly different in the two models, due to the retention of BHs in Run 4 and their expulsion in Run 3.

Thereafter, Runs 3 and 4 begin to evolve quite differently. Run 3 progresses in exactly the fashion of Run 1 – the cluster settles into a quasi-equilibrium state where the dynamical evolution is dominated by two-body relaxation processes, leading to the gradual development of mass stratification. Because Run 3 is far less dense than Run 1 by this stage, its relaxation time-scale is much longer. By

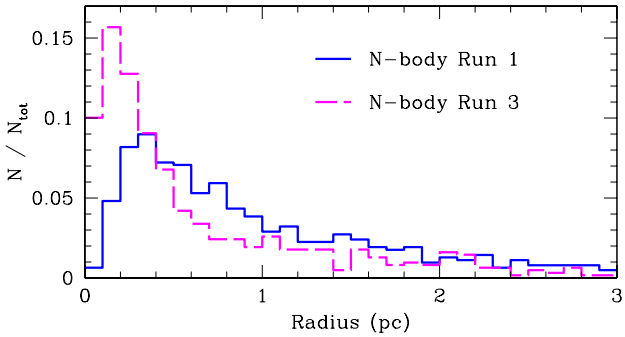

Figure 16. Radial distributions of supernova explosions in Run 1 (solid line) and Run 3 (dashed line). All supernova explosions in both models have occurred by $\tau \approx 50$ Myr. The significantly greater central concentration of the mass loss in Run 3 compared to Run 1 is quite evident.

$\tau_{\max} = 10.27$ Gyr, only 3.1 integrated median relaxation times have elapsed in this model, compared with 4.7 median relaxation times in Run 1 at the same age. Hence, while Run 3 is evolving towards core collapse when the simulation is terminated, we would expect it to enter this phase at a much older age than observed for Run 1.

In contrast, at $\tau \approx 750$ Myr, core expansion resumes in Run 4. This continues until the end of the simulation, which is terminated at $\tau_{\max} = 10.0$ Gyr. By this time, the core radius of Run 4 has evolved off the top of Fig. 15, to reach almost 11 pc. This is roughly comparable in size to the core radii observed for the most extended old Magellanic Cloud clusters, such as Reticulum in the LMC and Lindsay 1 in the SMC (Mackey et al. 2007, in prep.).

The second, prolonged, period of core expansion in Run 4 is due to the dynamical activity of its retained BH population. The evolution of this BH subsystem, illustrated in Fig. 17, is qualitatively identical to that which we observed in Run 2. The BHs, once formed, sink via dynamical friction and begin to accumulate at the centre of the cluster (panels b and c). The density of this central BH subsystem increases until it becomes sufficiently high as to initiate the creation of stable BH binaries in three-body interactions (panel a). The first such object is formed in Run 4 at ~ 570 Myr. Subsequently, these binaries undergo superelastic collisions with other BHs in the cluster centre, which leads to the hardening of the binaries, the scattering of BHs beyond r_c, and the ejection of BHs (panels d and e). These processes in turn result in the observed long-term core expansion.

One intriguing aspect of the evolution of the BH subsystem in Run 4 is that even though this cluster was strongly primordially mass segregated, so that the majority of the BHs were created in its very inner regions (cf. Fig. 16), the first BH binary does not form until a similar time as that in the non-segregated Run 2. From Fig. 17, it is also clear that the peak central BH density occurs at a similar time as it does in Run 2. Fig. 18 shows an expanded view of the early evolution of the BH Lagrangian radii in Run 4, with those for Run 2 plotted for comparison. As expected, the majority of BHs are formed near the centre of the cluster – the BH Lagrangian radii are initially much smaller than in Run 2. However, unlike Run 2, Run 4 suffers significant early core expansion due to the rapid stellar evolution phase. The BH subsystem does not escape this – the early centrally concentrated mass-loss is severe enough that the resulting expansion overcomes the natural tendency of the BHs to sink to the cluster core. This is reflected in the swift outward movement of the BH Lagrangian radii in Run 4, until the mass-loss phase is mostly complete around $\tau \approx 100$ Myr. Subsequently, the BHs do begin to sink to the cluster centre via dynamical friction, and the evolution of the BH Lagrangian radii in Run 4 closely follows that in Run 2.

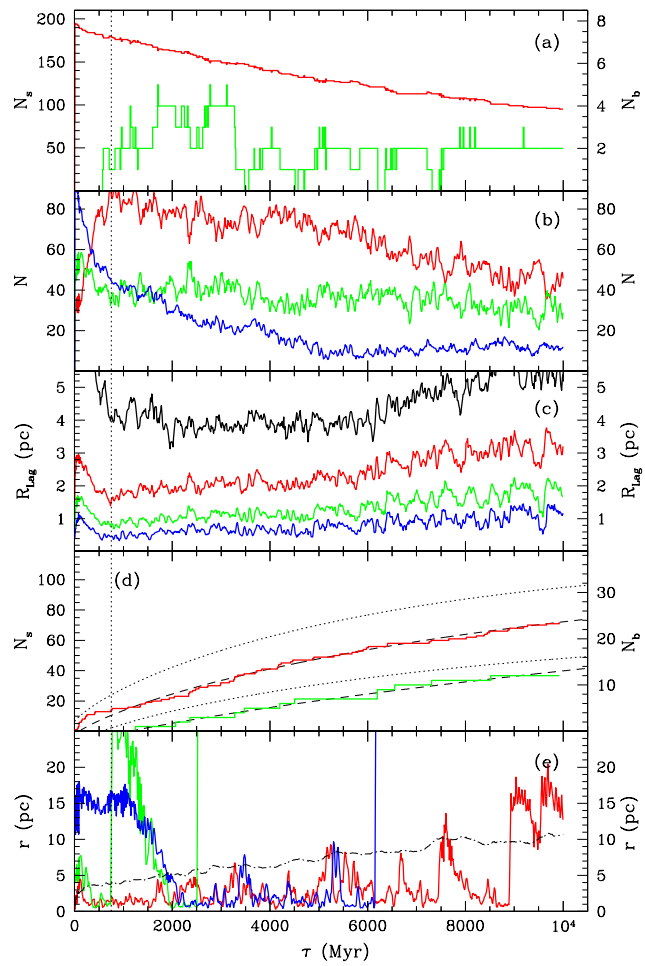

Figure 17. Properties of the BH population in Run 4 as a function of time: (a) the number of single BHs (upper line) and binary BHs (lower line) in the cluster; (b) the number of BHs within the shells encompassed by the *stellar* Lagrangian radii $r \leqslant R_{1\%}$, $R_{1\%} < r \leqslant R_{5\%}$, and $r > R_{10\%}$ (the uppermost to lowermost lines, respectively, at the right of the plot); (c) the *black hole* 10%, 25%, 50% and 75% Lagrangian radii (respectively, the innermost to outermost lines); (d) the cumulative numbers of escaped single BHs (upper line) and binary BHs (lower line), along with fits of the form $N_e = A_0 + A_1\tau - A_2\tau \log \tau$ (dashed lines) and the cumulative numbers of escaped single and binary BHs measured for Run 2 (dotted lines); and (e) the radial positions of three typical BHs. The vertical dotted line indicates $\tau = 750$ Myr, the approximate time when core expansion due to BH activity begins. The evolution of r_c is plotted (dot-dashed line) in panel (e). Note the different axis scales on either side of panels (a) and (d).

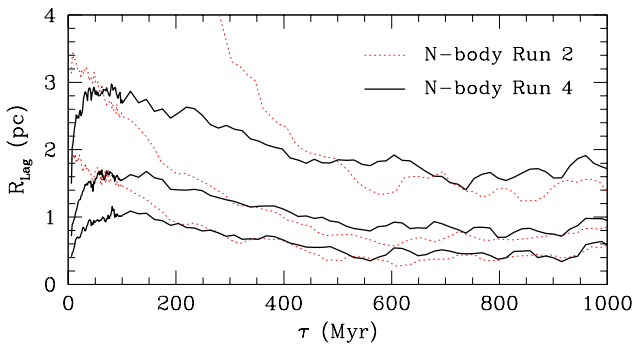

Figure 18. Evolution of the 10%, 25% and 50% BH Lagrangian radii in Run 4 (solid lines). The evolution of the same radii in Run 2 are plotted for comparison (dotted lines). This plot clearly shows that the BH subsystem in Run 4 *expands* at early times along with the rest of the core, in response to the rapid mass-loss from stellar evolution which is occurring. Once this phase is mostly complete ($\tau \approx 100$ Myr), the evolution of the BH subsystem is very similar to that in Run 2.

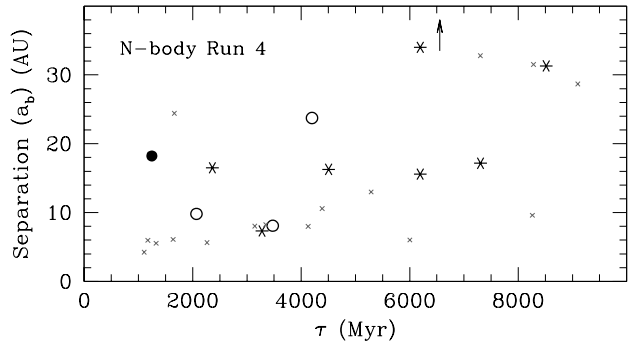

Figure 19. Separations and eccentricities of the ejected BH binaries in Run 4 as a function of cluster age. Eccentricity is represented by point style: BH binaries with $e \leqslant 0.8$ are asterisks, those with $0.8 < e \leqslant 0.95$ are open circles, while those with $e > 0.95$ are filled circles. The ejected BH binaries from Run 2 are plotted for comparison (small crosses). The arrow marks the ejection time of one additional Run 4 BH binary, which has separation $a_b = 56.4$ AU and eccentricity $e = 0.609$.

This result suggests that, contrary to expectations, the BH population in a primordially mass segregated or centrally concentrated cluster does not become dynamically active at significantly earlier times than does an identical population in a non-segregated cluster. In turn, this implies that the evolution in the radius-age trend observed on time-scales shorter than ≈ 500 Myr is not due to the influence of a BH population, unless such populations are comprised of BHs with masses significantly in excess of $10\,\mathrm{M}_{\odot}$. Instead, the early evolution of the radius-age trend most probably reflects centrally concentrated mass-loss in dense clusters due to rapid stellar evolution. Never the less, Runs 3 and 4 clearly demonstrate that this process cannot alone propel clusters to the upper right corner of Fig. 1, since it operates on a time-scale which is much too short. Our N-body models which possess core radii larger than ~ 6 pc after a Hubble time of evolution do so only because they have experienced prolonged core expansion due to the activity of a retained BHs, irrespective of whether they also experienced core expansion at ages $\tau \lesssim 100$ Myr.

As with Run 2, by $\tau_{\max} = 10.0$ Gyr there is still a significant BH population remaining in Run 4: 95 single BHs and 2 binary BHs. In fact, this population is rather larger than that in Run 2 at the same age. From Fig. 17d, it is clear that, while the cumulative numbers of escaped single and binary BHs in Run 4 follow the same functional dependence on age as in Run 2, they are, at all times, smaller than those in Run 2. That is, the rates of escape of BHs are always somewhat lower in Run 4 than they are in Run 2.

We attribute this variation to the different overall structures of Runs 2 and 4 when their respective BH populations become dynamically active. In Run 2 the core radius and central density remain nearly constant from the beginning of the simulation until this point (cf. Figs. 5 and 13); in contrast, Run 4 undergoes significant early core expansion. By $\tau = 500$ Myr, Run 4 is a considerably more diffuse cluster than is Run 2. The shallower gravitational potential in Run 4 affects the distribution of the BHs within this cluster (cf. Fig. 17c and Fig. 7c). This leads to a slower interaction rate between BHs in Run 4 than in Run 2, and hence the observed lower BH escape rates. The same effect is primarily responsible for the BH escape rate in a model cluster decreasing as the core radius increases (see Section 4.1), although in that case the decreasing size of the BH population contributes in addition.

The more diffuse nature of Run 4 also affects the properties of the ejected BH binaries in this simulation compared with those in Run 2. In Run 4, there are 12 BH binaries ejected over the course of the simulation. Their separations and eccentricities are plotted in Fig. 19, along with the ejected BH binaries from Run 2 for comparison. Because Run 4 is always more diffuse than Run 2 at times when binary BHs exist, these objects are more easily ejected in Run 4 than in Run 2. Hence, the ejected BH binaries in Run 4 are generally not as tightly bound as those in Run 2. This can be seen in terms of the binary separations in Fig. 19, which are typically larger for the ejected binaries in Run 4 than for those in Run 2 at similar times. In addition, the ejected BH binaries in Run 4 are typically less eccentric than those in Run 2 – of the 12 ejected Run 4 BH binaries, only one has $e > 0.95$, while there are three with $0.8 < e \leqslant 0.95$ and eight with $e \leqslant 0.8$. The maximum eccentricity of an ejected binary is $e = 0.981$, while the minimum is $e = 0.225$. As in Run 2, the members of ejected binaries are typically more massive than the average mass for the full BH population – the mean mass of members in escaping binaries in Run 4 is $11.20\,\mathrm{M}_{\odot}$. In Section 4.1, we showed that none of the ejected BH binaries from Run 2 would merge due to the emission of gravitational radiation within a Hubble time (Eq. 7). This is also, unsurprisingly, the case in Run 4.

Fig. 20 shows the evolution of the ratio of core radius to projected half-light radius, $r_c/r_{h,l}$, for Runs 3 and 4. Runs 1 and 2 are also plotted, for comparative purposes. The initial value of $r_c/r_{h,l}$ for Runs 3 and 4 is significantly smaller than that for Runs 1 and 2, reflecting the primordial mass segregation in these models. However, the early core expansion in Runs 3 and 4 results in a rapid and significant increase in $r_c/r_{h,l}$. Overall, Runs 3 and 4 better match the observed dis-

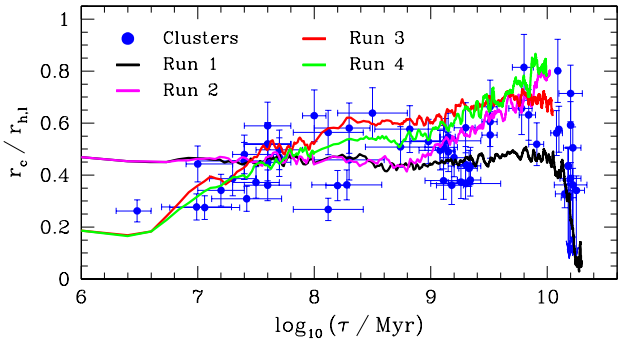

Figure 20. Evolution of the ratio of core radius to projected half-light radius $r_c/r_{h,l}$ for N-body Runs 3 and 4, compared with measurements for LMC and SMC clusters. The evolution of Runs 1 and 2 is also plotted, for comparative purposes.

tribution of young and intermediate-age Magellanic Cloud clusters than do Runs 1 and 2. By the end of Run 3, $r_c/r_{h,l}$ is beginning to decrease as two-body relaxation begins to dominate in this model; however, for the majority of this Run $r_c/r_{h,l} \sim 0.7$. This demonstrates that a large observed value of $r_c/r_{h,l}$ in a physically old star cluster need not reflect the presence of a central massive body (such as an IMBH) or a central accumulation of many less-massive bodies (such as stellar-mass BHs), but rather may reflect the fact that such a cluster is not very *dynamically* old. Run 4, which undergoes prolonged core expansion due to its BH population, finishes with $r_c/r_{h,l} \sim 0.8$, matching Run 2 closely.

4.3 Runs 4a and 4b: Variable mass segregation

As described at the beginning of Section 4, our four primary simulations cover the extremes of the parameter space we are investigating (spanned by $0 \leqslant f_{\rm BH} \leqslant 1$ and $0 \leqslant T_{\rm MS} \leqslant 450$ Myr), and are therefore expected to represent the extremes of cluster evolution induced by variation of these particular initial conditions. However, it is important to sample intermediate values of both $f_{\rm BH}$ and the degree of primordial mass segregation to check that the parameter space is well behaved and that the models evolve as we expect (i.e., intermediate between the extremes of Runs 1-4).

With this in mind, we completed two additional simulations with $f_{\rm BH} = 1$, and degrees of primordial mass segregation spaced between that for Run 2 and that for Run 4. Because the initial conditions for these new models were taken from two different output times during the pre-evolution of Run 4, at $T_{\rm MS} = 115$ Myr and 225 Myr, we denote them as Runs 4a and 4b, respectively. We only ran these models to $\tau_{\rm max} \sim 4.3$ Gyr, as this was more than sufficient to observe the progress of the clusters' evolution.

The initial properties of Runs 4a and 4b are listed in Table 1. As expected, the values of r_c, γ, and ρ_0 all lie between those of Runs 2 and 4. The longer the duration of the pre-evolution, the smaller the initial value of r_c, the higher the initial value of ρ_0, and the flatter the initial value of γ. This latter, in particular, is expected due to the development of a core-halo structure in a dynamically evolving cluster (see e.g., Spitzer 1987).

The core radius evolution of Runs 4a and 4b is illus-

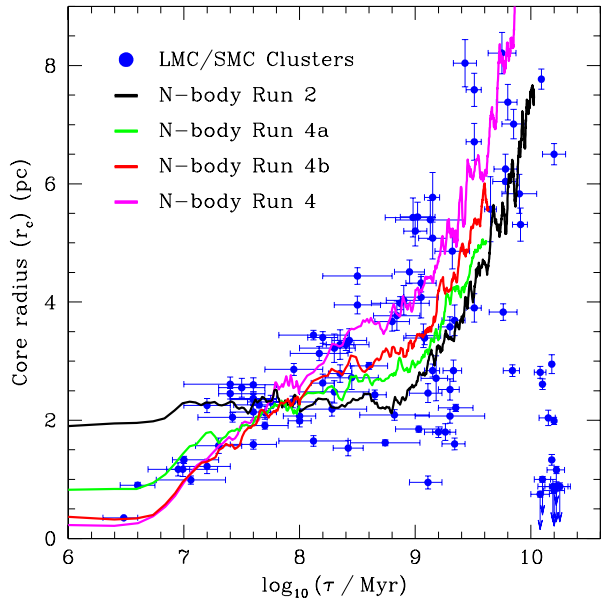

Figure 21. Core radius evolution of N-body Runs 4a and 4b, with the evolution of Runs 2 and 4 plotted for comparison. Runs 4a and 4b, with pre-evolution durations of $T_{\rm MS} = 115$ Myr and $T_{\rm MS} = 225$ Myr, possess primordial mass segregation of degrees intermediate between those of Runs 2 and 4. This initial condition is the only difference between each of the four plotted Runs – all four form 198 BHs and have a BH retention fraction of $f_{\rm BH} = 1$.

trated in Fig. 21. Just as with Run 4, these two models undergo two main stages of core expansion. The first, lasting until a little after ~ 100 Myr, is in response to the early rapid stellar evolution. The second, which begins around $\tau \approx 600 - 800$ Myr is due to the influence of the retained BH population. In between these two phases, there is a period during which the core radius is roughly constant.

As expected, the core radius evolution seen for both Runs 4a and 4b lies between the limits defined by Runs 2 and 4. The amount of early expansion apparently varies directly with the degree of primordial mass segregation – the more mass segregated a cluster, the larger the core expansion seen at ages less than ~ 100 Myr. From Fig. 15, for Runs 3 and 4, we saw that the amount of mass lost during the early period of rapid stellar evolution also influences to some extent the degree of the observed core expansion. However, all four models in the present case were specifically designed to possess identical populations of massive stars and retained BHs, and all therefore lose essentially identical amounts of mass due to stellar evolution at early times. The variation in the core expansion observed during this phase in Fig. 21 therefore cannot be caused by differing amounts of mass-loss and must solely be a result of the different initial cluster structures. More centrally concentrated mass-loss, in a more tightly-bound cluster core, clearly leads to a greater degree of core expansion during the early period of a cluster's life.

After the first stage of core expansion is complete in the four model clusters, their core radii remain roughly constant until the BH populations have accumulated at the cluster centres and started to form BH binaries, after which point the second phase of core expansion begins. From Fig. 21, the rates of observed expansion in this second phase are

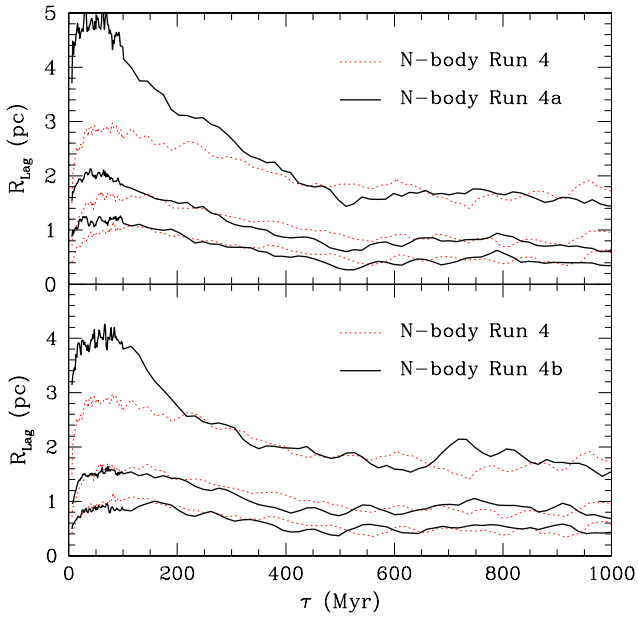

Figure 22. Evolution of the 10%, 25% and 50% BH Lagrangian radii in Runs 4a (upper panel, solid lines) and 4b (lower panel, solid lines). The evolution of the same radii in Run 4 are plotted for comparison in both panels (dotted lines). The BH subsystems in Run 4a and 4b both expand at early times in response to the rapid mass-loss from stellar evolution which is occurring, although the expansion is greater in the more heavily mass segregated Run 4b. Once the early mass-loss phase is mostly complete ($\tau \approx 100$ Myr), the evolution of the BH subsystems are very similar to that in Run 4 (and Run 2 – cf. Fig. 18).

approximately equivalent in all four clusters, so that the tracks on the radius-age plane run close to parallel for the remainder of the simulations.

Fig. 21 shows that the second stage of core expansion begins at an approximately equivalent time in each of the four models. We already noted this fact for Runs 2 and 4 in Section 4.2 and concluded that in a primordially mass segregated cluster the BH population does not become dynamically active significantly earlier than in a non-segregated cluster, because the strong expansion experienced by the mass segregated cluster at early times affects the BH population sufficiently strongly to negate the natural tendency of the BHs to sink to the cluster centre. In Fig. 22 we plot the evolution of the BH Lagrangian radii in Runs 4a and 4b, with those for Run 4 plotted for comparison. It is clear from this plot that even though the BHs tend to form closer to the cluster centres in more primordially mass segregated models, these models also suffer greater degrees of early expansion, hence delaying the central accumulation of BHs. This results in very similar evolution of the BH Lagrangian radii in Runs 2, 4, 4a, and 4b after the early rapid stellar evolution phase is complete, and leads to the formation of the first BH binaries at very similar ages – 510 Myr, 570 Myr, 540 Myr, and 460 Myr, in the four models respectively. Given that this is by nature a stochastic process, the agreement between these times for four models with such a wide range of early structural evolution is quite close. This observation strengthens our earlier conclusion that primordial mass segregation in a cluster does not lead to the earlier development of a dynamically active BH subsystem compared to a cluster which is not primordially mass segregated.

4.4 Run 5: Intermediate BH retention

Together with Runs 4a and 4b, we computed one additional model possessing properties intermediate between those of our four primary Runs. In this case, instead of intermediate degrees of primordial mass segregation, we set up the simulation (labelled Run 5) so that $f_{\rm BH} \approx 0.5$. Its initial conditions were otherwise identical to to those in Runs 3 and 4 (i.e., strong primordial mass segregation set by $T_{\rm MS} = 450$ Myr). One aim of Run 5 is to check that, as should be expected, its core radius evolution lies between that observed for Run 3 (where $f_{\rm BH} = 0$) and that observed for Run 4 (where $f_{\rm BH} = 1$). More importantly however, this model explores whether the extreme case that $f_{\rm BH} \approx 1$ is *necessary* for significant core expansion to occur, or if such expansion can still develop in a system which loses a large fraction of its BHs at formation. We set the duration of Run 5 to be roughly a Hubble time ($\tau_{\rm max} = 10.06$ Gyr) so that we could observe the full long-term core evolution of this model.

To generate a retention fraction of roughly 50 per cent in Run 5, we examined the formation of BHs in Run 4 with the aim of determining a suitable distribution of natal kicks. More specifically, we calculated the potential energy ($U_{\rm BH}$) of each given BH at the moment of its formation in Run 4, and estimated the escape velocity $v_{\rm esc} = \sqrt{-2U_{\rm BH} \,/\, m_{\rm BH}}$. Under the assumption that the inherited kinetic energy of the BH at formation ($K_{\rm BH}$) does not contribute to its ejection, this escape velocity corresponds to the minimum natal kick required to remove the BH from the cluster. However, this assumption is not always justified – for example, the natal kick may be in the same direction as the inherited motion of the BH, in which case the minimum required velocity would be significantly smaller than the original estimate, and closer to $v_{\rm esc} = \sqrt{-2(U_{\rm BH} + K_{\rm BH}) \,/\, m_{\rm BH}}$.

The two calculated distributions of BH escape velocities in Run 4 may be seen in Fig. 23. The upper left panel is the binned distribution neglecting the inherited kinetic energy of the BH, while the upper right panel is the binned distribution under the assumption that the kick velocity is in the same direction as the inherited velocity. The lower panel shows the two distributions in cumulative form. The most tightly bound BHs require natal kicks of order ≈ 12 km s^{-1} to escape the cluster, while the least tightly bound BHs require only tiny natal kicks to escape. Note from the upper right panel that two BHs are unbound from the cluster at their formation – this is a result of their progenitor stars becoming unbound shortly before exploding as supernovae, because of the recent rapid mass-loss occurring in the progenitor star as well as the violent fluctuations occurring in the cluster potential due to mass-loss from other stars.

For interest's sake, we also calculated the same distributions for Run 2, which, in contrast to Run 4, was not primordially mass segregated. The distributions for this model are plotted in the lower panel of Fig. 23 as dashed lines. As might be expected, BHs formed in the mass segregated Run 4 are significantly more tightly bound than are BHs formed in the non-segregated Run 2. Hence, the initial structure of

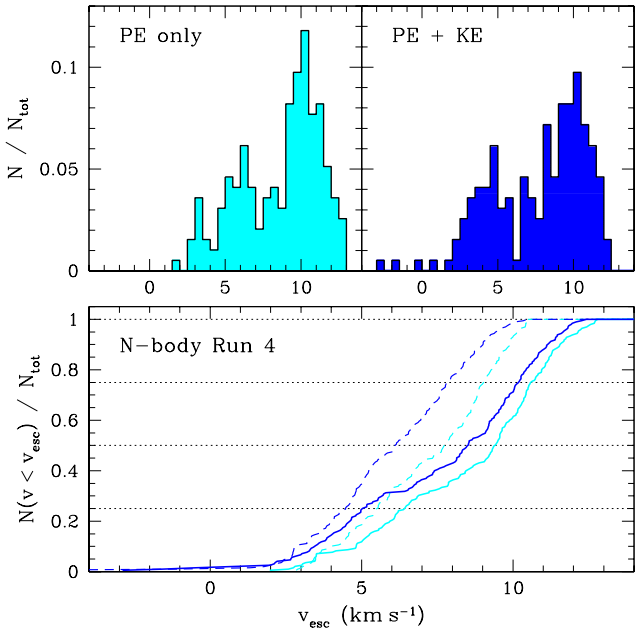

Figure 23. Calculated distributions of escape velocities at formation for all 198 BHs in Run 4. The upper left panel is the binned distribution assuming $v_{\rm esc} = \sqrt{-2U_{\rm BH}\,/\,m_{\rm BH}}$, while the upper right panel is the binned distribution if the inherited kinetic energy is also included so that $v_{\rm esc} = \sqrt{-2(U_{\rm BH}+K_{\rm BH})\,/\,m_{\rm BH}}$. The distributions may be interpreted as the minimum natal kicks required to remove the respective BHs from Run 4 under the two different assumptions listed above. The lower panel shows the two distributions in cumulative form (solid lines, where the distribution including $K_{\rm BH}$ is to the left of that where $K_{\rm BH}$ is neglected). Also marked are the equivalent distributions for Run 2, which has no primordial mass segregation (dashed lines).

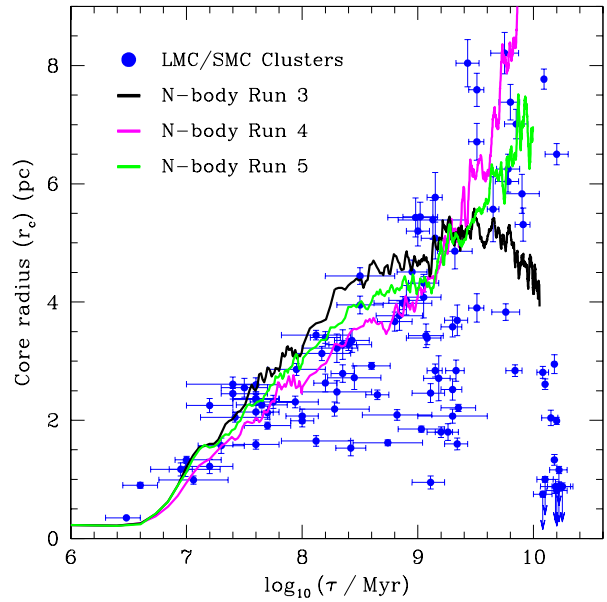

Figure 24. Core radius evolution of N-body Run 5, with the evolution of Runs 3 and 4 plotted for comparison. All three models possess identical initial conditions, including strong primordial mass segregation ($T_{\rm MS} = 450$ Myr) and the formation of 198 BHs. The only difference between them is the BH retention fraction, which is zero for Run 3, unity for Run 4, and approximately 0.485 for Run 5 – i.e., in Run 5 96 BHs are still present after 100 Myr.

a cluster can have some effect on the retention fraction of BHs. We discuss this issue in more detail in Section 5.

The distributions observed for Run 4 in Fig. 23 allowed us to determine a suitable distribution of natal kicks in Run 5 in order to set $f_{\rm BH} \approx 0.5$. We did this by noting that the retention fraction $f_{\rm BH}$ is approximately the mean probability of retention calculated over the full BH subsystem – that is, $f_{\rm BH} \approx \sum P_i(retain)\,/\,N_{\rm BH}$ where $N_{\rm BH}$ is the number of BHs in the subsystem and $P_i(retain)$ is the probability that the i-th BH will not be ejected by the natal kick it receives at formation. For simplicity, we set the natal kicks in Run 5 to be selected randomly from a uniform distribution spread between $v_{\rm kick} = 0$ km s^{-1} and $v_{\rm kick} = v_{\rm k,max}$ km s^{-1}. In this case, for the i-th BH at formation the retention probability is given by $P_i(retain) = P(v_{\rm kick,i} < v_{\rm esc,i}) = v_{\rm esc,i}\,/\,v_{\rm k,max}$ if $v_{\rm k,max} > v_{\rm esc,i}$, or unity otherwise. Assuming that $v_{\rm k,max}$ is larger than $v_{\rm esc,i}$ for all BHs in the subsystem under consideration, in order to obtain a given retention fraction we require $v_{\rm k,max} = \sum v_{\rm esc,i}\,/\,(f_{\rm BH}N_{\rm BH})$. For Run 5 we have that $N_{\rm BH} = 198$, and require that $f_{\rm BH} = 0.5$, and we compute the sum using the distributions displayed in Fig. 23. We found that in this scenario $v_{\rm k,max} = 17.5$ km s^{-1}, determined by adopting the mean of the results for the two measured distributions (i.e., with and without the inherited BH kinetic energy). No physical meaning should be read into our choice of a uniform kick distribution – we selected it here simply for convenience. The above process could easily be generalized to any desired probability distribution.

With the natal kick distribution described above implemented in Run 5, as expected we observed a significant number of BHs escaping from the cluster shortly after their formation. All 198 BHs in the simulation are created by $\tau = 10$ Myr, and the first BH escapes occur at $\tau = 14$ Myr. By $\tau = 100$ Myr, 102 BHs have left the cluster, and the escape rate has dropped to approximately one BH every 100 Myr. Subsequently, BHs appear to be leaving the cluster due to straightforward relaxation and evaporation processes – by the time of the creation of the first stable BH binary at $\tau \approx 1350$ Myr, a further 9 BHs have been removed. Hence, we estimate the BH retention fraction in this realization of Run 5 to be $f_{\rm BH} = 0.485$, but it could be as low as $f_{\rm BH} = 0.440$ depending on whether BHs escaping between $\tau \approx 100 - 1350$ Myr are included in the definition. We note that re-running this simulation with a new random seed would result in a different retention fraction, since, in contrast to all our previous models, the ejection of BHs due to natal kicks is a stochastic process in Run 5.

The evolution of Run 5 on the radius-age plane is plotted in Fig. 24, along with the evolution of Runs 3 and 4 for comparison. All three models possess identical initial conditions – the only difference between them is the BH retention fraction. At all times, the core radius of Run 5 lies in between those measured for Runs 3 and 4. During the first, early, phase of core expansion, this is a consequence of the intermediate BH retention fraction in Run 5 – this model loses less mass than Run 3 but more than Run 4. The second phase of core expansion, due to BH activity, begins at $\tau \approx 1400$ Myr in Run 5. This is noticeably later than in

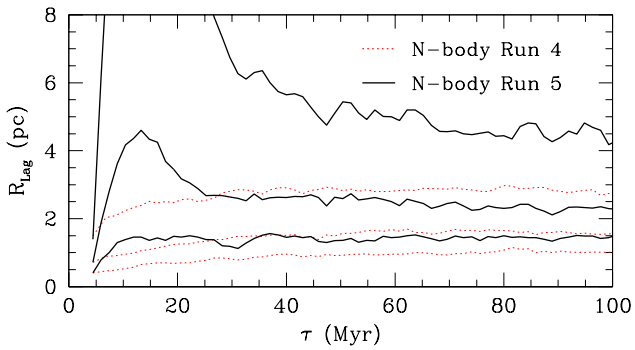

Figure 25. Early evolution of the 10%, 25% and 50% BH Lagrangian radii in Run 5 (solid lines). The evolution of the same radii in Run 4 are plotted for comparison (dotted lines). The BH subsystem in Run 5 expands significantly at early times primarily due to the non-zero natal kicks, although the BHs do also share in the general expansion of the cluster due to the rapid mass-loss from stellar evolution which is occurring during this period.

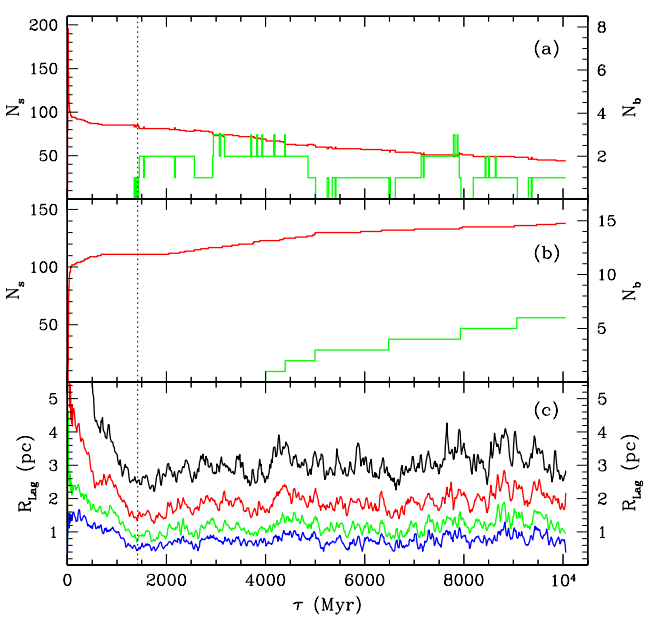

Figure 26. Properties of the BH population in Run 5 as a function of time: (a) the number of single BHs (upper line) and binary BHs (lower line) in the cluster; (b) the cumulative numbers of escaped single BHs (upper line) and binary BHs (lower line); and (c) the *black hole* 10%, 25%, 50% and 75% Lagrangian radii (respectively, the innermost to outermost lines). The vertical dotted line indicates $\tau = 1400$ Myr, the approximate time when core expansion due to BH activity begins. Note the different axis scales on either side of panels (a) and (b).

the previous models; furthermore, the rate of expansion is clearly not as great as is observed in Run 4 where twice as many BHs are retained.

The evolution of the BH population in Run 5 is illustrated in Figs. 25 and 26. The first of these shows the very early evolution of the 10%, 25% and 50% BH Lagrangian radii, compared to Run 4. Upon formation of the BHs, the BH Lagrangian radii are initially identical in Runs 4 and 5 because they share identical initial conditions and random seeds. However, the Lagrangian radii in Run 5 immediately undergo a large degree of expansion. This is primarily in response to the non-zero natal kicks given to the BHs, although the BH subsystem does share in the general expansion of the cluster which is occurring during this period due to the rapid mass-loss from stellar evolution. For comparison, the Run 4 Lagrangian radii are expanding only in response to this mass-loss. The Lagrangian radii in Run 5 exhibit large bumps at early times – these are most prominent in the 25% radius at $\tau < 30$ Myr and the 50% radius at $\tau < 50$ Myr. These features are due to the large number of BHs moving outward in the cluster on their way to escaping. The majority of these BHs have been removed from the cluster by ~ 50 Myr. After this point, the Lagrangian radii are still greatly inflated compared to those for Run 4. This is due to the extra kinetic energy received by the retained BHs in Run 5 at their creation.

Fig. 26 shows the long-term evolution of the BH subsystem in Run 5. Because of the extra kinetic energy the retained BHs in this model receive at birth, they take significantly longer to sink to the cluster centre via dynamical friction than do the BHs in previous models. In addition, there are fewer BHs retained in Run 5, so once they have accumulated in the cluster core, they interact more infrequently than in previous comparable models such as Run 4. The first BH binary does not form in Run 5 until $\tau = 1350$ Myr, much later than in our previous models. Binary hardening, BH scattering and BH ejection subsequently begin; however, the rates of all these processes are considerably reduced compared to previous simulations. The first ejection of a single BH after the formation of the first BH binary does not occur until $\tau = 2050$ Myr, while the first ejection of a BH binary does not occur until $\tau = 4000$ Myr.

By the end of Run 5, at $\tau_{\rm max} = 10.06$ Gyr, only six BH binaries have been ejected. In common with earlier models, a significant population of BHs still remains in Run 5 at this point, consisting of 44 single BHs and one BH binary. The ejected BH binaries possess properties very similar to those observed for Run 4. Two have eccentricities in the range $0.8 < e < 0.95$ while the remaining four have $e < 0.8$. The closest ejected BH binary has separation $a_b = 7.55$ AU, while the least tightly bound has $a_b = 61.0$ AU. The mean mass of individual BHs in the ejected binaries is again greater than the ensemble average, at $10.65\,{\rm M}_\odot$.

The reduced activity of the central BH subsystem in Run 5 compared with our other models explains the somewhat slower expansion of the core radius in this simulation. Despite this, the evolution of $r_c/r_{h,l}$ is very similar to earlier models with retained BH populations. Once the late, prolonged phase of core expansion begins in Run 5 (i.e., after $\tau \approx 1400$ Myr), the locus traced by $r_c/r_{h,l}$ lies exactly on top of that for Run 4, reaching $r_c/r_{h,l} \sim 0.8$ by the end of the simulation. This indicates that despite the reduced heating rate due to the BH population (and hence slower expansion of r_c), the distribution of this heating within the cluster is similar to that for Runs with larger numbers of BHs. Overall, Run 5 clearly demonstrates that complete BH retention is not necessary for significant and prolonged core expansion to occur – even with half the number of retained BHs as Run 4, Run 5 still reaches the upper right-hand corner of the radius-age plane after ~ 10 Gyr of evolution.

4.5 Run 6: Can neutron stars replace BHs?

Finally, we computed one further model, designed to investigate whether the influence of a population of BHs is necessary for prolonged core expansion to develop in a cluster, or whether such expansion can also result from similar dynamical processes involving larger numbers of less massive stellar remnants such as neutron stars (NSs). To this end we set up the new simulation, named Run 6, so that it was initially identical to Run 1 – that is, possessing no primordial mass segregation and retaining no BHs. However, unlike Run 1 where NSs were formed with large kicks so that the NS retention fraction $f_{\rm NS} = 0$, in Run 6 we set the natal NS kicks to be zero in order to achieve the extreme case that $f_{\rm NS} = 1$. In all, 425 NSs are formed in Run 6 from supernova explosions occurring between $\tau \approx 10 - 43$ Myr. The masses of these NSs lie in the range $1.30 \leqslant m_{\rm NS} \leqslant 2.32\,{\rm M}_{\odot}$. We extended the duration of Run 6 to be as long as that for Run 1 (i.e., $\tau_{\rm max} \approx 20$ Gyr), to enable a comparison between the full long-term development of the two models.

The evolution of Run 6 on the radius-age plane may be seen in Fig. 27. Clearly, the retention of a large number of NSs in this model does not result in core expansion at any stage during the lifetime of the cluster. In fact, the evolution is remarkably similar to that of Run 1, with the cluster undergoing many Gyr of gradual contraction before entering the core collapse phase. By the end of the early rapid mass-loss period at roughly $\tau \sim 100$ Myr, the median relaxation time in Run 6 is very similar to that in Run 1 at the same age – i.e., $t_{rh} \sim 2$ Gyr. In the absence of any retained BHs, the NSs are the most massive objects in the system and hence begin to sink to the cluster centre on a time-scale of $\sim (m_*/m_{\rm NS})\,t_{rh} \approx 500$ Myr. However, the NSs are not very many times more massive than the otherwise most massive stars in the cluster, and so the central density of NSs never exceeds that of the other cluster members by a sufficient degree that the NS subsystem is unstable to a runaway collapse (Spitzer 1987, Eq. 3-55). Hence, the NS subsystem evolves quite differently to the BH subsystems in our previous models, which did become unstable to runaway collapse. No NS binaries are formed in the central core, and consequently, widespread scattering and ejection of NSs does not occur. As a result, Run 6 proceeds towards core collapse rather than undergoing prolonged core expansion.

From Fig. 27 it is evident that Run 6 enters the core collapse phase at a significantly earlier time than does Run 1 – observationally, the point of deepest collapse (smallest core radius) occurs at $\tau \approx 12.8$ Gyr in Run 6, compared with $\tau \approx 17.4$ Gyr in Run 1. At any given age, the median relaxation time in Run 6 is very similar to that in Run 1, so that the point of deepest collapse in Run 6 occurs after significantly fewer integrated median relaxation times than in Run 1 – $4.40\,t_{rh}$ as opposed to $8.37\,t_{rh}$. More enlightening is to examine the relaxation time in the central core of each cluster, $t_{r0} \propto v_s r_c^2 m_{*0}^{-1}$, where v_s is the velocity scale in the core and m_{*0} is the mean mass of all the particles in thermal equilibrium in the central parts (e.g., Meylan 1987). Calculating for each model the integrated number of central relaxation times which have elapsed by the time the point of deepest collapse occurs, the two values are within ~ 10 per cent of each other. The central relaxation time in Run 6 is generally much shorter than in Run 1, due to the larger mean mass of the centralmost objects (predominantly NSs).

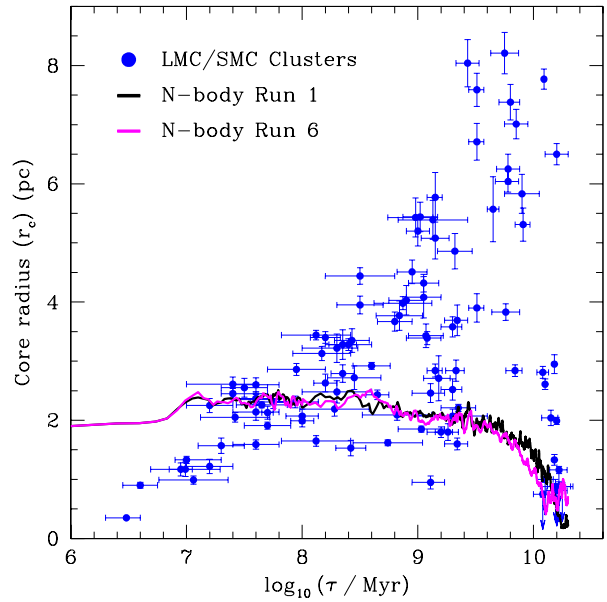

Figure 27. Core radius evolution of N-body Run 6, with the evolution of Run 1 plotted for comparison. These two models possess identical initial conditions – neither has any primordial mass segregation, and $f_{\rm BH} = 0$ in both. The only difference between them is that in Run 6 neutron stars are formed with no natal kicks so that $f_{\rm NS} = 1$, whereas in Run 1 they are formed with large natal kicks so that $f_{\rm NS} = 0$. Hence, Run 6 retains 425 neutron stars, which are not present in Run 1. Unlike a BH population, the NS population in Run 6 does not lead to core expansion, but does cause the cluster to enter the core collapse phase at an earlier age.

It is also evident from Fig. 27 that during collapse, the smallest observed core radius in Run 6 is larger than the smallest observed core radius in Run 1. This is due to the luminosity cut-offs inherent in the calculation of r_c. In Run 1, the stars contributing most of the light for the calculation of r_c are also among the most massive remaining members, and hence typically reside in the innermost cluster regions during the core collapse phase. In Run 6 however, the centralmost members are the NSs, which do not contribute light for the calculation of r_c. The most luminous stars in Run 6 therefore appear to constitute a more widely distributed "core" during the late phases of evolution than do those in Run 1. The larger core radius during collapse in Run 6 is also reflected in the evolution of $r_c/r_{h,l}$ for this model. While the behaviour of this ratio is very similar to that for Run 1, during collapse $r_c/r_{h,l}$ oscillates around ~ 0.2 rather than the smaller values ($r_c/r_{h,l} \lesssim 0.05$) observed for Run 1.

Just as in Run 1, the point of deepest collapse in Run 6 coincides with a spate of binary formation in the core. This time, the binaries generally possess at least one NS member; several of them are NS-NS binaries. These are the first binary objects involving NSs to be created in Run 6 – no such objects are formed at earlier times in this model.

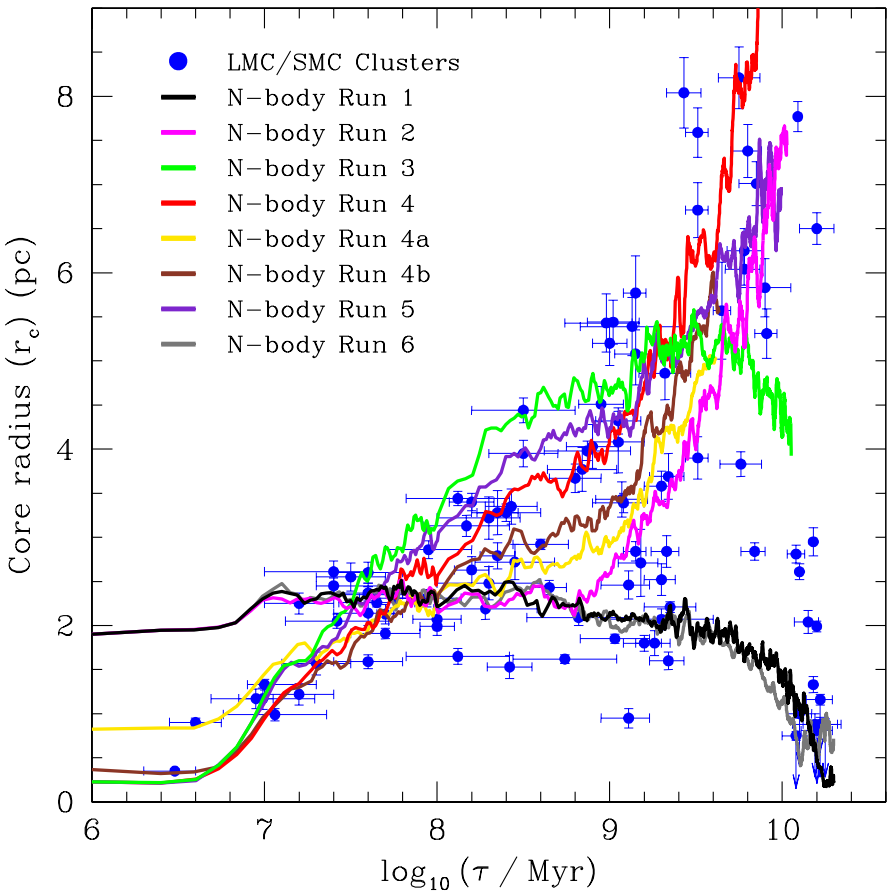

Figure 28. Our full suite of eight N-body Runs plotted together for comparative purposes. In combination, the two core expansion processes described in this paper lead to a wide variety of evolutionary paths on the r_c versus age plane, which fully cover the observed distribution of massive Magellanic Cloud star clusters.

5 DISCUSSION AND SUMMARY

In this paper we have presented an ensemble of eight large-scale N-body simulations aimed at directly modelling the evolution of massive star clusters like those observed in the Magellanic Clouds. Figure 28 shows the core radius evolution of all eight models plotted on the same set of axes, for the purposes of direct comparison. Using these models we have identified two physical processes which can occur in such clusters and result in substantial core expansion – mass-loss due to rapid stellar evolution in a cluster which is mass-segregated or otherwise centrally concentrated, and heating due to a significant population of retained stellar-mass ($\sim 10\,\mathrm{M}_\odot$) BHs formed in the supernova explosions of the most massive cluster stars. These two processes operate over different time-scales and at different stages in a cluster's life. The former only occurs during the first $\sim 100-200$ Myr after the formation of a cluster, when massive stars are still present. These evolve rapidly, losing a large fraction of their mass as they do so. The latter begins, at the earliest, several hundred Myr after the formation of the cluster but may remain active for at least a Hubble time beyond this starting point. In combination, these two processes can lead to a wide variety of evolutionary paths on the core-radius versus age plane, which fully cover the observed distribution of massive star clusters. They therefore define a physically-motivated dynamical explanation for the radius-age trend observed for the star cluster systems belonging to the Magellanic Clouds.

Our N-body modelling has allowed us to examine in more detail the behaviour of each of these core-expansion mechanisms. As stated above, the phase of severe mass-loss due to rapid stellar evolution is mostly complete by $\sim 100-200$ Myr into a cluster's life, by which time all the most massive stars in the cluster have expired. Mass-loss due to stellar evolution still occurs after this point; however, it is from much less massive stars and therefore proceeds at a far more gradual rate without noticeably affecting the core radius evolution of the host cluster. Our simulations show that the amount of observed core expansion in a cluster due to the early mass-loss phase depends on both the degree of primordial mass segregation in the cluster, and the amount of mass lost in relation to the total cluster mass. In models where the former parameter is held constant and the latter parameter is varied (e.g., Runs 3, 4, and 5), the cluster losing the most mass expands the fastest. In models where the latter parameter is held constant and the former parameter is varied (e.g., Runs 2, 4, 4a, and 4b), the cluster with the most significant degree of primordial mass segregation expands the fastest. Furthermore, the early rapid phase of mass-loss does not cause any significant core expansion in

our models unless the mass-loss is centrally concentrated – models which do not possess any primordial mass segregation exhibit essentially no early expansion. In models where early expansion occurs, the ratio of the core radius to half-light radius $r_c/r_{h,l}$ increases significantly. This is in contrast to models which do not undergo early expansion, where $r_c/r_{h,l}$ remains fairly constant with time. Inflated values of $r_c/r_{h,l}$ may remain for $\gtrsim 10$ Gyr in some clusters (cf. Run 3), since the central and median relaxation times in these objects become rather long.

Since the amount of mass lost in the early rapid stellar evolution phase is an important contributor to the amount a cluster core expands during this phase, the expansion is effectively regulated by the cluster's stellar IMF, modulated by second order effects such as BH retention. A steep IMF results in proportionally few high-mass members and hence a small amount of early expansion, whereas a flat IMF results in proportionally many high-mass members and hence a large amount of early expansion. In principle, therefore, significant inter-cluster IMF variations could lead to a variety of dramatically different paths across the radius-age plane at ages $\tau \lesssim 200$ Myr, and consequently induce a large spread in the observed cluster distribution (e.g., Elson et al. 1989). However, there is an increasing body of evidence that large-scale variations in the stellar IMF between Magellanic Cloud clusters are not present (e.g., Kroupa 2001; de Grijs et al. 2002c). This in turn suggests that inter-cluster variations in the degree of primordial mass segregation or central concentration may be the primary driver of the observed spread in the radius-age distribution at young ages. The sharp upper envelope of the distribution at ages less than a few hundred Myr therefore most likely reflects an upper limit to the degree of primordial mass segregation present in Magellanic Cloud clusters. Indeed, our model with an IMF matching that generally observed for Magellanic Cloud clusters (Kroupa 2001), and an initial structure (including mass segregation) matching that observed for R136 (which is the most extreme young object presently observed in the Magellanic Clouds) evolves along a path closely matching the upper envelope of the radius-age distribution at early times.

One important process which can affect the early evolution of a massive star cluster, but which is not included in our N-body models, is the expulsion of gas left over from the star formation process. This residual gas is removed from the cluster within the first ~ 10 Myr due to the combined effect of massive stellar winds and supernova explosions. Just as with the early mass-loss due to stellar evolution, mass-loss due to gas expulsion can cause cluster core expansion, although typically on an even shorter time-scale of $\approx 10-20$ Myr (e.g., Bastian & Goodwin 2006; Goodwin & Bastian 2006). The larger the mass of expelled gas, the larger the degree of core expansion; if the mass of expelled gas is too great, the cluster may become unbound. In cases where the star formation efficiency is relatively high, and in the absence of sustained mass-loss due to stellar evolution, clusters soon settle into new equilibrium states with core radii generally not much larger than their initial values (see Goodwin & Bastian 2006, Fig. 2). Therefore, gas expulsion may be affecting the core radius evolution of clusters younger than ~ 50 Myr in our radius-age plot, but is unlikely to be of relevance to cluster evolution on longer time-scales. To correctly model the effects of gas loss occurring in combination with early stellar mass loss on the evolution of the various types of clusters studied in the present work will require more sophisticated codes than are presently available.

Core expansion due to the dynamical influence of a population of retained stellar-mass BHs in a cluster occurs over a much longer timescale than that due to early mass loss. Our simulations show that the BH population in a cluster only induces core expansion once the BHs have accumulated in a sufficiently dense central subsystem that BH binaries are created. These binaries are the catalyst for core expansion, since it is the interactions between them and other single and binary BHs which lead to BH scattering and ejection, and subsequent heating of the central cluster regions. We do not observe core expansion due to the BH population prior to the formation of BH binaries in any of our simulations. In particular, the sinking and accumulation of BHs in the core does not appear to affect the observed core radius.

In our models, the time at which the first BH binaries are formed is relatively independent of the early evolution of the cluster. Models which are identical but for widely varying degrees of primordial mass segregation and hence widely varying amounts of early expansion (Runs 2, 4, 4a, and 4b) all form their first BH binaries at ages of roughly $\sim 500-600$ Myr. Even though BHs are preferentially formed very centrally in a model with a significant degree of primordial mass segregation compared to a model with no primordial mass segregation, the former object undergoes very significant early expansion compared to the latter. The BH subsystem does not escape this expansion, and by $\tau \sim 200$ Myr it has roughly the same distribution within the cluster as does the BH subsystem in the initially non-segregated model. The subsequent evolution of the two BH populations is very similar. The time of formation of the first BH binaries is, however, strongly sensitive to the natal kicks received by the BHs at formation. In the case of non-zero kicks, retained BHs take longer to accumulate in the cluster centre than in the case of no kicks, due to the extra kinetic energy they receive at birth. In addition, non-zero natal kicks generally result in the expulsion of some fraction of the BH population, leading to a smaller retained BH subsystem and a smaller probability per unit time of BH binary formation. Although our modelling did not test it, the time of formation of the first BH binaries is also expected to be sensitive to the mean BH mass. More massive BHs will sink to the cluster centre much more rapidly than less massive BHs, and hence form a dense central core at a significantly earlier time.

Once BH binaries have formed in a cluster and core expansion begins, the rate of expansion is dependent on the number of BHs in the cluster. A cluster with fewer BHs expands more slowly than an otherwise identical cluster with more BHs (cf. Runs 4 and 5). This is because the interaction rate between BHs in the cluster centre is much lower for the model with the smaller number of BHs, so that fewer BHs are scattered and ejected per unit time and the rate of heating of the cluster is reduced. The interaction rate between BHs in the cluster centre is also apparently sensitive to the density of the surrounding stellar core – it is significantly reduced in lower density clusters (cf. Runs 2 and 4). These observations have important implications for the survivability of BH subsystems within clusters. As the number of BHs in a cluster decreases due to the ejection of BHs after close encounters, and the central density of the cluster decreases

due to the expansion of its core, the interaction rate between BHs in the cluster centre also decreases. This in turn results in a lower BH ejection rate, allowing the BH population in a cluster to survive much longer than previously believed. All our long-duration simulations with retained BHs still possess a sizeable BH population after a Hubble time of evolution. As a result, some degree of core expansion is still occurring in these models at late times.

We emphasize that even though most of our models examine the scenario where *all* BHs are retained in a cluster, such an extreme case is not *required* for core expansion to occur. We still observe significant expansion in the more moderate case of ~ 50 per cent retention, although the rate of expansion is reduced due to the factors outlined above.

It is also worth emphasising that while rapid mass-loss due to stellar evolution is the dominant cluster core expansion process at early times ($\tau \lesssim 200$ Myr), that expansion ceases as the mass-loss rate slows. This process therefore *cannot* drive the full observed radius-age distribution, which still exhibits a significantly increasing spread in core size at much later times. A cluster which has expanded during its first few hundred Myr of evolution, but which has not retained a BH population sufficient to induce additional late-time expansion, begins to contract again as two-body relaxation processes take over (Run 3). Our models *only* achieve core sizes matching those observed for the most extended ~ 10 Gyr old Magellanic Cloud clusters if expansion due to a retained BH population also occurs. This long-term expansion cannot be reproduced by other types of stellar remnants such as neutron stars (Run 6). Such remnants are not of high enough mass to accumulate in a central subsystem of sufficient density to allow frequent formation of the binary objects which drive the cluster heating.

The ratio $r_c/r_{h,l}$ evolves very similarly in all of our models where core expansion due to a retained population of BHs occurs, once this phase has started. By $\tau \sim 10$ Gyr, the ratio approaches a large value of $r_c/r_{h,l} \approx 0.8$, comparable to the largest values observed for old Magellanic Cloud clusters, and Galactic globular clusters. This is irrespective of the early evolution of a cluster (i.e., whether expansion due to early mass-loss occurs or not), the time of onset of the expansion due to BHs, and the subsequent rate of this expansion. As described in Section 4, these observations are compatible with those presented recently by Hurley (2007).

Several other mechanisms are known to be able to sustain large or expanding cores in massive clusters. For example, the presence of primordial binary stars may stall core collapse, while the presence of a central IMBH may result in cluster expansion (Baumgardt et al. 2004a,b). The heating effect of stellar-mass BHs, as considered in this paper, is far more efficient than the heating effect due to primordial binaries in comparable clusters. To transfer binding energy from primordial binaries to other cluster members requires frequent interactions and hence a dense environment. For most of their lives, Magellanic Cloud clusters are not sufficiently dense, as has been demonstrated from N-body modelling by Mackey (2003)[4]. Furthermore, heating due to primordial binaries is self-regulated: a dense core will expand, reducing the interaction rate and switching the heating off until the core contracts again. Primordial binaries therefore cannot sustain the type of core expansion observed in our N-body models. It is more difficult to estimate the relative heating efficiency of stellar mass BHs compared to that of a central IMBH. Baumgardt et al. (2004a,b) display the evolution of the Lagrangian radii of their large N-body models, which do show significant expansion. However, it is difficult to disentangle the amount of heating due to mass-loss from stellar evolution from the amount due to the central IMBH. Based on the material presented by Baumgardt et al. (2004a,b), we estimate that heating due to stellar-mass BHs is probably at least as efficient as that due to a central IMBH.

The scenario outlined above as a dynamical explanation for the radius-age trend observed in the Magellanic Clouds requires significant variations in BH population size (i.e., in the BH retention fraction) between otherwise very similar clusters. Clusters which have developed very large core radii by the time they are $\gtrsim 12$ Gyr old (e.g., the LMC clusters NGC 1841 and Reticulum) must have managed to retain a significant BH population. Conversely, clusters which have entered core collapse at late times (e.g., the LMC clusters NGC 2005 and 2019) are unlikely to have retained very many BHs – for example, Hurley (2007) showed that even one BH binary in a cluster can prevent the collapse of its core.

There are a number of possibilities which could lead to inter-cluster variability in the BH population size. First, we note that the number of BH-forming stars in a given cluster is only a tiny fraction of the total number of stars in the cluster, so there will always be sampling-noise variations between clusters. In addition, the formation of a BH in a supernova explosion is sensitive to many features of the prior evolution of the progenitor star, in particular how much mass it loses as it evolves. Factors which introduce mass-loss variations, such as binarity, chemical inhomogeneities or a dispersion in stellar rotation, are therefore likely to further accentuate the stochastic fluctuations in BH population size between clusters. In principle, inter-cluster variations in the stellar IMF would also strongly affect BH population sizes; however, as we noted earlier, such variations are not observed. Observations do suggest that the maximum stellar mass in a cluster correlates with the total cluster mass (e.g., Weidner & Kroupa 2006). Hence, even if the stellar IMF is universal between clusters, smaller clusters will have a lower maximum stellar mass and thus fewer BHs relative to the total cluster mass than will larger clusters.

Natal BH kicks are also critical. At present, these are poorly constrained both by theory and observation. Typical estimates lie in the range $0 \lesssim v_{\rm kick} \lesssim 200\ {\rm km\,s^{-1}}$, with kicks of a few tens of $\rm km\,s^{-1}$ possibly favoured (e.g., Willems et al. 2005, and references therein). If BH natal kicks are indeed typically a few tens of $\rm km\,s^{-1}$ in magnitude, then they are roughly comparable to the escape velocity of a massive stellar cluster. In this case, the structure of the host cluster when the BHs are formed (i.e., before $\tau \approx 10$ Myr) can strongly affect the retention fraction. For example, BHs formed in a dense, strongly mass segregated cluster are more easily retained that BHs formed in a comparably massive but less dense, non-segregated cluster (e.g., Fig. 23). The retention fraction will also be sensitive to the overall initial mass of the cluster, as well as to factors which affect the very early evolution of the cluster such as residual gas expulsion. Stellar binarity may also play an important role.

[4] This Ph.D. Thesis can be supplied by ADM on request.

It is interesting to note that theoretical models suggest BH formation to be a strongly sensitive function of metal abundance, in that BH production is apparently more frequent, and $m_{\rm BH}$ is typically greater for metal poor progenitor stars than for metal rich progenitor stars (see e.g., Zhang et al. 2007). Hence, the BH populations formed in clusters of very different metallicities are likely to be quite distinct. The strong age-metallicity relationships observed in both the LMC and SMC mean that this factor probably cannot cause differences between the BH population sizes in compact and extended LMC or SMC clusters of a given age, since such objects will have approximately equal metallicities. However, the LMC and SMC age-metallicity relationships do suggest that any BH populations forming in present-day young Magellanic Cloud clusters are likely to be quite different to those which may have existed in Magellanic Cloud clusters that are now $\gtrsim 12$ Gyr old.

The possibility of large-scale and prolonged core expansion has important implications for the study of all massive star clusters, including the globular clusters in our Galaxy and others. Many such objects are at least an order of magnitude more massive than the models presented in this paper. Even so, we expect the physical processes which we have described will still operate in larger systems.

Neglecting any stochastic fluctuations between clusters, the number of BHs formed in a cluster is, to first order, dependent only on the stellar IMF and the minimum progenitor mass. We do not expect these to change with cluster mass, so with all other parameters held constant, the mass fraction of BHs should remain the same for clusters of increasing mass. Similarly, the mass fraction lost due to rapid stellar evolution early on in a cluster's life should also remain the same for clusters of increasing mass. Assuming that natal BH kicks are also not a function of cluster mass, the BH retention fraction should increase with increasing cluster mass, since it is more difficult to eject BHs from the deeper gravitational well of a more massive cluster. Overall, we therefore expect the relative size of retained BH populations should be larger for more massive clusters. Given the above, more massive clusters have at least the same potential for core expansion as do less massive clusters.

In terms of the dynamics of the expansion, the central densities of the model clusters we have studied in this paper are directly comparable to the central densities of more massive objects such as globular clusters. The central and median relaxation times in our models are also commensurate with those calculated for typical globular clusters. Given this, we expect similar dynamical processes to operate on similar time-scales in clusters larger than our present models, so that early mass-loss and BH heating will both still be effective at inducing core expansion. The main difference is that it becomes more difficult to eject BHs as the cluster mass increases. Therefore, the mean time a BH remains in a cluster will increase with the total mass. This will increase the potential of each BH to heat the cluster through additional scattering-sinking cycles, and will allow BH binaries to harden further than they would do in a less massive object. BH heating in more massive clusters is hence likely to be even more efficient than it is in less massive clusters.

We therefore predict that some degree of core expansion is possible in any massive stellar cluster due to the processes outlined in this paper, irrespective of the total mass of the cluster. In many aspects of star cluster research, this possibility is not usually considered. However, under a wide variety of circumstances, it could have an important effect on the problem under consideration. As a simple example, it is well known that diffuse extended clusters are far more susceptible to tidal disruption than are compact clusters. Prolonged core expansion in clusters could result in many more such diffuse extended objects in a given population than would otherwise be expected. This possibility is vital to incorporate into modelling where destruction rates are important, such as studies designed to investigate the evolution of the globular cluster mass function (e.g., Fall & Zhang 2001), the past and future dissolution of globular clusters in the Galactic system (e.g., Gnedin & Ostriker 1997), or whether the super star clusters observed in starburst galaxies will eventually evolve into objects resembling classical globular clusters (e.g., de Grijs & Parmentier 2007).

Another example involves the measurement of dynamical mass estimates for young massive clusters in external galaxies. Such measurements are sometimes used to infer the stellar IMF in such clusters. Bastian & Goodwin (2006) and Goodwin & Bastian (2006) have demonstrated that very young clusters ($\tau \lesssim 50$ Myr) may be out of virial equilibrium due to the rapid expulsion of residual gas, so that dynamical mass measurements assuming virial equilibrium may be in error. Our modelling has shown that significant core expansion due to stellar evolution occurs on a timescale close to ~ 100 Myr. Researchers should be aware of this additional possibility when evaluating the properties of young clusters in external galaxies, although we note that it is not yet clear to what extent any signal due to such expansion would manifest in integrated cluster spectra. This is an avenue worthy of further investigation.

As a final example, consider the cluster half-mass radius, r_h. This quantity is often assumed to be relatively stable for much of a cluster's life (cf. Fig. 6), and is hence sometimes used to infer information about cluster formation (e.g., van den Bergh & Mackey 2004). However, if a cluster undergoes prolonged core expansion, r_h is certainly *not* a stable quantity (Fig. 8). Caution should therefore be exercised in the use of this parameter.

The possibility of core expansion may also help explain the properties of some of the more exotic star clusters discovered in recent years – for example, the "faint fuzzies" uncovered in several lenticular galaxies (Brodie & Larsen 2002), the luminous extended clusters found in the halo of M31 (Huxor et al. 2005; Mackey et al. 2006), and the diffuse star clusters located in a number of Virgo early-type galaxies (Peng et al. 2006). All these newly-discovered clusters possess unusually extended structures compared to those of classical globular clusters. Core expansion, particularly the prolonged variety due to retained BHs, may offer a viable formation channel for these objects.

We conclude with a note on the possibility of testing observationally our prediction of retained populations of stellar-mass BHs in some massive star clusters. While these BHs cannot be observed directly, there are a number of means by which their presence might be inferred in a cluster. One possibility is that a BH in a close binary with an evolved star is likely to be an X-ray source, as the star overflows its Roche limit and transfers gas onto the BH. Such BH X-ray sources are known in the field (see

e.g., Casares 2006) and one is known in an extra-Galactic globular cluster (Maccarone et al. 2007; Zepf et al. 2007); however, none have been found in Galactic globular clusters (Verbunt & Lewin 2006). From our modelling, we know that clusters which do retain significant BH populations are, for most of their lives, objects in which the timescale for encounters between BHs and stars is very long (due to the low stellar density in the extended core), but the timescale for encounters between BHs is comparatively short. Hence the creation of long-lived BH-star binaries is rare – we did not observe any such objects in our simulations. It is therefore unsurprising that no BH X-ray sources are known in the Galactic globular cluster system, and only one is known in an external cluster.

The most promising means of inferring the presence of a BH population in a cluster is through the dynamical effect it causes on the stellar component of the cluster. As we demonstrated in Section 4.1, unlike in the case of an IMBH, a significant stellar density and velocity cusp does not develop about the compact central BH subsystem. None the less, the effect of the central concentration of unseen mass should be evident in the stellar motions – the velocity dispersion of the cluster should be larger than is to be expected solely from the observed luminous mass. Observations to test this will be difficult, primarily because the target clusters should be extended, diffuse objects with low velocity dispersions. In addition, many will have relatively few targets suitable for spectroscopic radial velocity measurements, such as luminous red giants. Even so, it may be possible to make sufficiently precise observations with presently available $8-10$ m-class facilities.

Finally, it seems likely that at least some BH binaries ejected from very massive clusters will merge on a timescale $\lesssim 12$ Gyr, and will therefore be sources of gravitational radiation detectable by interferometers such as LIGO, and in future, LISA. This possibility has previously been investigated in more detail by other authors (see e.g., Portegies Zwart & McMillan 2000). As described in Sections 4.1 and 4.2, the BH binaries ejected from our model clusters will not merge on a timescale $\lesssim 12$ Gyr; however several have orbital parameters not far from the required threshold. A subset of the BH binaries ejected from more massive clusters than those studied here would almost certainly have orbital parameters well within this threshold.

ACKNOWLEDGEMENTS

We thank Sverre Aarseth for the use of NBODY4, and for numerous valuable discussions and on-going assistance. We also thank Jarrod Hurley for providing code to calculate the absolute magnitudes of stars evolving in our simulated clusters. We are grateful to Pete Bunclark and Mick Bridgeland for providing technical support with the IoA GRAPE-6 board, and to the anonymous referee for a thorough report which helped to improve the paper. ADM is supported by a Marie Curie Excellence Grant from the European Commission under contract MCEXT-CT-2005-025869, and is grateful for support from a PPARC Postdoctoral Fellowship during which much of this work was completed. MIW acknowledges support from a Royal Society University Research Fellowship and, previously, from PPARC. MBD is a Royal Swedish Academy Research Fellow supported by a grant from the Knut and Alice Wallenberg Foundation. Some results in this paper are based on observations made with the NASA/ESA Hubble Space Telescope, obtained at the Space Telescope Science Institute, which is operated by the Association of Universities for Research in Astronomy, Inc., under NASA contract NAS 5-26555. These observations are associated with program #9891.

REFERENCES

Aarseth S. J., 1999, PASP, 111, 1333
Aarseth S. J., 2001, New Astron., 6, 277
Aarseth S. J., 2003, Gravitational *N*-body Simulations. Cambridge University Press, Cambridge
Aarseth S. J., Heggie D. C., 1998, MNRAS, 297, 794
Bastian N., Goodwin S. P., 2006, MNRAS, 369, L9
Baumgardt H., 2001, MNRAS, 325, 1323
Baumgardt H., Makino J., Ebisuzaki T., 2004a, ApJ, 613, 1133
Baumgardt H., Makino J., Ebisuzaki T., 2004b, ApJ, 613, 1143
Bergeron P., Wesemael F., Beauchamp A., 1995, PASP, 107, 1047
Bica E., Clariá J. J., Dottori H., Santos Jr. J. F. C., Piatti A., 1996, ApJS, 102, 57
Binney J., Tremaine S., 1987, Galactic Dynamics. Princeton University Press, Princeton
Bonnell I. A., Bate M. R., 2006, MNRAS, 370, 488
Brandl B., et al., 1996, ApJ, 466, 254
Brodie J. P., Larsen S. S., 2002, AJ, 124, 1410
Casares J., 2007, in Karas V., Matt G., eds., Proc. IAU Symp. 238, Black Holes: from stars to galaxies. Cambridge University Press, Cambridge, p. 3
Casertano S., Hut P., 1985, ApJ, 298, 80
De Angeli F., Piotto G., Cassisi S., Busso G., Recio-Blanco A., Salaris M., Aparicio A., Rosenberg A., 2005, AJ, 130, 116
de Grijs R., Parmentier G., 2007, ChJAA, 7, 155
de Grijs R., Johnson R. A., Gilmore G. F., Frayn C. M., 2002a, MNRAS, 331, 228
de Grijs R., Gilmore G. F., Johnson R. A., Mackey A. D., 2002b, MNRAS, 331, 245
de Grijs R., Gilmore G. F., Mackey A. D., Wilkinson M. I., Beaulieu S. F., Johnson R. A., Santiago B. X., 2002c, MNRAS, 337, 597
Dejonghe H., 1987, MNRAS, 224, 13
de Zeeuw T., 1985a, MNRAS, 216, 273
de Zeeuw T., 1985b, MNRAS, 216, 599
Elson R. A. W., 1991, ApJS, 76, 185
Elson R. A. W., 1992, MNRAS, 256, 515
Elson R. A. W., Fall S. M., Freeman K. C., 1987, ApJ, 323, 54
Elson R. A. W., Freeman K. C., Lauer T. R., 1989, ApJ, 347, L69
Elson R. A. W., Sigurdsson S., Davies M. B., Hurley J. R., Gilmore G. F., 1998, MNRAS, 300, 857
Fall S. M., Zhang Q., 2001, ApJ, 561, 751
Giersz M., Heggie D. C., 1994, MNRAS, 268, 257
Gnedin O. Y., Ostriker J. P., 1997, ApJ, 474, 223
Goodwin S. P., Bastian N., 2006, MNRAS, 373, 752

Harris W. E., 1996, AJ, 112, 1487
Heggie D. C., 1975, MNRAS, 173, 729
Heggie D. C., 2001, in Steves B. A., Maciejewski A. J., eds., The Restless Universe: Applications of Gravitational N-Body Dynamics to Planetary, Stellar and Galactic Systems. IOP Publishing, Bristol, p. 109
Heggie D. C., Mathieu R. D., 1986, in Hut P., McMillan S., eds., Lecture Notes in Physics Vol 267, The Use of Supercomputers in Stellar Dynamics. Springer-Verlag, Berlin, p. 233
Heggie D., Hut P., 2003, The Gravitational Million-Body Problem. Cambridge University Press, Cambridge
Heggie D. C., Trenti M., Hut P., 2006, MNRAS, 368, 677
Heggie D. C., Hut P., Mineshige S., Makino J., Baumgardt H., 2007, PASJ, 59, L11
Hilker M., 2006, A&A, 448, 171
Hunter D. A., Shaya E. J., Holtzman J. A., Light R. M., 1995, ApJ, 448, 179
Hunter D. A., O'Neil Jr. E. J., Lynds R., Shaya E. J., Groth E. J., Holtzman J. A., 1996, 459, L27
Hunter D. A., Elmegreen B. G., Dupuy T. J., Mortonson M., 2003, AJ, 126, 1836
Hurley J. R., 2007, MNRAS, 379, 93
Hurley J. R., Pols O. R., Tout C. A., 2000, MNRAS, 315 543
Hurley J. R., Tout C. A., Aarseth S. J., Pols O. R., 2001, MNRAS, 323, 630
Hurley J. R., Tout C. A., Pols O. R., 2002, MNRAS, 329, 897
Hurley J. R., Tout C. A., Aarseth S. J., Pols O. R., 2004, MNRAS, 355, 1207
Hurley J. R., Pols O. R., Aarseth S. J., Tout C. A., 2005, MNRAS, 363, 293
Huxor A., Tanvir N. R., Irwin M. J., Ibata R., Collett J. L., Ferguson A. M. N., Bridges T., Lewis G. F., 2005, MNRAS, 360, 1007
Kim S. S., Figer D. F., Kudritzki R. P., Najarro F., 2006, ApJ, 653, L113
King I. R., 1962, AJ, 67, 471
Krauss L. M., Chaboyer B., 2003, Science, 299, 65
Kroupa P., 2001, MNRAS, 322, 231
Kroupa P., Tout C. A., Gilmore G. F., 1993, MNRAS, 262, 545
Kulkarni S.R., Hut P., McMillan S., 1993, Nature, 364, 421
Kurucz R. L., 1992, in Barbuy B., Renzini A., eds., Proc. IAU Symp. 149, The Stellar Populations of Galaxies. Kluwer, Dordrecht, p. 225
Maccarone T. J., Kundu A., Zepf S. E., Rhode K. L., 2007, Nature, 445, 183
Mackey A. D., 2003, Ph.D. Thesis, University of Cambridge
Mackey A. D., Gilmore G. F., 2003a, MNRAS, 338, 85
Mackey A. D., Gilmore G. F., 2003b, MNRAS, 338, 120
Mackey A. D., Gilmore G. F., 2003c, MNRAS, 340, 175
Mackey A. D., Gilmore G. F., 2004, MNRAS, 352, 15
Mackey A. D., van den Bergh S., 2005, MNRAS, 360, 631
Mackey A. D., Payne M. J., Gilmore G. F., 2006, MNRAS, 369, 921
Mackey A. D., et al., 2006, ApJ, 653, L105
Mackey A. D., Wilkinson M. I., Davies M. B., Gilmore G. F., 2007, MNRAS, 379, L40
Makino J., 1991, ApJ, 369, 200
Makino J., Fukushige T., Koga M., Namura K., 2003, PASJ, 55 ,1163
Malumuth E. M., Heap S. R., 1994, AJ, 107, 1054
Mateo M., 1987, ApJ, 323, L41
McLaughlin D. E., van der Marel R. P., 2005, ApJS, 161, 304
Massey P., Hunter D. A., 1998, ApJ, 493, 180
Massey P., Bresolin F., Kudritzki R. P., Puls J., Pauldrach A. W. A., 2004, ApJ, 608, 1001
Massey P., Puls J., Pauldrach A. W. A., Bresolin F., Kudritzki R. P., Simon T., 2005, ApJ, 627, 477
Merritt D., Cruz F., 2001, ApJ, 551, L41
Merritt D., Piatek S., Portegies Zwart S., Hemsendorf M., 2004, ApJ, 608, L25
Meylan G., 1987, A&A, 184, 144
Meylan G., Heggie D. C., 1997, A&AR, 8, 1
Mikkola S., Aarseth S. J., 1993, Celest. Mech. Dyn. Astron., 57, 439
Mikkola S., Aarseth S. J., 1998, New Astron., 3, 309
Olsen K. A. G., Hodge P. W., Mateo M., Olszewski E. W., Schommer R. A., Suntzeff N. B., Walker A. R., 1998, MNRAS, 300, 665
Pagel B. E. J., Tautvaišienė G., 1998, MNRAS, 299, 535
Peng E. W., et al., 2006, ApJ, 639, 838
Plummer H. C., 1911, MNRAS, 71, 460
Portegies Zwart S. F., McMillan S. L. W., 2000, ApJ, 528, L17
Portegies Zwart S. F., McMillan S. L. W., 2002, ApJ, 576, 899
Portegies Zwart S. F., Baumgardt H., Hut P., Makino J., McMillan S. L. W., 2004, Nature, 428, 724
Rochau B., Gouliermis D. A., Brandner W., Dolphin A. E., Henning T., 2007, ApJ, 664, 322
Rosenberg A., Saviane I., Piotto G., Aparicio A., 1999, AJ, 118, 2306
Salaris M., Weiss A., 2002, A&A, 388, 492
Sigurdsson S., Hernquist L., 1993, Nature, 364, 423
Sirianni M., Nota A., De Marchi G., Leitherer C., Clampin M., 2002, ApJ, 579, 275
Spitzer L., 1987, Dynamical Evolution of Globular Clusters. Princeton University Press, Princeton
Trenti M., Heggie D. C., Hut P., 2007, MNRAS, 374, 344
van den Bergh S., Mackey A. D., 2004, MNRAS, 354, 713
van der Marel R. P., Alves D. R., Hardy E., Suntzeff N. B., 2002, AJ, 124, 2639
Verbunt F., Lewin W., 2006, in Lewin W., van der Klis M., eds., Compact stellar X-ray sources. Cambridge University Press, Cambridge, p. 341
Vesperini E., Chernoff D. F., 1994, ApJ, 431, 231
Weidner C., Kroupa P., 2004, MNRAS, 348, 187
Weidner C., Kroupa P., 2006, MNRAS, 365, 1333
Wilkinson M. I., Kleyna J., Evans N. W., Gilmore G. F., 2002, MNRAS, 330, 778
Wilkinson M. I., Hurley J. R., Mackey A. D., Gilmore G. F., Tout C. A., 2003, MNRAS, 343, 1025
Willems B., et al., 2005, ApJ, 625, 324
Zepf S. E., Maccarone T. J., Bergond G., Kundu A., Rhode K. L., Salzer J. J., 2007, ApJ, 669, L69
Zhang W., Woosley S., Heger A., 2007, ApJ, submitted (astro-ph/0701083)
Zhao H., 1996, MNRAS, 278, 488
Zinn R., 1993, in Smith G. H., Brodie J. P., eds., ASP Conf.

Ser. Vol. 48, The Globular Cluster-Galaxy Connection.
Astron. Soc. Pac., San Francisco, p. 38

APPENDIX A: ANALYTIC PROPERTIES OF THE EFF FAMILY OF MODELS

In this Appendix we present analytic expressions for the properties of a number of members of the general family of EFF models. As demonstrated in the present work, with the recent rapid increase in computing power and software sophistication, and hence the size and degree of realism feasible for N-body simulations, it may occur that such models represent more appropriate initial conditions for a given scenario than do the frequently adopted Plummer spheres or King models. With the formulae presented below, it is reasonably straightforward to develop procedures such as that described in Section 2.1 to generate the desired initial conditions.

A1 General properties

The EFF models, after Elson, Fall & Freeman (1987), are a family of models originally defined through empirical fitting to the observed surface brightness profiles of young massive star clusters in the LMC. These objects do not exhibit tidal cut-offs in their outer regions, and are therefore most appropriately described by projected three-parameter models of the form:

$$\mu(r_p) = \mu_0 \left(1 + \frac{r_p^2}{a^2}\right)^{-\frac{\gamma}{2}}, \tag{A1}$$

where r_p is the projected radius, μ_0 is the central surface brightness, a is the scale radius, and γ represents the power-law fall-off of the profile at large radii. These models can easily be deprojected to obtain the three-dimensional density:

$$\rho(r) = \rho_0 \left(1 + \frac{r^2}{a^2}\right)^{-\frac{\gamma+1}{2}} \qquad \text{where} \quad \rho_0 = \frac{\mu_0\, \Gamma\left(\frac{\gamma+1}{2}\right)}{a\sqrt{\pi}\, \Gamma\left(\frac{\gamma}{2}\right)}. \tag{A2}$$

In the above equation, Γ is a standard gamma function. Since μ_0 is the central surface brightness, here ρ_0 is the central luminosity density – to obtain the central mass density it is necessary to multiply by the global mass-to-light ratio Υ. It can be seen that the three-dimensional density has exactly the same functional form as the projected density, but with index $\gamma + 1$. By comparison with the more general spherically symmetric family of (α, β, δ) models described by Zhao (1996)[5], it is straightforward to see that the EFF models represent the subset with $(\alpha, \beta, \delta) = (\frac{1}{2}, \gamma + 1, 0)$ and break radius $r = a$.

Assuming now that ρ_0 is a mass density, substituting Eq. A2 into Eq. 2-22 from Binney & Tremaine (1987) and integrating yields a general expression for the gravitational potential of EFF models:

$$\Phi = -\frac{4}{3}\pi G \rho_0 \left[\frac{3a^2}{\gamma - 1}\left(1 + \frac{r^2}{a^2}\right)^{-\frac{(\gamma-1)}{2}} + r^2\, {}_2F_1\left(\frac{3}{2}, \frac{\gamma+1}{2}; \frac{5}{2}; -\frac{r^2}{a^2}\right)\right], \tag{A3}$$

where ${}_2F_1(a, b; c; z)$ is Gauss's hypergeometric function.

Similarly, the enclosed mass (or luminosity if ρ_0 is a luminosity density) as a function of radius can be derived by integrating Eq. A2:

$$M(r) = 4\pi \int_0^r \rho(r') r'^2 dr' \; = \frac{4}{3}\pi \rho_0 r^3\, {}_2F_1\left(\frac{3}{2}, \frac{\gamma+1}{2}; \frac{5}{2}; -\frac{r^2}{a^2}\right). \tag{A4}$$

In the limit where $r \to \infty$, this expression converges only if $\gamma > 2$. The asymptotic mass is given by $M_\infty = 2\pi\mu_0 \Upsilon a^2/(\gamma - 2)$.

Finally, rearranging and integrating the Jeans equations for a steady-state, spherically symmetric, non-rotating cluster (i.e., Binney & Tremaine (1987) Eq. 4-54) yields a general expression for the radial dependence of the isotropic velocity dispersion:

$$\sigma^2(r) = \frac{1}{\rho(r)} \int_r^\infty \rho(r') \frac{d\Phi(r')}{dr'} dr', \tag{A5}$$

which can, in principle, be evaluated numerically for all γ. However, for integer values of γ, the hypergeometric functions in Eqs. A3 and A4 reduce to elementary functions, resulting in straightforward analytic expressions for $M(r)$ and $\sigma^2(r)$ which may be written into the computer code to generate initial conditions. The best known of the analytic subset is the case when $\gamma = 4$ – the Plummer (1911) sphere. The properties of this model have been investigated extensively by Dejonghe (1987) for mass-follows-light scenarios, while the more general study of Wilkinson et al. (2002) includes the possibility of a dark halo. Below, we consider the less-well studied cases of $\gamma = 3, 5$, and 6.

A2 The $\gamma = 3$ case

The case where $\gamma = 3$ has been studied in passing as special cases of a general ellipsoidal form by de Zeeuw (1985a,b), who labelled the profiles "perfect spheres". This particular case is of interest since it represents the EFF model with analytic expressions for $M(r)$ and $\sigma^2(r)$ which, in projection, is closest in form to the observed profiles of young massive star clusters

[5] Zhao (1996) labelled these (α, β, γ) models; however, we alter his nomenclature here to avoid ambiguity in the definition of γ.

in the LMC and SMC. Elson et al. (1987) found a median value of $\gamma = 2.6$ and a range $2.2 \lesssim \gamma \lesssim 3.2$ for their ten young LMC clusters, while the 18 young LMC and SMC clusters plotted in Fig. 3 in the present paper cover the range $2.05 \leqslant \gamma \leqslant 3.79$ and have a median value $\gamma = 2.67$. We started all the N-body simulations described in the present work with initial conditions generated from the following equations.

When $\gamma = 3$, the Gauss hypergeometric function in Eqs. A3 and A4 reduces to:

$$ {}_2F_1\left(\frac{3}{2}, 2; \frac{5}{2}; -\frac{r^2}{a^2}\right) = -\frac{3a^2}{2r^2}\left(\left[1+\frac{r^2}{a^2}\right]^{-1} - \sqrt{-\frac{a^2}{r^2}}\,\mathrm{arctanh}\left[\sqrt{-\frac{r^2}{a^2}}\right]\right) = \frac{3a^3}{2r^3}\left(\arctan\left[\frac{r}{a}\right] - \frac{r}{a}\left[1+\frac{r^2}{a^2}\right]^{-1}\right) \tag{A6} $$

Substituting into Eq. A4, the enclosed mass $M(r)$ is then given by:

$$ M(r) = 2\pi\rho_0\, a^3\left(\arctan\left[\frac{r}{a}\right] - \frac{r}{a}\left[1+\frac{r^2}{a^2}\right]^{-1}\right), \tag{A7} $$

while carrying out the integration in Eq. A5 provides the isotropic velocity dispersion:

$$ \sigma^2 = -\frac{\pi G\rho_0}{8a^2}(a^2+r^2)^2\left(3\pi^2 - \frac{1}{r(a^2+r^2)^2}\left[4\left(ar + (a^2+r^2)\arctan\left[\frac{r}{a}\right]\right)\left(4a^3 + 3ar^2 + 3r(a^2+r^2)\arctan\left[\frac{r}{a}\right]\right)\right]\right) \tag{A8} $$

A3 Steeper cases: $\gamma = 5$ and $\gamma = 6$

Cluster models with steep density fall-offs do not seem to have been well studied in the literature, if at all. For this reason, the properties of two such models are derived here. These $\gamma = 5$ and $\gamma = 6$ cases *do* correspond to real objects – old globular clusters can have observed brightness profiles which fall off this steeply. For example, Mackey & Gilmore (2003a,b,c) found the LMC globular cluster NGC 1841 to have $\gamma = 4.55 \pm 0.61$, the SMC cluster NGC 339 to have $\gamma = 5.21 \pm 0.99$, and the diffuse cluster 1 in the Fornax dSph to have $\gamma = 7.52 \pm 0.64$. It may well be desirable in future to model the evolution of clusters such as these. In this case, the equations below will allow suitable initial conditions to be simply constructed.

If $\gamma = 5$, the hypergeometric function in Eqs. A3 and A4 reduces to:

$$ \begin{aligned} {}_2F_1\left(\frac{3}{2}, 3; \frac{5}{2}; -\frac{r^2}{a^2}\right) &= \frac{3a^2}{8r^2}\left(\sqrt{-\frac{r^2}{a^2}}(a^2+r^2)^2\right)^{-1}\left(a^2\sqrt{-\frac{r^2}{a^2}}(r^2-a^2) + (a^2+r^2)\,\mathrm{arctanh}\left[\sqrt{-\frac{r^2}{a^2}}\right]\right) \\ &= \frac{3a^3}{8r^3}\left(\frac{ar^3 - a^3r}{(a^2+r^2)^2} + \arctan\left[\frac{r}{a}\right]\right) \end{aligned} \tag{A9} $$

Substituting into Eq. A4, as before, yields the enclosed mass $M(r)$:

$$ M(r) = \frac{1}{2}\pi\rho_0\, a^3\left(\frac{ar^3 - a^3r}{(a^2+r^2)^2} + \arctan\left[\frac{r}{a}\right]\right), \tag{A10} $$

while evaluating Eq. A5 provides the isotropic velocity dispersion as a function of radius:

$$ \begin{aligned} \sigma^2(r) = \frac{\pi G\rho_0}{384a^4r(a^2+r^2)}\Bigg[&5a^8r(64-9\pi^2) + 4a^6r^3(173-45\pi^2) + 30a^4r^5(20-9\pi^2) - 180a^2r^7(\pi^2-1) - 45\pi^2r^9 \\ &+ 12(a^2+r^2)^2\arctan\left[\frac{r}{a}\right]\left(16a^5 + 50a^3r^2 + 30ar^4 + 15r(a^2+r^2)^2\arctan\left[\frac{r}{a}\right]\right)\Bigg]. \end{aligned} \tag{A11} $$

The $\gamma = 6$ case is of particular interest as its properties are comparable in simplicity to those of the widely used Plummer sphere ($\gamma = 4$). With $\gamma = 6$, the hypergeometric function in Eqs. A3 and A4 can be written:

$$ {}_2F_1\left(\frac{3}{2}, \frac{7}{2}; \frac{5}{2}; -\frac{r^2}{a^2}\right) = \frac{a^3}{5}\left[\frac{5a^2+2r^2}{(a^2+r^2)^{\frac{5}{2}}}\right] \tag{A12} $$

which leads to the following straightforward expressions for the enclosed mass and isotropic velocity dispersion:

$$ M(r) = \frac{4}{15}\pi\rho_0\, a^3r^3\left[\frac{5a^2+2r^2}{(a^2+r^2)^{\frac{5}{2}}}\right] \tag{A13} $$

$$ \sigma^2(r) = \frac{1}{75}\pi G\rho_0\, a^3\left[\frac{11a^2+5r^2}{(a^2+r^2)^{\frac{3}{2}}}\right]. \tag{A14} $$

In principle, it is possible to continue deriving similar analytic expressions for increasing integer values of γ; however we note that the expressions become correspondingly more complicated as γ increases.